Evolution and Statistics of Non-sphericity of Galaxy Clusters from Cosmological Simulations

(
)

28　7　　（　）

Abstract

In the standard model of the universe, it is widely accepted that the hierarchical structure has been formed through the gravitational assembly of cold dark matter (CDM). The examination of the CDM paradigm is one of the most important tasks in the era of precision cosmology.

The information on the structure formation history can be extracted from galaxy clusters. In particular, Jing & Suto (2002) (JS02) found a universal probability distribution function (PDF) for the minor-to-major axis ratio of trixaially-modelled simulated halos. This suggests that we can test the CDM paradigm by comparing PDFs of axis ratio between observations and simulations.

Recently, observational analyses of the non-sphericity of galaxy clusters have become feasible. In particular, Kawahara (2010) fitted ellipses to the X-ray surface brightness of galaxy clusters, and showed that their axis ratio is barely consistent with the prediction based on JS02, although the number of analyzed data is small and so the observational uncertainty is large.

In this thesis, by using cosmological hydrodynamical simulations, we show that the prediction based on JS02 is not suitable for precise comparisons with observation data; we calculate PDFs of axis ratio of X-ray surface brightness directly from our simulation data, in the same way as Kawahara (2010), and show that our results are significantly different from the prediction based on JS02. This is mainly because JS02 assumes that the density distribution inside simulated halos is well approximated by concentric ellipsoids with common axis ratio; this assumption affects predictions of *projected* (two-dimensional) axis ratio that is observationally more relevant. Our PDFs are free from the above assumptions, and therefore reliable in comparisons with observation data.

We also preliminarily compare our simulation results with the X-ray observation data analyzed by Kawahara (2010). Our PDF is much closer to the observation data, than the simple prediction based on JS02, while the robustness of both simulation data and observation analyses should be more thoroughly tested with a much larger number of observation and simulation data that is expected to be available in the near future. Especially, we found that the non-sphericity of dark matter halos, as well as gas distribution, significantly depends on baryonic processes adopted in simulations, even up to the virial radius, not only in the central region.

In general, we emphasize that the estimator of the non-sphericity of galaxy clusters both in simulations and observations. This methodology can be straightforwardly applied to a larger number of observation data, including X-ray and gravitational lensing data, and higher-resolution simulations, and the CDM paradigm will be more severely tested in the near future.

Contents

Chapter 1

Introduction

Based on a number of observational evidence, the standard model of the universe, so called the ΛCDM model, lays the foundations of modern cosmology; approximately 70 % of the total energy budget of the universe is attributed to the cosmological constant Λ, a little under 30 % is due to dark matter, and only the remaining a few percent comes from baryons we are familiar with. The hierarchical structure of the universe has been formed through the gravitational assembly of Cold (dissipationless) Dark Matter, which is referred to as the CDM paradigm. The ΛCDM model has been firmly established through a number of observational evidence; in particular, temperature anisotropies in the cosmic microwave background (CMB) radiation, distance measurements of Ia type supernovae, and the abundance of galaxy clusters have independently brought results consistent with the ΛCDM model.

Nevertheless, the ΛCDM model is not always perfect, especially at small scales. In particular, cosmological simulations based on the CDM paradigm produce too much small objects (satellites) in a galactic halo, compared to the amount found in actual observations. In the era of precision cosmology, the CDM paradigm should be more severely tested than ever before, not only at small scales, but also at larger scales where the CDM paradigm has been successful.

One of the most conventional ways to obtain the information on the structure formation history of the universe is observations of galaxy clusters, corresponding to the most massive gravitationally bound halos; since the dynamical time of galaxy clusters reaches to a few Gyr, comparable to the age of the universe, they still hold the information on the structure formation history. For example, the construction of the abundance of galaxy clusters, or the mass function, is one of the principal ways to determine the cosmological parameters (Allen et al., 2011, for a recent review).

Cosmological applications of galaxy clusters have been mainly performed under the assumption of spherical symmetry for simplicity. A number of observations and cosmological simulations, however, has exhibited clear signatures of the non-sphericity of dark matter halos. In addition, from a theoretical point of view, the Gaussian random field, a conventional description of the primordial density fluctuations, predicts a definite statistical signature of the non-sphericity already imprinted in the early universe (Doroshkevich, 1970; Bardeen et al., 1986). Hence the non-spherical observational analyses of galaxy clusters are essentially required to promote their cosmological applications, and have recently

become feasible thanks to the development of observational techniques.

The improved quality of observational data demands accurate theoretical predictions of the non-sphericity of cluster-scale halos. However, purely theoretical description of the non-spherical structure and evolution of dark matter halos is very difficult due to the non-linear evolution and complicated interactions among dark matter within the highly inhomogeneous density distribution. Therefore cosmological simulations play key roles in investigating the non-sphericity.

Among the recent simulation studies on the non-sphericity, Jing & Suto (2002) (hereafter JS02) modelled their simulated halos by triaxial ellipsoids, and found that their minor-to-major axis ratio follows a universal probability distribution function (PDF). The universality of the non-sphericity suggests that a comparison of PDFs of axis ratio between simulations and observations can be a test for the CDM paradigm.

Actually, observational estimates of PDFs of axis ratio have been already performed, although the number of available observation data is limited for now. The weak lensing study by Oguri et al. (2010) has shown that their 18 clusters have PDF of axis ratio barely consistent with that proposed by JS02 while the observational uncertainty is large. The 70 X-ray clusters analyzed by Kawahara (2010) also produced a consistent result with JS02, although the observational uncertainty is large, too. In the near future, especially Subaru Hyper Suprime-Cam (HSC)[1] will provide us with a number of highly resolved lensing halos which are suitable for non-spherical analyses. In addition, since the surface brightness is one of the primary observables in X-ray observations of galaxy clusters, a number of available X-ray data may be already existing. Also, future projects like eROSITA[2] will provide us with plenty of X-ray data.

For more precise comparisons between observations and simulations, however, we suspect that the PDF of JS02 is inadequate; the PDF is constructed in the *three-dimensional* space, so it must be arranged for comparisons with *two-dimensional* observation data. For example, Oguri et al. (2003) integrated the PDF of JS02 along randomly oriented lines-of-sight, and the resulting PDF of *projected* axis ratio is compared with the weak lensing data by Oguri et al. (2010). In order to precisely compare observations and simulations, it is the best way to calculate the non-sphericity *of the observable quantity in each observation* directly from simulations.

Based on the above background, the main goals of this paper is to make more reliable predictions on PDFs of axis ratio of galaxy clusters by using cosmological simulations, and to establish the methodology to test the CDM paradigm by comparing PDFs between simulations and observations. We predict PDFs of projected axis ratio of dark matter density distribution and the X-ray surface brightness, directly from cosmological simulations. We then clarify the difference between our results and the prediction of JS02. Our resulting PDFs of projected axis ratio are compared with the observation data by Oguri et al. (2010) (weak lensing) and Kawahara (2010) (X-ray). Especially, we calculate the axis ratio of X-ray surface brightness in the same way as Kawahara (2010), and therefore we can make a conclusion on the consistency between the observation data and the simulations, i.e., the validity of the CDM paradigm, for the currently available data.

The construction of PDFs of axis ratio itself can be achievable just by processing the

---

[1]www.naoj.org/Projects/HSC/

[2]http://www.mpe.mpg.de/eROSITA

simulation data. It is important, however, to physically understand the simulation results as possible. Especially, we attempt to clarify how and to what extent the simulation results differ from purely theoretical predictions, including the spherical collapse model and the ellipsoidal collapse model.

While the spherical collapse model and ellipsoidal collapse model are widely used in *statistically* describing the evolution of halos, the *individual* comparison with the simulation results has never been performed in the previous literature. Since these theoretical models adopt a variety of strong assumptions, the validity of their predictions should be examined.

In this thesis, before constructing PDFs of axis ratio of halos, we compare the evolution of individual simulated halos with the conventional spherical collapse model and ellipsoidal collapse model, *on the object-wise basis*. The results of the comparisons turn out to be helpful to interpret statistical features on the non-sphericity of halos.

The rest of this thesis as follows:

- Chapter 2 reviews the theoretical models to describe the evolution and virialized state of dark matter halos under the spherical symmetry assumption.

- In Chapter 3, we summarize the previous studies on the non-sphericity of halos. First, we describe the theoretical models on the non-sphericity; the Gaussian random initial conditions and the ellipsoidal collapse model. Next we present the simulation study by JS02 who found the universality in the non-sphericity of simulated halos. Then we summarize the study by Rossi et al. (2011) that pointed out the discrepancy between the PDF of JS02 and the theoretical prediction from the Gaussian random initial conditions. In addition, we review the previous observational studies on the non-sphericity of galaxy clusters by Oguri et al. (2010) and Kawahara (2010).

- Chapter 4 compares the prediction of the spherical collapse model with the evolution of individual halos extracted from the N-body simulation. We confirm that the velocity dispersion that is neglected in the spherical collapse model, plays important roles in the evolution of the simulated halos. This chapter is based on Suto et al. (2016)

- In Chapter 5, we compare the prediction of the ellipsoidal collapse model with the evolution of individual simulated halos. Especially we emphasize that the density distribution of the simulated halos is not necessarily self-similar. We then construct PDFs of projected axis ratio directly from the simulation data, and show that the self-similarity assumption adopted in JS02 is indeed invalid. Furthermore, we compare our simulation results with the weak-lensing data by Oguri et al. (2010).

- In Chapter 6, we measure the axis ratio of X-ray surface brightness from the galaxy clusters extracted from the cosmological hydrodynamical simulations, in the same way as Kawahara (2010) for the actual clusters. We statistically test the consistency between our results and the observation data by Kawahara (2010).

- Chapter 7 presents the summary and conclusion of this thesis.

Chapter 2

Evolution and Structure of Dark Matter Halos under Spherical Symmetry

In order to better understand the non-sphericity of dark matter halos, we first have to know how their evolution and structure are theoretically described *under the spherical symmetry*. For example, the ellipsoidal collapse model (Section 3.2) is extension of the spherical collapse model (Section 2.2). In this Chapter, we review the theoretical models that have been conventionally used to describe spherical pictures of dark matter halos. Most parts of this chapter will be referred to in Chapter 4, where we compare the top-hat spherical collapse model with the simulation results.

2.1 Dynamics of Collisionless Particles

We begin with the general description of the evolution of collisionless particles, i.e., the collisionless Boltzmann equation:

$$\frac{df}{dt} = \frac{\partial f}{\partial t} + \sum_i v_i \frac{\partial f}{\partial x_i} - \sum_i \frac{\partial \phi}{\partial x_i} \frac{\partial f}{\partial v_i} = 0, \tag{2.1}$$

where $f = f(\boldsymbol{x}, \boldsymbol{v}, t)$ is the phase space density of the particles, and $\phi = \phi(\boldsymbol{x}, t)$ is the gravitational potential at the position $\boldsymbol{x}$. For simplicity, we here assume that all the particles have the same mass m; otherwise, the momentum $\boldsymbol{p}$ should be used instead of the velocity $\boldsymbol{v}$.

Integrating Equation (2.1) over the velocity space yields the continuity equation:

$$\frac{\partial \rho}{\partial t} + \sum_i \frac{\partial}{\partial x_i} \left(\rho \bar{v}_i \right) = 0, \tag{2.2}$$

where

$$\rho(\boldsymbol{x}, t) = m \int d^3 v \ f(\boldsymbol{x}, \boldsymbol{v}, t) \tag{2.3}$$

is the density, and

$$\bar{v}_i(\boldsymbol{x}, t) = \int d^3v \ v_i f(\boldsymbol{x}, \boldsymbol{v}, t) \bigg/ \int d^3v f(\boldsymbol{x}, \boldsymbol{v}, t) \tag{2.4}$$

is the mean velocity at position $\boldsymbol{x}$.

Similarly, by multiplying Equation (2.1) by $\bar{v}_j$ and integrating over the velocity space, one obtains the following:

$$\frac{\partial \rho \bar{v}_j}{\partial t} + \sum_i \frac{\partial}{\partial x_i} \left(\rho \overline{v_i v_j} \right) + \rho \frac{\partial \phi}{\partial x_j} = 0, \tag{2.5}$$

where

$$\overline{v_i v_j}(\boldsymbol{x}, t) = \int d^3v \ v_i v_j f(\boldsymbol{x}, \boldsymbol{v}, t) \bigg/ \int d^3v f(\boldsymbol{x}, \boldsymbol{v}, t). \tag{2.6}$$

The above equation can be rewritten as

$$\frac{\partial \bar{v}_j}{\partial t} + \sum_i \bar{v}_i \frac{\partial \bar{v}_j}{\partial x_i} = -\frac{1}{\rho} \sum_i \frac{\partial}{\partial x_i} \left(\rho \sigma_{ij}^2 \right) - \frac{\partial \phi}{\partial x_j}, \tag{2.7}$$

where

$$\sigma_{ij}^2 = \overline{v_i v_j} - \bar{v}_i \bar{v}_j, \tag{2.8}$$

is the velocity dispersion. Equation (2.7) gives the equation of motion for collisionless particles, and called the Jeans equation.

In the spherical coordinates (r, θ, φ), the Jeans equation for the r-direction is written as

$$\frac{\partial v_r}{\partial t} + \left[v_r \frac{\partial}{\partial r} + \frac{v_\theta}{r} \frac{\partial}{\partial \theta} + \frac{v_\varphi}{r \sin \theta} \frac{\partial}{\partial \varphi} \right] v_r = -\frac{1}{\rho} \left[\frac{\partial (\rho \sigma_{rr}^2)}{\partial r} + \frac{1}{r} \frac{\partial (\rho \sigma_{r\theta}^2)}{\partial \theta} + \frac{1}{r \sin \theta} \frac{\partial (\rho \sigma_{r\varphi}^2)}{\partial \varphi} \right]$$

$$- \frac{2\sigma_{rr}^2 - \sigma_{\theta\theta}^2 - \sigma_{\varphi\varphi}^2 - \bar{v}_\theta^2 - \bar{v}_\varphi^2 + \sigma_{r\theta}^2 \cot \theta}{r} - \frac{\partial \phi}{\partial r}. \tag{2.9}$$

In addition, under the spherical symmetry, the above equation reduces to

$$\frac{\partial v_r}{\partial t} + v_r \frac{\partial v_r}{\partial r} = -\frac{1}{\rho} \frac{\partial (\rho \sigma_{rr}^2)}{\partial r} - \frac{2\beta \sigma_{rr}^2}{r} - \frac{\partial \phi}{\partial r}, \tag{2.10}$$

where

$$\beta = 1 - \frac{\sigma_{\theta\theta}^2 + \sigma_{\varphi\varphi}^2}{2\sigma_{rr}^2} \tag{2.11}$$

is called the velocity anisotropy parameter. If the velocity dispersion is exactly isotropic, $\beta = 0$, and if the radial (tangential) component is dominant, $\beta = 1$ ($\beta \to -\infty$). The Jeans equation (2.10) is one of the most conventional forms to describe the motion of dark matter particles inside a halo.

We next derive the energy equation for the collisionless system, and then discuss the equilibrium state. Multiplying Equation (2.5) by mx_k and integrating over $\boldsymbol{x}$ yields

$$\int d^3x \; x_k \frac{\partial(\rho\bar{v}_j)}{\partial t} = -\sum_i \int d^3x \; x_k \frac{\partial(\rho\overline{v_i v_j})}{\partial x_i} - \int d^3x \; \rho x_k \frac{\partial\phi}{\partial x_j}. \tag{2.12}$$

The first term in the right-hand side is written as

$$-\sum_i \int d^3x \; x_k \frac{\partial(\rho\overline{v_i v_j})}{\partial x_i} = \int d^3x \; \rho\overline{v_j v_k} - \sum_i \int d\sigma_i \; x_k \rho\overline{v_i v_j}, \tag{2.13}$$

where $d\sigma_i$ represents the surface element oriented toward the direction of x_i. We rewrite the right-hand side of the above equation in terms of the kinetic energy tensor K_{jk}:

$$K_{jk} = \frac{1}{2}\int d^3x \rho\overline{v_j v_k}, \tag{2.14}$$

and the surface pressure term Σ_{jk}:

$$\Sigma_{jk} = -\sum_i \int d\sigma_i \; x_j \rho\overline{v_i v_j}. \tag{2.15}$$

The second term in the right-hand side of Equation (2.12) is just the definition of the Chandrasekhar potential tensor W_{jk}:

$$W_{jk} = -\int d^3x \; \rho x_k \frac{\partial\phi}{\partial x_j}. \tag{2.16}$$

For the gravitational system, ϕ is given by

$$\phi(\boldsymbol{x}) = -G\int d^3x' \; \frac{\rho(\boldsymbol{x}')}{|\boldsymbol{x}' - \boldsymbol{x}|} \tag{2.17}$$

and therefore W_{jk} becomes

$$W_{jk} = G\int d^3x \int d^3x' \; \rho(\boldsymbol{x})\rho(\boldsymbol{x}')\frac{x_j(x'_k - x_k)}{|\boldsymbol{x}' - \boldsymbol{x}|^3}. \tag{2.18}$$

In the above equation, one can interchange $\boldsymbol{x}$ and $\boldsymbol{x}'$ since they are dummy variables of integration:

$$W_{jk} = G\int d^3x' \int d^3x \; \rho(\boldsymbol{x}')\rho(\boldsymbol{x})\frac{x'_j(x_k - x'_k)}{|\boldsymbol{x} - \boldsymbol{x}'|^3}. \tag{2.19}$$

Combining Equations (2.18) and (2.19), one obtains

$$W_{jk} = -\frac{G}{2}\int d^3x \int d^3x' \; \rho(\boldsymbol{x})\rho(\boldsymbol{x}')\frac{(x'_j - x_j)(x'_k - x_k)}{|\boldsymbol{x}' - \boldsymbol{x}|^3}, \tag{2.20}$$

which explicitly indicates that W_{jk} is symmetric about the subscripts j and k. Taking the trace of above equation yields

$$\sum_k W_{kk} = -\frac{G}{2} \int d^3x \ \rho(\boldsymbol{x}) \int d^3x' \ \frac{\rho(\boldsymbol{x}')}{|\boldsymbol{x} - \boldsymbol{x}'|}$$
$$= \frac{1}{2} \int d^3x \ \rho(\boldsymbol{x})\phi(\boldsymbol{x}). \tag{2.21}$$

Hence the trace of W_{jk} reproduces the ordinary definition of the total gravitational potential energy.

Because the right-hand side of Equation (2.12) is now $2K_{jk} + W_{jk} + \Sigma_{jk}$, and because K_{jk}, W_{jk} and Σ_{jk} are symmetric about j and k, the left-hand side is also symmetric about j and k. Therefore we can rewrite Equation (2.12) as

$$\frac{1}{2}\frac{d}{dt} \int d^3x \ \rho \left(x_k \bar{v}_j + x_j \bar{v}_k \right) = 2K_{jk} + W_{jk} + \Sigma_{jk}. \tag{2.22}$$

Furthermore, for the inertial moment tensor I_{jk}:

$$I_{jk} = \int d^3x \ \rho x_j x_k, \tag{2.23}$$

its time-derivative satisfies

$$\frac{dI_{jk}}{dt} = \int d^3x \ \frac{\partial \rho}{\partial t} x_j x_k = -\int d^3x \ \frac{\partial(\rho \bar{v}_i)}{\partial x_i} x_j x_k$$
$$= \int d^3x \ \left(x_k \bar{v}_j + x_j \bar{v}_k \right). \tag{2.24}$$

Therefore Equation (2.12) finally becomes

$$\frac{1}{2}\frac{d^2 I_{jk}}{dt^2} = 2K_{jk} + W_{jk} + \Sigma_{jk}. \tag{2.25}$$

This is called the tensor virial theorem. By taking the trace of both sides of the above equation, one obtains the scalar virial theorem:

$$\frac{1}{2}\frac{d^2 I}{dt^2} = 2K + W + \Sigma, \tag{2.26}$$

where

$$I = \int d^3x \ \rho|\boldsymbol{x}|^2, \qquad K = \frac{1}{2} \int d^3x \ \rho\overline{v^2},$$
$$W = -\int d^3x \ \rho\boldsymbol{x} \cdot \nabla\phi, \qquad \Sigma = -\int d\boldsymbol{\sigma} \cdot \boldsymbol{x}\rho\overline{v^2}. \tag{2.27}$$

For a static system, $d^2 I/dt^2 = 0$, and so

$$2K + W + \Sigma = 0. \tag{2.28}$$

In particular, when the surface pressure term Σ is negligible, Equation (2.28) indicates that the total energy E satisfies $E = K + W = -K$. The virial theorem is widely used in theoretical models, including the spherical collapse model and ellipsoidal model (described in the later sections), to describe the dynamical equilibrium state of dark matter halos.

2.2 Top-Hat Spherical Collapse Model

Structures in the universe are formed through gravitational assemblies of dark matter, starting from primordial density fluctuations. Except for early times of the universe, the evolution of the density fluctuation is non-linear. The top-hat spherical collapse model (Gunn & Gott, 1972; Gunn, 1977; Peebles, 1980) provides the most simple description of the non-linear evolution of density fluctuations. In this section, we summarize the basic equations and assumptions adopted in the top-hat spherical collapse model in the Einstein de Sitter (EdS) universe (Subsection 2.2.1) and the flat universe with the cosmological constant Λ (Subsection 2.2.2).

2.2.1 Einstein de Sitter universe

We consider an *isolated homogeneous* spherical region in the Einstein de Sitter (EdS) universe ($\Omega_m = 1$). Assuming that the sphere has radius r_i at the initial time t_i, the initial density ρ_i can be written as

$$\rho_i(r) = \begin{cases} \bar{\rho}_i(1 + \delta_i) & ; \quad r < r_i \\ \\ 0 & ; \quad r > r_i, \end{cases} \tag{2.29}$$

where $\bar{\rho}_i = (6\pi G t_i^2)^{-1}$ is the cosmic mean density, and δ_i (independent of r) is the initial density contrast. Throughout this thesis, we refer to this form of density profile as a "top-hat" density profile.

The time evolution of the radius $r(t)$ of the sphere follows

$$\frac{d^2 r}{dt^2} = -\frac{GM}{r^2} = -\frac{4\pi G}{3}\bar{\rho}(t)(1 + \delta(t))r, \tag{2.30}$$

where $M = 4\pi\bar{\rho}(t)(1+\delta(t))r^3/3$ is the total mass of the sphere. Throughout the evolution, the density contrast $\delta(t)$ inside the sphere is determined so that M remains constant. We emphasize that, in general, the motion of collisionless dark matter particles obeys the Jeans equation that takes into account the velocity dispersion of particles. The above equation of motion neglects the velocity dispersion.

Integration of the equation of motion (2.30) yields the following energy equation:

$$\frac{1}{2}\left(\frac{dr}{dt}\right)^2 - \frac{GM}{r} = E, \tag{2.31}$$

where E is the total energy. If $E < 0$, Equation (2.30) has a bound-state solution. The solution is parametrically written as

$$t = \frac{t_{\text{ta}}}{\pi}(\theta - \sin\theta) \quad , \quad r = \frac{r_{\text{ta}}}{2}(1 - \cos\theta). \tag{2.32}$$

Accordingly, the overdensity $\Delta = \rho/\bar{\rho}$ ($= 1 + \delta$) inside the sphere is also parametrically described as follows:

$$\Delta = \frac{9}{2}\frac{(\theta - \sin\theta)^2}{(1 - \cos\theta)^3}. \tag{2.33}$$

The above solution states that r reaches a maximum, or "turns-around" at $\theta = \pi$. We have normalized t and r by the values at $\theta = \pi$, i.e., t_{ta} and r_{ta}, and they satisfy

$$\frac{r_{ta}^3}{t_{ta}^2}\frac{\pi^2}{8} = GM. \tag{2.34}$$

We note that the equation of motion (2.30) is independent of the scale of r. Consequently, $r(t)/r_{ta}$ and $\Delta(t)$ do not depend on M and are determined solely by δ_i. Therefore the initially homogeneous sphere remains homogeneous throughout the evolution. In particular, at the turn-around time t_{ta}, the overdensity $\Delta_{ta} \equiv \Delta(t_{ta})$ satisfy

$$\Delta_{ta} = \frac{9\pi^2}{16} \approx 5.55 \tag{2.35}$$

inside the sphere.

According to the solution (2.32), r contracts to zero at the "collapse time" $t_{col} = 2t_{ta}$. Then $\Delta(t_{col})$ diverges to infinity, which is, of course, unrealistic. Hence the another assumption is needed to describe the state of the sphere after $t = t_{col}$. In fact, it is conventional to assume that the system instantaneously reaches to the virial equilibrium at $t = t_{col}$, described as follows.

At $t = t_{ta}$, the kinetic energy $K_{ta} = 0$ since all the matter inside the sphere stop expansion. In contrast, at $t = t_{col}$, the kinetic energy K_{vir} inside the sphere is assumed to be half the absolute value of the potential energy W_{vir}. Since the density in the sphere is homogeneous at all times, the potential energy W within the sphere is given by

$$W = -\frac{3}{5}\frac{GM^2}{r}. \tag{2.36}$$

Hence, by equating the total energies at $t = t_{ta}$ and t_{col}; $K_{ta} + W_{ta} = K_{vir} + W_{vir}$, one obtains

$$r_{vir} = \frac{1}{2}r_{ta}. \tag{2.37}$$

Note that the factor $3/5$ in W comes from the homogeneous density profile. It is essential that the retained homogeneity yields the *same* factor of $3/5$ both at t_{ta} and t_{col}. We will revisit this point in Chapter 4.

According to the above simplified treatment, the radius r of the sphere *instantaneously* takes the finite value r_{vir} at $t = t_{col}$, rather than vanishing. As a result, the overdensity $\Delta_{vir} \equiv \Delta(t_{col})$ does not diverge, but becomes finite:

$$\Delta_{vir} = 18\pi^2 \approx 177.7. \tag{2.38}$$

This value of Δ_{vir} is independent of M and δ_i; any collapsed object has the same value of Δ_{vir} at $t = t_{col}$. This is part of a reason why Δ_{vir} is widely used as the threshold of halo identification in numerical simulations.

It is conventional to relate the above non-linear evolution of the sphere with that in the linear regime. At early time t where the density contrast δ is much less than unity, r, t and δ can be approximated up to the leading order of θ:

$$t \approx \frac{t_{ta}}{6\pi}\theta^3 \quad , \quad r \approx \frac{r_{ta}}{4}\theta^2 \quad , \quad \delta \approx \frac{3}{20}\theta^2. \tag{2.39}$$

Hence δ grows as $t^{2/3}$ in the linear regime, which corresponds to the linear growth rate $D(t)$ in the EdS universe is proportional to the scale factor $a \propto t^{2/3}$.

In particular, at the turn-around time t_{ta},

$$\delta_{\text{ta,lin}} = \frac{3}{20}(6\pi)^{2/3} \approx 1.05 \tag{2.40}$$

and at the collapse time t_{col},

$$\delta_{\text{vir,lin}} = \frac{3}{20}(12\pi)^{2/3} \approx 1.69. \tag{2.41}$$

The latter value corresponds to the *linearly-extrapolated* density contrast of collapsed (viliarized) objects, and widely used in theoretical studies including the Press-Schechter theory (Press & Schechter, 1974).

All the results in this subsection are strictly correct only in the EdS universe. We describe the top-hat spherical collapse model in the spatially flat universe with the non-zero cosmological constant Λ in the next subsection.

2.2.2   Flat universe with $\Omega_\Lambda > 0$

We consider the evolution of an isolated homogeneous sphere in the flat universe with $\Omega_\Lambda > 0$ (Lacey & Cole, 1993; Eke et al., 1996; Nakamura & Suto, 1997). For simplicity, we assume that the sphere collapses exactly at the present time; $a(t_{\text{col}}) = 1$. In this section, we denote Ω_m simply by Ω, and so $\Omega_\Lambda = 1 - \Omega$. The time-dependence of the scale factor can be parametrically written as

$$
\begin{aligned}
H_v t &= \frac{1}{3}(1 - \Omega_v)^{-1/2}\cosh^{-1}(1 + 2\chi), \\
a &= \left(\frac{\Omega_v}{1 - \Omega_v}\right)^{1/3}\chi^{1/3},
\end{aligned}
\tag{2.42}
$$

where the subscript v denotes the values at the collapse (or virlial) time $t_c ol$. Since $a_v = 1$,

$$\Omega_v = \frac{1}{1 + \chi_v} \quad ; \quad 1 - \Omega_v = \frac{\chi_v}{1 + \chi_v}. \tag{2.43}$$

It can also be easily shown that

$$Ht = \frac{1}{3}\left(\frac{1 + \chi}{\chi}\right)^{1/2}\cosh^{-1}(1 + 2\chi). \tag{2.44}$$

A sphere of mass M and radius $r(t)$ obeys the following equation of motion:

$$\frac{d^2 r}{dt^2} = -\frac{GM}{r^2} + \frac{\Lambda}{3}r. \tag{2.45}$$

Integrating Equation (2.45) gives the energy equation:

$$\frac{1}{2}\left(\frac{dr}{dt}\right)^2 - \frac{GM}{r} - \frac{\Lambda}{6}r^2 = E, \tag{2.46}$$

where the energy E is defined at the turn-around time t_{ta}:

$$E = -\frac{GM}{r_{\text{ta}}} - \frac{\Lambda}{6} r_{\text{ta}}^2.$$
(2.47)

Integrating the energy equation, one obtains

$$Ht = \zeta^{1/2} \left(\frac{1+\chi}{\chi}\right) \int_0^y dx \; \left[\frac{1}{x} - (1+\zeta) + \zeta x^2\right]^{-1/2},$$
(2.48)

where

$$y = \frac{r}{r_{\text{ta}}} \quad , \quad \zeta = \frac{r_{\text{ta}}^3 \Lambda}{6GM}.$$
(2.49)

Note that ζ is time-independent. In order for the sphere to turn around (i.e., the integrand of Equation (2.48) does not diverge in the range $0 < x < 1$), ζ must satisfy $0 < \zeta < 1/2$. Using *zeta* and y, the overdensity Δ $(= 1 + \delta)$ is written as

$$\Delta = \frac{3M}{4\pi\bar{\rho}r^3} = \frac{\chi}{y^3\zeta}.$$
(2.50)

The collapse time is given by

$$H_v t_v = 2\zeta^{1/2} \left(\frac{1+\chi_v}{\chi_v}\right) \int_0^1 dx \; \left[\frac{1}{x} - (1+\zeta) + \zeta x^2\right]^{-1/2}.$$
(2.51)

Now we replace the variable x by

$$x = \frac{(2 - \zeta - \eta)t^2}{2[1 + 2\zeta - (3\zeta + \eta - 1)t^2]},$$
(2.52)

where

$$\eta = \sqrt{4\zeta + \zeta^2}.$$
(2.53)

Then $H_v t_v$ can be expressed as

$$H_v t_v = \frac{4(\zeta + \eta)}{\sqrt{(\eta + 3\zeta)(\eta - \zeta)}} \left[\Pi(\nu, k) - K(k)\right],$$
(2.54)

where $K(k)$ and $\Pi(\nu, k)$ are the elliptic integrals of the first and third kinds characterized by

$$k^2 = \frac{4\eta\zeta}{(\eta + 3\zeta)(\eta - \zeta)} \quad , \quad \nu = \frac{2\zeta}{\eta + 3\zeta}.$$
(2.55)

Using Equation (2.44), one obtains

$$\chi_v = \frac{1}{2} \left[\cosh\left(\frac{12(\zeta + \eta)}{\sqrt{(\eta + 3\zeta)(\eta - \zeta)}} \left[\Pi(\nu, k) - K(k)\right]\right) - 1\right].$$
(2.56)

From the virial theorem,

$$\langle U_m \rangle_{\text{ta}} + \langle U_\Lambda \rangle_{\text{ta}} = \frac{1}{2}\langle U_m \rangle_{\text{vir}} + 2\langle U_\Lambda \rangle_{\text{vir}},$$
(2.57)

where

$$\langle U_m \rangle = -\frac{3}{5}\frac{GM}{r} \qquad , \qquad \langle U_\Lambda \rangle = -\frac{1}{10}\Lambda M r^2 \tag{2.58}$$

are the gravitational potential energy due to the total mass M, and the potential energy due to the cosmological constant Λ, respectively. By using ζ and y_v, Equation (2.57) is written as

$$4\zeta y_v^3 - 2(1+\zeta)y_v + 1 = 0. \tag{2.59}$$

Equation (2.59) has a solution in the range $0 < y_v < 1$:

$$y_v = \left(\frac{2+2\zeta}{3\zeta}\right)^{1/2} \cos\left[\frac{2}{3}\pi - \frac{1}{3}\cos^{-1}\left\{-\frac{1}{\zeta}\left(\frac{3\zeta}{2+2\zeta}\right)^{3/2}\right\}\right]. \tag{2.60}$$

Combining all the above results, the virial overdensity $\Delta_{\rm vir}$ is given by

$$\Delta_{\rm vir} = \frac{\chi_v}{y_v^3 \zeta}, \tag{2.61}$$

where χ_v and y_v are given by Equations (2.56) and (2.60), respectively. This is considered to be the density contrast at the collapse time in the non-linear theory.

Next we calculate the linearly-extrapolated density contrast $\delta_{\rm vir,lin}$. In the early stages ($y \ll 1$), Equations (2.44) and (2.48) give

$$Ht \simeq \frac{2}{3}(1+\chi)^{1/2} \tag{2.62}$$

and

$$Ht \simeq \frac{2}{3}\zeta^{1/2}\left(\frac{1+\chi}{\chi}\right)^{1/2} y^{3/2}\left[1 + \frac{3}{10}(1+\zeta)y\right]. \tag{2.63}$$

Equating Equations (2.62) and (2.63) gives y iteratively:

$$y \simeq \left(\frac{\chi}{\zeta}\right)^{1/3}\left[1 - \frac{1}{5}(1+\zeta)\left(\frac{\chi}{\zeta}\right)^{1/3}\right]. \tag{2.64}$$

Combining all the above results, the initial density contrast δ_i is given by

$$\delta_i \simeq \frac{3}{5}(1+\zeta)\left(\frac{\chi}{\zeta}\right)^{1/3} = \frac{3}{5}a(1+\zeta)\left(\frac{\chi_v}{\zeta}\right)^{1/3}, \tag{2.65}$$

showing that $\delta_i \propto a$ as predicted by the linear theory. Since the linear growth rate D_+ in an open universe is given by

$$D_+ = a\,_2F_1\left(1, \frac{1}{3}, \frac{11}{6}; -\chi\right), \tag{2.66}$$

the density contrast $\delta_{\rm vir,lin}$ at the collapse time is given by

$$\delta_{\rm vir,lin} = \frac{3}{5}\,_2F_1\left(1, \frac{1}{3}, \frac{11}{6}; -\chi_v\right)(1+\zeta)\left(\frac{\chi_v}{\zeta}\right)^{1/3}. \tag{2.67}$$
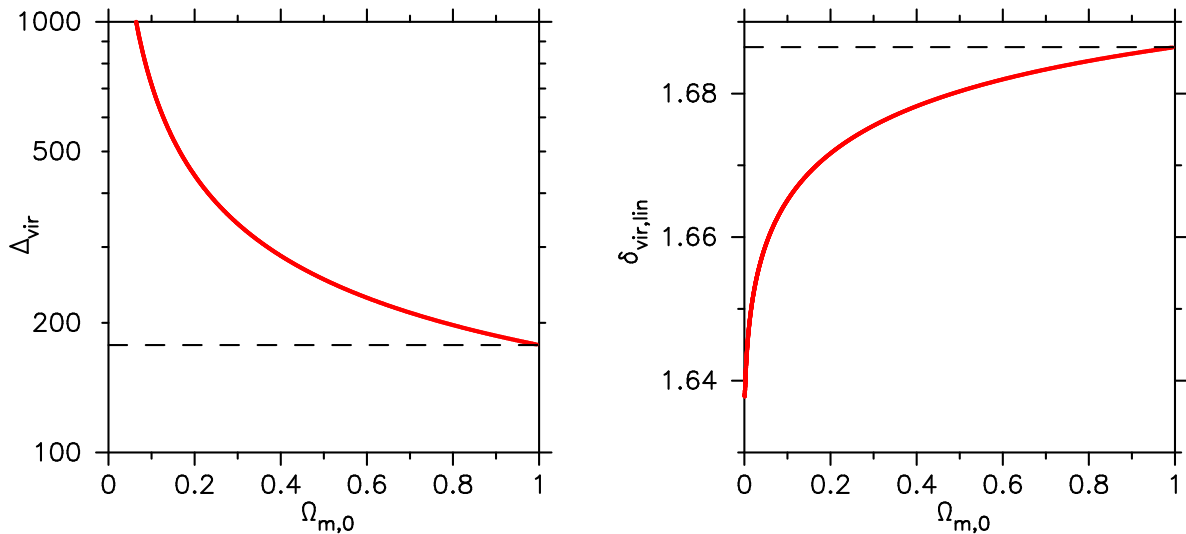
Figure 2.1: Virial overdensity $\Delta_{\rm vir}$ (left) and its linearly-extrapolated value $\delta_{\rm vir,lin}$ (right), as a function of $\Omega_{m,0}$. In each panel, the dashed line indicates the value for the EdS universe ($\Omega_{m,0} = 0$).

Figure 2.1 shows the dependence of $\Delta_{\rm vir}$ (left) and $\delta_{\rm vir,lin}$ (right) on $\Omega_{m,0}$. While $\Delta_{\rm vir}$ strongly depends on $\Omega_{m,0}$, $\delta_{\rm vir,lin}$ only slightly depends on $\Omega_{m,0}$. Hence the value $\delta_{\rm vir,lin} \approx 1.68$ is widely used as the linearly-extrapolated density contrast of virialized objects, for any $\Omega_{m,0}$.

In Chapters 4 and 5, we use the cosmological N-body simulations with $\Omega_{m,0} = 0.279$. For this value of $\Omega_{m,0}$, $\Delta_{\rm vir} \approx 355.4$ and $\delta_{\rm vir,lin} \approx 1.675$. We use the value $\Delta_{\rm vir} \approx 355.4$ to identify halos from the simulation data at $z = 0$.

2.3 Self-Similar Spherical Collapse — Bertschinger Model

One of the strong assumptions adopted in the top-hat spherical collapse model (TSC) is the homogeneous density in the sphere. Fillmore & Goldreich (1984) and Bertschinger (1985) considered mass shells with inhomogeneous density profile, and developed a self-similar collapse model. Due to crossings of mass shells in the inhomogeneous density field, the self-similar model naturally yields a picture of velocity dispersion of dark matter that is neglected in TSC. Strictly speaking, the self-similar model holds only in the EdS universe, but its qualitative picture gives us an important insight into the dynamics of dark matter. We summarize the key points of the self-similar model in this section.

2.3.1 Cold accretion onto a black hole

Before describing the self-similar model including the shell crossing, we consider mass shells accreting onto a black hole, as done by Bertschinger (1985); since a mass shell does

not turn back after it falls onto the black hole, the shell crossing never happens. There is a self-similar solution also in this case, and the resulting solution will be helpful in the next subsection.

At the initial time t_i, the density profile is set as follows:

$$\rho = \rho_i \times \begin{cases} 1 + \delta_{a,i} & ; \quad r < r_{a,i} \\ \\ 1 & ; \quad r > r_{a,i}, \end{cases} \tag{2.68}$$

where $\rho_i = (6\pi G t_i^2)^{-1}$, and $r_{a,i}$ is the initial radius of the overdense region, corresponding, in this case, to the black hole radius.

For the mass shell with the initial radius $r_i(> r_{a,i})$, the equation of motion is given by

$$\frac{d^2 r}{dt^2} = -\frac{Gm}{r^2}, \tag{2.69}$$

where

$$m = \frac{4\pi}{3} \rho_i r_i^3 \left(1 + \delta_{a,i} \frac{r_{a,i}^3}{r_i^3} \right) \equiv \frac{4\pi}{3} \rho_i r_i^3 (1 + \delta_i). \tag{2.70}$$

We have denoted the initial overdensity for the mass shell under consideration by $\delta_i = \delta_{a,i}(r_{a,i}/r_i)^3$. By normalizing the radius and time by their initial values, namely, by using $\tau = t/t_i$, $y = r/r_i$, the equation of motion is written as

$$\frac{d^2 y}{d\tau^2} = -\frac{2}{9}(1 + \delta_i)\frac{1}{y^2}. \tag{2.71}$$

Also, the initial conditions now become $y = 1$ and $dy/d\tau = 2/3$ (i.e., the Hubble speed) at $\tau = 1$. The above equation of motion can be solved in the same way as in the case of TSC, and for $\delta_i \ll 1$, τ and y are given by

$$\tau = \frac{3}{4}(\theta - \sin\theta) \left(\frac{5}{3}\delta_i \right)^{-3/2} \tag{2.72}$$

and

$$y = \frac{1}{2}(1 - \cos\theta) \left(\frac{5}{3}\delta_i \right)^{-1}. \tag{2.73}$$

Then the turn-around radius r_{ta} of the mass shell satisfies

$$r_{\text{ta}}(t) = \left(\frac{3\pi}{4} \right)^{-8/9} \left(\frac{5}{3}\delta_{a,i} \right)^{1/3} r_{a,i}\tau^{8/9}. \tag{2.74}$$

In other words, $r_{\text{ta}}(t)$ can be interpreted as *the turn-around radius of the mass shell that turns-around at time t*. The corresponding mass m_{ta} at the turn-around time is given by

$$m_{\text{ta}}(t) = \left(\frac{3\pi}{4} \right)^{-2/3} \frac{4}{3}\pi \frac{5}{3}\delta_{a,i}\rho_i r_{a,i}\tau^{2/3}. \tag{2.75}$$

The self-similar solution for the mass shells accreting onto the black hole is described via λ, or the radius normalized by $r_{\text{ta}}(t)$:

$$\lambda = \frac{r}{r_{\text{ta}}(t)} = \sin^2 \frac{\theta}{2} \left(\frac{\theta - \sin\theta}{\pi} \right)^{-8/9}. \tag{2.76}$$

Both radius r and time t are now incorporated into λ, and therefore λ has two interpretations; radius of one particular mass shell, or a series of radii of all the mass shells. In what follows, we present the velocity, mass and density in the self-similar solution.

First, the self-similar description of velocity $V(\lambda)$ is defined by

$$\frac{dr}{dt} = \frac{r}{t} \frac{\sin\theta(\theta - \sin\theta)}{(1 - \cos\theta)^2} \equiv \frac{r_{\text{ta}}}{t} V(\lambda). \tag{2.77}$$

Note that V and λ are connected through θ. The top panel of Figure 2.2 illustrates V as a function of λ. For $\lambda \gg 1$, V asymptotically approaches to $(2/3)\lambda$, corresponding to the Hubble flow. In contrast, for $\lambda \ll 1$, $V \propto \lambda^{-1/2}$, which is expected for a particle freely falling onto a point mass.

Next, the mass $M(\lambda)$ in the self-similar solution is given by

$$m = \frac{4\pi}{3} \rho_m(t) r^3 \left[\frac{3}{4}(\theta - \sin\theta) \right]^2 \sin^{-6} \frac{\theta}{2} \equiv \frac{4\pi}{3} \rho_m(t) r_{\text{ta}}^3 M(\lambda). \tag{2.78}$$

The middle panel of Figure 2.2 shows M as a function of λ. In the limit of $\lambda \to 0$, M has a non-zero value:

$$M(0) \approx 3.497, \tag{2.79}$$

which is interpreted as the black hole mass. Since $m \propto t^{2/3} M$, the (dimensional) black hole mass grows as $t^{2/3}$. For $\lambda \gg 1$,

$$M(\lambda) \approx \lambda^3 + \frac{3}{5} \left(\frac{3\pi}{4} \right)^{8/3}. \tag{2.80}$$

Finally, the density $D(\lambda)$ in the self-similar solution is defined by

$$\rho = \rho_i \frac{r_i^2 dr_i}{r^2 dr} = \rho_m(t) \left[\frac{3}{4}(\theta - \sin\theta) \right]^2 \sin^{-6} \left(4 - \frac{9}{2} \frac{V(\lambda)}{\lambda} \right)^{-1} \equiv \rho_m(t) D(\lambda). \tag{2.81}$$

Note that, in the above, $r_i^2 dr_i / r^2 dr$ is calculated through

$$0 = d\tau = \left(\frac{\partial\tau}{\partial\delta_i} \frac{\partial\delta_i}{\partial r_i} + \frac{\partial\tau}{\partial y} \frac{\partial y}{\partial r_i} \right) dr_i + \left(\frac{\partial\tau}{\partial\delta_i} \frac{\partial\delta_i}{\partial r} + \frac{\partial\tau}{\partial y} \frac{\partial y}{\partial r} \right) dr. \tag{2.82}$$

The bottom panel of Figure 2.2 illustrates D as a function of λ. For $\lambda \ll 1$, $D \propto \lambda^{-3/2}$, while $\lambda \to 1$ for $\lambda \gg 1$.
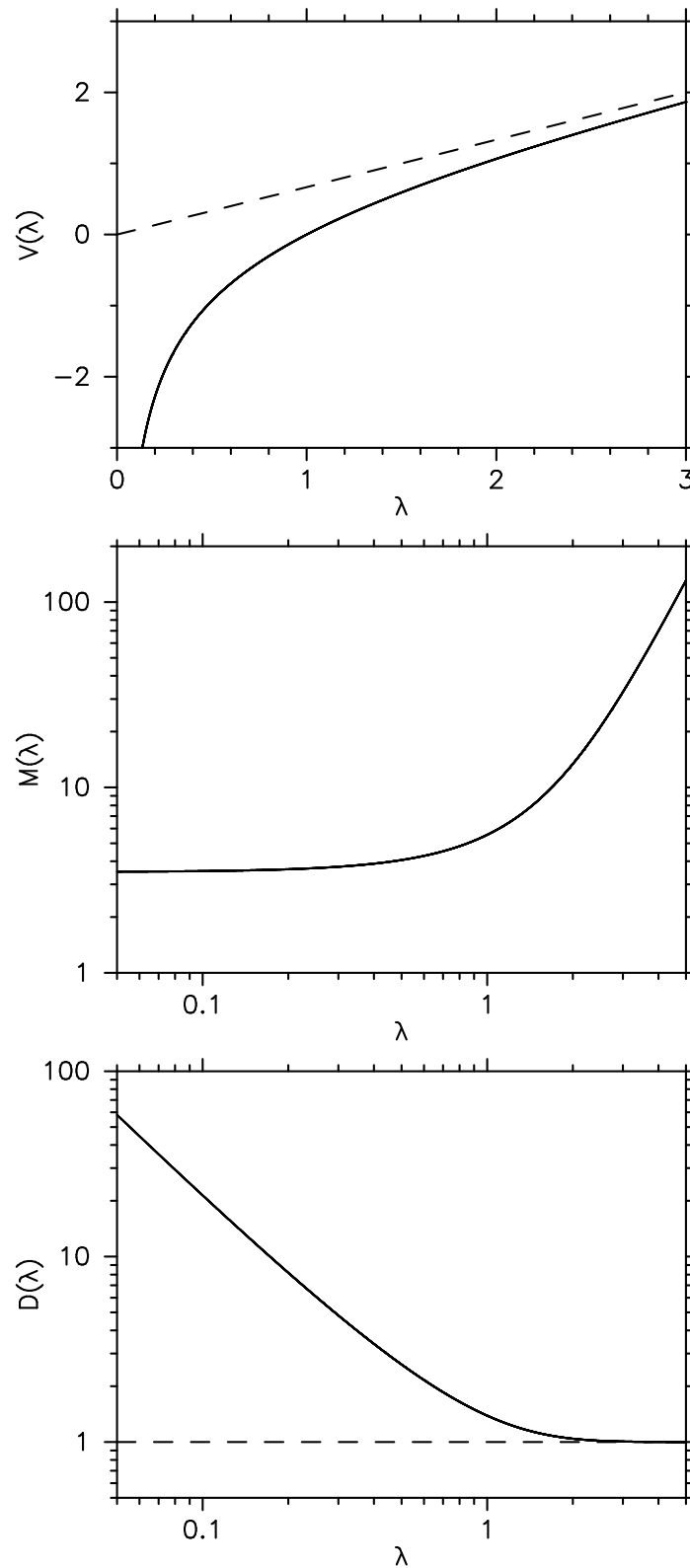
Figure 2.2: Velocity $V(\lambda)$ (top), Mass $M(\lambda)$ (middle) and Density $D(\lambda)$ (bottom) of dark matter mass shells in the self-similar accretion onto a black hole, as a function of $\lambda = r/r_{\mathrm{ta}}(t)$.

2.3.2 Collisionless infall

Now we describe the self-similar solution for collisionless infall with shell crossings. After a mass shell falls into the center, the shell turns back and then turns-around once again. Hence several mass shells can reside at a given radius at the same time.

We consider a mass shell that turns-around at $t = t_{\rm ta}$. The self-similar solution adopts $\lambda = r/r_{\rm ta}(t)$ and $\xi = \log(t/t_{\rm ta})$, where $r_{\rm ta}$ is defined by Equation (2.74). Importantly, $r_{\rm ta}(t)$ is not the turn-around radius of the mass shell under consideration, but the turn-around radius of another mass shell that turns around at time t.

Then the equation of motion is rewritten as

$$\frac{d^2\lambda}{d\xi^2} + \frac{7}{9}\frac{d\lambda}{d\xi} - \frac{8}{81}\lambda = -\frac{2}{9}\frac{\mu(\lambda)}{\lambda^2}, \tag{2.83}$$

where $\mu(\lambda)$ denotes the mass in the self-similar solution. Also, the initial conditions are $\lambda = 1$, $d\lambda/d\xi = -8/9$ at $\xi = 0$. The above equation of motion is only numerically solved. Since μ is not known in advance, the solution is iteratively derived by beginning with a trail function for μ.

The resulting $\lambda(\xi)$ is shown in Figure 2.3. The self-similarity enables us to interpret this figure in two ways; the time evolution of radius of a particular mass shell, or a snapshot for various mass shells at a fixed time. In the former picture, the figure shows a mass shell repeats infalls and turns-around, in principle, infinite times. In the latter picture, the figure indicates that several mass shells have the same λ at the same time, i.e., shell crossings are occurring.

Figure 2.4 illustrates $d\lambda/d\xi$ against λ, or the phase diagram. Due to the shell crossings, several shells can have the same λ with different $d\lambda/d\xi$. This yields non-zero velocity dispersions that is neglected in TSC. The dimensional velocity is given by

$$\frac{dr}{dt} = \frac{r_{\rm ta}}{t}\left(\frac{d\lambda}{d\xi} + \frac{8}{9}\lambda\right), \tag{2.84}$$

which satisfies $dr/dt = 0$ at $t = t_{\rm ta}$.

For the resulting $\lambda(\xi)$, the mass $\mu(\lambda)$ is given by

$$\mu(\lambda) = \frac{9\pi^2}{16}\sum_i (-1)^{i-1}\exp\left[-\frac{2}{3}\xi_i\right], \tag{2.85}$$

where ξ_i is the i-th point where $\lambda = \lambda(\xi)$. Figure 2.5 illustrates $\mu(\lambda)$. For $\lambda \ll 1$, $\mu \propto \lambda^{3/4}$.

Correspondingly, the density ϱ is calculated by

$$\varrho(\lambda) = \frac{1}{3\lambda^2}\frac{d\mu}{d\lambda} = \frac{\pi^2}{4\lambda^2}\sum_i (-1)^i \exp\left[-\frac{2}{3}\xi_i\right]\left(\frac{d\lambda}{d\xi}\right)^{-1}, \tag{2.86}$$

and shown in Figure 2.5. Note that the cusps in the figure have , in principle, $\varrho = \infty$. The positions of cusps correspond to λ where a mass shell collapses. For $\lambda \ll 1, \varrho \propto \lambda^{-9/4}$.

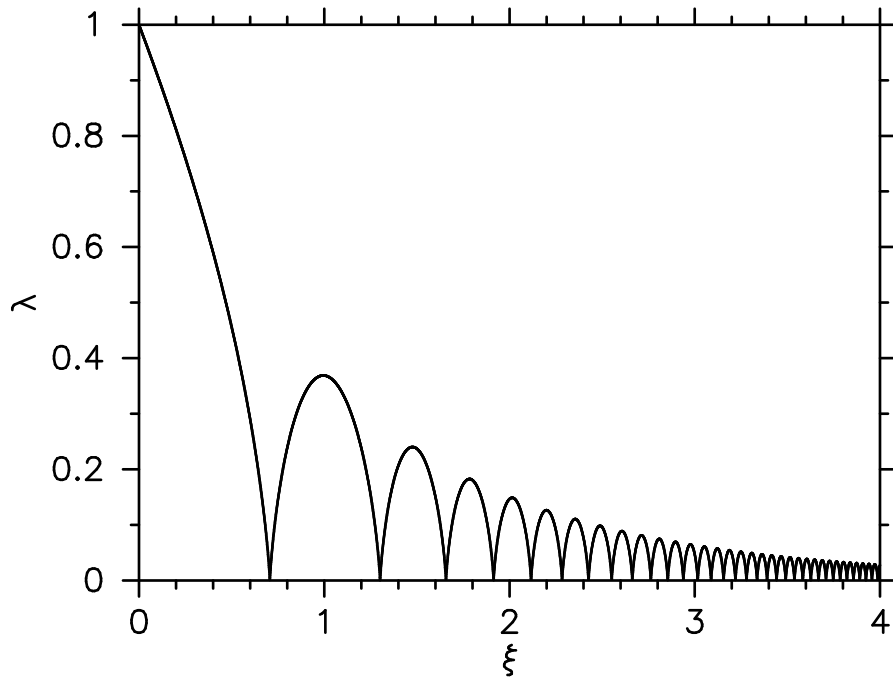Figure 2.3: The self-similar solution $\lambda = r/r_{\mathrm{ta}}$ for the collisionless infall as a function of $\xi = \log(t/t_{\mathrm{ta}})$.
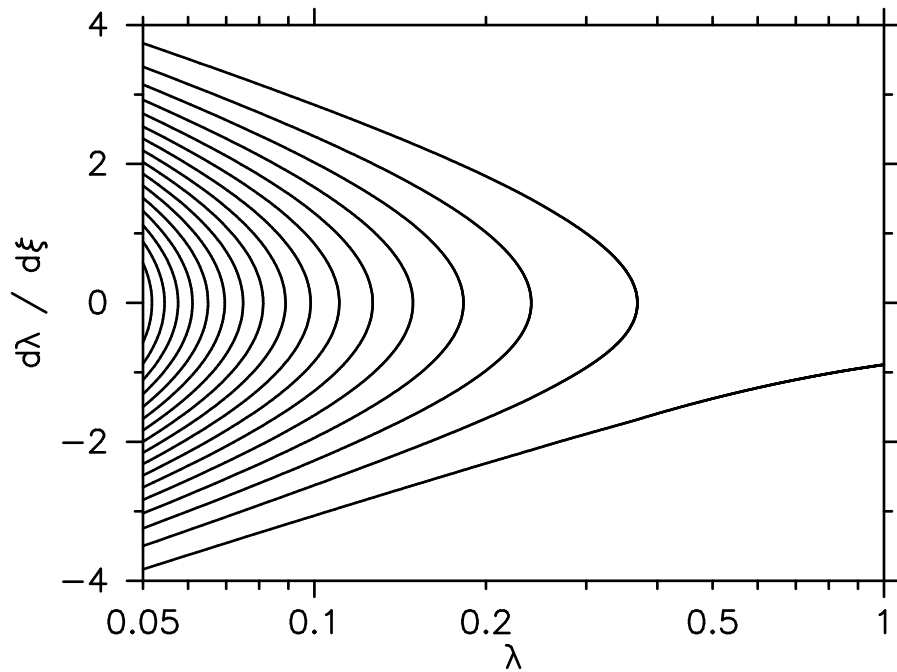

Figure 2.4: Phase diagram of the self-similar solution for the collisionless infall; $d\lambda/d\xi$ against λ.
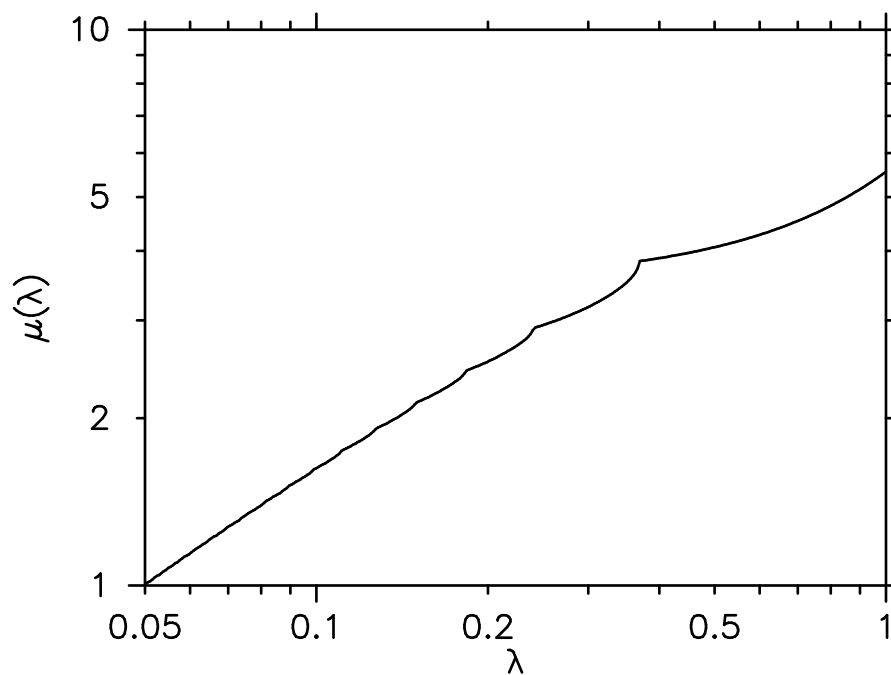
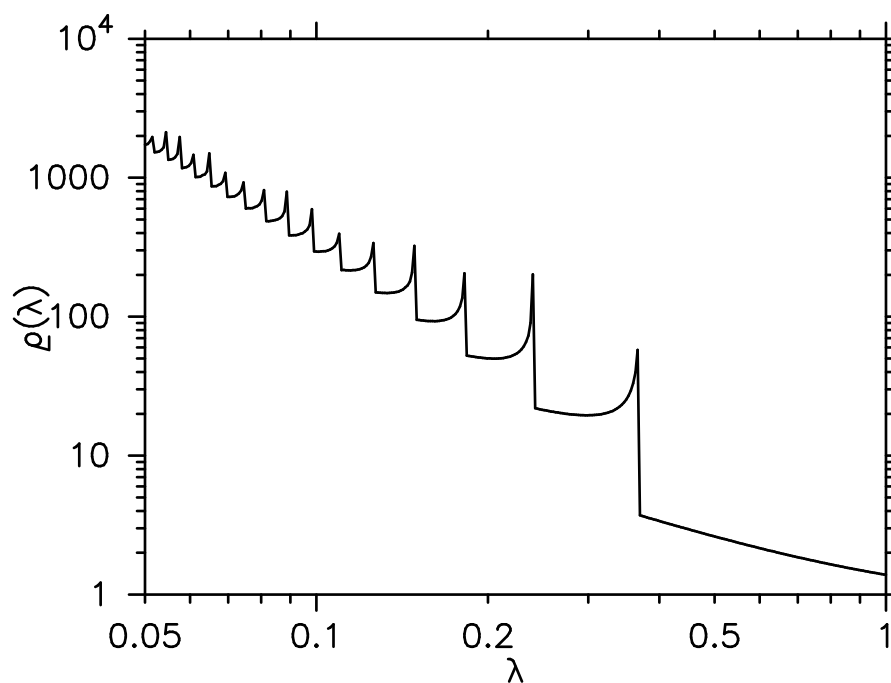Figure 2.5: Mass profile $\mu(\lambda)$ of the self-similar solution.

Figure 2.6: Density profile $\varrho(\lambda)$ of the self-similar solution.

2.4 Virialized State of Dark Matter Halos — Łokas & Mamon Model

The top-hat spherical collapse models predict that a sphere always keeps the homogeneity of density. The self-similar solution by Fillmore & Goldreich (1984) and Bertschinger (1985) describes a non-uniform density profile, but it is different from the NFW density profile that is common in dark matter halos both in simulations and in observations.

Although there is no theoretical model to describe the formation of the NFW profile (the origin of the NFW profile itself is still unknown), the viriazlied state with the NFW profile has been provided by Łokas & Mamon (2001). Since the method of Łokas & Mamon (2001) is applicable to any *spherically symmetric* systems, in this section, we consider the uniform density profile, in addition to the NFW profile.

For a given density profile $\rho(r)$, the gravitational potential $\phi(r)$ is given through the Poisson equation by

$$\phi(r) = -4\pi G \left[\frac{1}{r} \int_0^r \rho(r') r'^2 dr' + \int_r^\infty \rho(r') r' dr' \right]. \tag{2.87}$$

Using the above potential and the density, the dispersion profile of the radial velocity σ_r^2 is obtained from the static Jeans equation:

$$\frac{1}{\rho} \frac{d}{dr} (\rho \sigma_r^2) + 2\beta \frac{\sigma_r^2}{r} = -\frac{d\phi}{dr}, \tag{2.88}$$

where the velocity anisotropy $\beta (= 1 - \sigma_t^2 / 2\sigma_r^2)$. It is the essential point of this model that the virialized state is regarded as a static solution of the Jeans equation. Here *beta* in general depends on radius, but we assume for simplicity that β is constant.

Using the total velocity dispersion $\sigma^2 = \sigma_r^2 (3 - 2\beta)$, the kinetic energy $K(r)$ and the potential energy $W(r)$ inside the radius r are given by

$$K(r) = \frac{1}{2} \int_0^r 4\pi \rho(r) \sigma^2(r) r^2 dr, \tag{2.89}$$

$$W(r) = -G \int_0^r 4\pi \rho(r) M(r) r dr, \tag{2.90}$$

where $M(r)$ is the mass inside the radius r. Then we obtain the virial ratio $2K/|W|$.

2.4.1 Uniform density

We consider the uniform density profile:

$$\rho(r) = \begin{cases} \rho_0 & ; & r \le a \\ 0 & ; & r > a \end{cases} \tag{2.91}$$

In this case, the gravitational potential $\phi(r)$ is given by

$$\phi(r) = \begin{cases} -\dfrac{GM_a}{a} \left(\dfrac{3}{2} - \dfrac{1}{2} \dfrac{r^2}{a^2} \right) & ; & r \le a \\ -\dfrac{GM_a}{r} & ; & r > a, \end{cases} \tag{2.92}$$

where $M_a = 4\pi a^3 \rho_0/3$. Then the static Jeans equation yields

$$\sigma_r^2(r) = \frac{1}{1+\beta}\frac{GM_a}{2a}\left[\left(\frac{r}{a}\right)^{-2\beta} - \left(\frac{r}{a}\right)^2\right], \qquad (2.93)$$

for $r \leq a$. Here we set the boundary condition $\sigma_r^2 = 0$ at $r - a$, and so $\sigma_r^2 = 0$ outside $r = a$.

Then the kinetic energy K inside $r = a$ becomes

$$K(r) = \frac{3(3-2\beta)}{4(1+\beta)}\frac{GM_a^2}{a}\left[\frac{1}{3-2\beta}\left(\frac{r}{a}\right)^{3-2\beta} - \frac{1}{5}\left(\frac{r}{a}\right)^5\right] \qquad (r \leq a). \qquad (2.94)$$

In addition, the potential energy is

$$W(r) = -\frac{3}{4}\frac{GM_a^2}{a}\left[1 - \frac{1}{5}\left(\frac{r}{a}\right)^2\right] \qquad (r \leq a). \qquad (2.95)$$

Note that $W(r) = 0$ for $r > a$ since $\rho = 0$.

For any β, $2K/|W| = 1$ at $r = a$. This is because we have set the boundary condition $\sigma_r^2 = 0$ at $r = a$, and so the surface pressure term becomes zero in the virial theorem (2.28).

2.4.2 NFW density profile

The density of virialized halos at the present time is not uniform. In fact, Navarro et al. (1995, 1996, 1997) have found a universal profile for the spherically averaged density of simulated halos, called the Navarro-Frenk-White (NFW) profile:

$$\rho(r) = \frac{\rho_0 c^3 g(c)}{3}\frac{1}{cs(1+cs)^2}, \qquad (2.96)$$

where $s = r/r_s$ is the radius normalized by the scale radius r_s, $c = r_v/r_s$ is the concentration parameter characterized by the virial radius r_v, and

$$g(c) = \left[\log(1+c) - \frac{c}{1+c}\right]^{-1}. \qquad (2.97)$$

Here we basically follow the notation of Łokas & Mamon (2001). In this subsection, we consider the energy terms in the viriaized state with the NFW profile, according to Łokas & Mamon (2001).

The mass $M(s)$ inside s is obtained by integrating the density profile:

$$M(s) = M_v g(c)\left[\log(1+cs) - \frac{cs}{1+cs}\right], \qquad (2.98)$$

where

$$M_v = \frac{4\pi}{3}\rho_0 r_v^3. \qquad (2.99)$$

Then the (specific) gravitational potential $phi(s)$ is given by

$$\frac{\phi(s)}{V_v^2} = -g(c)c\frac{\log(1+cs)}{cs}, \tag{2.100}$$

where

$$V_v^2 = \frac{GM_v}{r_v} = \frac{4\pi}{3}G\rho_0 r_v^2 \tag{2.101}$$

is the circular velocity.

Solving the static Jeans equation, one obtains the velocity dispersion σ_r^2. Unlike the case of the uniform density profile, the solution cannot be written in a common form for arbitrary β. Hence we specifically provide the solution for $\beta = 0$, $1/2$ and 1.

$$\frac{\sigma_r^2}{V_v^2}(s;\beta=0) = \frac{1}{2}cg(c)cs(1+cs)\left[\pi^2 - \log(cs) - \frac{1}{cs} - \frac{1}{(1+cs)^2} - \frac{6}{1+cs}\right.$$
$$\left. + \left(1 + \frac{1}{c^2s^2} - \frac{4}{cs} - \frac{2}{1+cs}\right)\log(1+cs) + 3\log^2(1+cs) + 6\operatorname{Li}_2(-cs)\right], \tag{2.102}$$

$$\frac{\sigma_r^2}{V_v^2}(s;\beta=1/2) = cg(c)(1+cs)^2\left[-\frac{\pi^2}{3} + \frac{1}{2(1+cs)^2} + \frac{2}{1+cs}\right.$$
$$\left. + \frac{\log(1+cs)}{cs} + \frac{\log(1+cs)}{1+cs} - \log^2(1+cs) - 2\operatorname{Li}_2(-cs)\right] \tag{2.103}$$

and

$$\frac{\sigma_r^2}{V_v^2}(s;\beta=1) = g(c)(1+cs)^2\frac{1}{cs}\left[\frac{\pi^2}{6} - \frac{1}{2(1+cs)^2} - \frac{1}{1+cs}\right.$$
$$\left. - \frac{\log(1+cs)}{1+cs} + \frac{\log^2(1+cs)}{2} + \operatorname{Li}_2(-cs)\right], \tag{2.104}$$

where

$$\operatorname{Li}_2(x) = \int_x^0 \frac{\log(1-t)}{t} \tag{2.105}$$

is the dilogarithm function. Accordingly, the kinetic energy $K(s)$ is given as follows:

$$K(s,\beta=0) = \frac{1}{2}W_\infty\left[-3 + \frac{3}{1+cs} - 2\log(1+cs) + cs\left(5 + 3\log(1+cs)\right)\right.$$
$$\left. -c^2s^2\left(7 + 6\log(1+cs)\right) + c^3s^3\left(\pi^2 + \log\frac{1+cs}{cs} + 3\log^2(1+cs) + 6\operatorname{Li}_2(-cs)\right)\right], \tag{2.106}$$

$$K(s,\beta=1/2) = \frac{1}{3}W_\infty\left[-3 + \frac{3}{1+cs} - 3\log(1+cs) + 6cs\left(1 + \log(1+cs)\right)\right.$$
$$\left. -c^2s^2\left(\pi^2 + 3\log^2(1+cs) + 6\operatorname{Li}_2(-cs)\right)\right] \tag{2.107}$$

29

and

$$K(s, \beta = 1) = \frac{1}{2} W_\infty \left[-2\log(1 + cs) + cs \left(\frac{\pi^2}{3} - \frac{1}{1 + cs} + \log^2(1 + cs) + 2\,\mathrm{Li}_2(-cs) \right) \right],$$

(2.108)

where

$$W_\infty = \frac{cg^2(c)GM_v^2}{2r_v}.$$

(2.109)

The potential energy is given by

$$W(s) = -W_\infty \left[1 - \frac{1}{(1 + cs)^2} - \frac{2\log(1 + cs)}{1 + cs} \right].$$

(2.110)
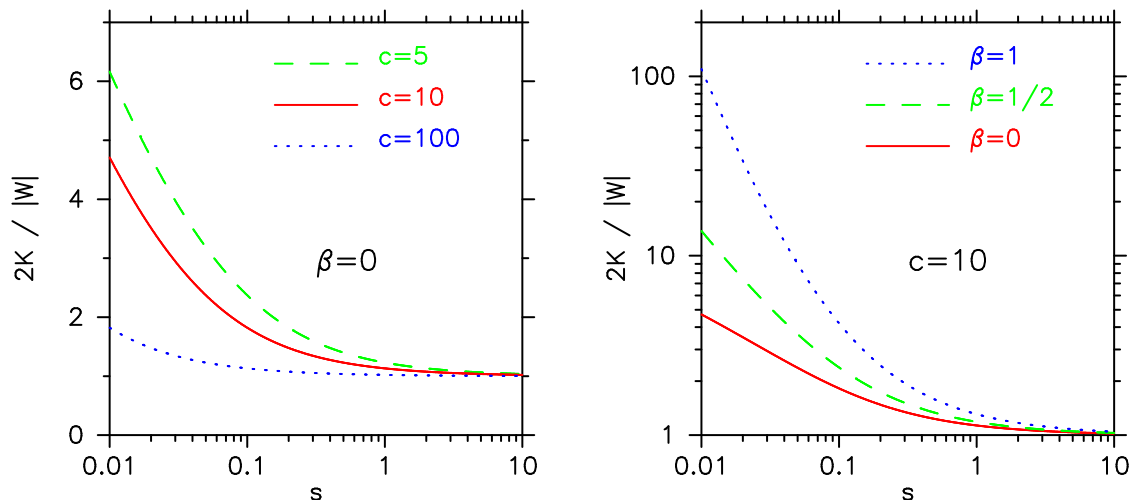
Figure 2.7: Ratio of the kinetic energy K to the potential energy W. The left panel illustrates $2K/|W|$ with the velocity anisotropy parameter $\beta = 0$, for the three different values of concentration parameter c; $c = 5$ (green dashed), $c = 10$ (red solid), $c = 100$ (blue dotted). The right panel shows $2K/|W|$ with c is fixed to 10, for the three different values of β; $\beta = 0$ (red solid), $\beta = 1/2$ (green dashed), $\beta = 1$ (blue dotted). Note that the red curves in the two panels are identical.

Figure 2.7 demonstrates the solutions with $\beta = 0$ and three different values of c (left), and with $c = 10$ and three different values of β (right). Compared to c, the solution strongly depends on β, especially in inner regions. In general, $2K/|W|$ is not necessarily unity because the surface pressure term in the virial theorem (2.28) does not vanish.

In observations and simulations, the virialized region of a halo is conventionally determined based on the spherically averaged overdensity. In particular, the radius r_{200} inside which the averaged overdensity is 200 times the cosmic critical density, is widely used as the virial radius of a galaxy cluster. This is motivated by the fact that, in the top-hat spherical model in the EdS universe, the virial overdensity is given by $\Delta_{\mathrm{vir}} \approx 177.7$, independent of the collapse time. As Figure 2.7 indicates, however, $2K/|W|$ does not have a special value at $r_{200} \approx r_v$. Hence r_{200}, or a radius defined by overdensity does not represent the virial region of halos. This point will be revisited in Chapter 4.

Chapter 3

Non-spherical Modelling of Dark Matter Halos; Ellipsoidal Collapse Model, Simulations and Observations

In this chapter, we present the previous studies from the aspects of theory, simulations and observations. In particular, we pay a special attention to the work by Rossi et al. (2011) who found a discrepancy between simulations and theory, in the probability distribution function (PDF) of axis ratio of triaxial halos. Their finding strongly motivates our researches, especially the one in Chapter 5.

We reproduce the work by Rossi et al. (2011) in Section 3.4. In preparation for that, we first describe the theoretical models for the non-sphericity of halos, i.e., the Gaussian random initial conditions(Section 3.1) and the ellipsoidal collapse model (Section 3.2). These models give a purely theoretical prediction for PDF of axis ratio of triaxial halos. Then, in Section 3.3, we present the work by Jing & Suto (2002) who found a universal PDF of axis ratio of triaxially-modelled simulated halos. The work by Rossi et al. (2011) is based on the theoretical models in Sections 3.1 and 3.2, and the simulation results described in Section 3.3.

Finally, in Section 3.5, we describe the previous observation studies on the non-sphericity of actual clusters by Oguri et al. (2010) (weak-lensing) and Kawahara (2010) (X-ray) who compared their own observation data with the prediction of Jing & Suto (2002).

3.1   Gaussian Random Initial Conditions

Theoretically, the non-sphericity of dark matter halos is already imprinted in primordial density fluctuations, conventionally described by the Gaussian random field (Doroshkevich, 1970; Bardeen et al., 1986).

The primordial density fluctuations are characterized by the eigenvalues λ_k ($k = 1$, 2, 3; $\lambda_1 > \lambda_2 > \lambda_3$) of the tensor $(4\pi G\bar{\rho}a^3)^{-1}\nabla_i\nabla_j\phi$. The overdensity δ is related to λ_k through

$$\delta = \lambda_1 + \lambda_2 + \lambda_3, \tag{3.1}$$

and ellipticity e and prolate p of the density field are given by

$$e = \frac{\lambda_1 - \lambda_3}{2\delta} \quad , \quad p = \frac{\lambda_1 + \lambda_3 - 2\lambda_2}{2\delta}. \tag{3.2}$$

By definition, $-\infty < e < \infty$ and $-e < p < e$. In addition, $e > 0$ for $\delta > 0$ and $e < 0$ for $\delta < 0$.

For a given variance σ^2 of the density fluctuations, Doroshkevich (1970) derived the probability distribution $\wp$ for δ, e and p:

$$\wp(\delta, e, p; \sigma) = \frac{1}{\sqrt{2\pi\sigma^2}} \exp\left(-\frac{\delta^2}{2\sigma^2}\right) \frac{1125}{\sqrt{10\pi}} e(e^2 - p^2) \left(\frac{\delta}{\sigma}\right)^5 \exp\left[-\frac{5}{2}\frac{\delta^2}{\sigma^2}(3e^2 + p^2)\right]. \tag{3.3}$$

Integrating $\wp$ over all the possible e and p simply reduces to an ordinary Gaussian function for δ:

$$\int_{-\infty}^{\infty} de \int_{-e}^{e} dp \; \wp(\delta, e, p; \sigma) = \frac{1}{\sqrt{2\pi\sigma^2}} \exp\left(-\frac{\delta^2}{2\sigma^2}\right). \tag{3.4}$$

This is fully expected since the distribution $\wp$ is constructed base on the assumption that the probability distribution of δ follows a Gaussian function.

To clarify how the ellipticity e depends on σ (or mass), we integrate the distribution $\wp$. First, integrating $\wp$ over $-e < p < e$ reduces to the following:

$$\int_{-e}^{e} dp \; \wp(\delta, e, p; \sigma) = \frac{9\sqrt{5}e}{2\pi\sigma} \exp\left[-\frac{\delta^2}{2\sigma^2} - 10\left(\frac{e\delta}{\sigma}\right)^2\right]\left(\frac{\delta}{\sigma}\right)^2$$

$$\times \left[10\frac{e\delta}{\sigma} + \sqrt{10\pi}\exp\left\{\frac{5}{2}\left(\frac{e\delta}{\sigma}\right)^2\right\}\left\{5\left(\frac{e\delta}{\sigma}\right)^2 - 1\right\}\mathrm{erf}\left(\sqrt{\frac{5}{2}}\frac{e\delta}{\sigma}\right)\right]. \tag{3.5}$$

Furthermore, integration over $0 < \delta < \infty$ yields

$$\int_0^{\infty} d\delta \int_{-e}^{e} dp \; \wp(\delta, e, p; \sigma) = \frac{45e}{\pi(1 + 15e^2)^2}$$

$$\times \left[\frac{\sqrt{5}e(1 + 30e^2)}{1 + 20e^2} - \frac{1}{(1 + 15e^2)^{1/2}}\tan^{-1}\sqrt{\frac{5e^2}{1 + 15e^2}}\right]. \tag{3.6}$$

The above expression does not include σ, and therefore the ellipticity e does not depend on mass *when $\wp$ is integrated over all the possible δ*.

We are interested, however, in the mass dependence of e for the regions that eventually become dark matter halos by the present time. Hence we integrate Equation (3.5) over $\delta_c < \delta < \infty$, where $\delta_c = 1.68$ is the linearly-extrapolated density contrast in the top-hat spherical collapse model. Then the resulting function now depends on σ.

Figure 3.1 illustrates $\int_{1.68}^{\infty} d\delta \int_{-e}^{e} dp \; \wp$ for three different values of σ; $\sigma = 2.0$ (blue), $\sigma = 1.5$ (green), $\sigma = 1.0$ (red). Note that larger σs correspond to less massive regions. For comparison, Equation (3.6) is also plotted in the black dashed curve. Importantly, Figure 3.1 indicates that *more massive regions (with smaller σ) tend to have smaller ellipticity*

e in the Gaussian random initial conditions. This point will be revisited when we discuss the discrepancy in the mass dependence of non-sphericity of halos at the present time between simulations and theory.
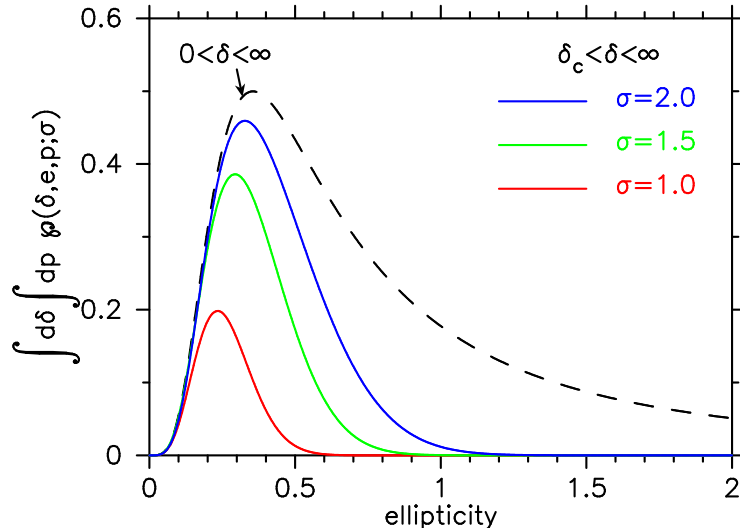
Figure 3.1: Probability distributions of e as a result of $\int d\delta d\delta \int_{-e}^{e} dp \, \wp$. Integration over $0 < \delta < \infty$ yields the black dashed curve, independent of σ. If we change the lower limit of integration to $\delta_c = 1.68$, the result depends on σ, and the probability distributions of e for $\sigma = 2.0, 1.5, 1.0$ are shown in blue, green and red, respectively.

3.2 Ellipsoidal Collapse Model

A conventional theoretical model to describe the evolution of non-spherical primordial density fluctuations is the ellipsoidal collapse model (hereafter EC White & Silk, 1979; Bond & Myers, 1996). In this section, we summarize the basic framework of EC. We adopt the notation of Rossi et al. (2011).

EC describes the evolution of a homogeneous ellipsoid, embedded with a tidal field. The tidal field is characterized by the eigenvalues of the tensor $\nabla_{ij}\phi/(4\pi G\bar{\rho}a^3)$, where ϕ, $\bar{\rho}$ and a denote the gravitational potential, the mean matter density, and the scale factor, respectively. The differentiation by ∇_{ij} is operated in the comoving coordinate system. We denote the eigenvalues of the tensor by λ_k ($k = 1, 2, 3$; $\lambda_1 \geq \lambda_2 \geq \lambda_3$).

In the linear regime, the density contrast δ is given by $\sum_k \lambda_k$, and λ_k, δ and ϕ grow in proportion to the linear growth rate $D(t)$. Therefore, at the initial time t_{ini} where the linear regime holds, the axis lengths of the ellipsoid A_k ($k = 1, 2, 3$) satisfy the following equations:

$$A_k(t_{\text{ini}}) = a(t_{\text{ini}})(1 - \lambda_k(t_{\text{ini}})) \tag{3.7}$$

and

$$\frac{dA_k(t_{\text{ini}})}{dt} = H(t_{\text{ini}}) \left[A_k(t_{\text{ini}}) - a(t_{\text{ini}})\lambda_k(t_{\text{ini}}) \left. \frac{d\ln D}{d\ln a} \right|_{t=t_{\text{ini}}} \right], \tag{3.8}$$

where $H(t)$ is the Hubble parameter.

Then the axis lengths A_k evolve according to the following equation of motion:

$$\frac{d^2 A_k(t)}{dt^2} = \Omega_{\Lambda,0} H_0^2 A_k(t) - 4\pi G \bar{\rho}(t) A_k(t) \left[\frac{1 + \delta(t)}{3} + \frac{b'_k \delta(t)}{2} + \lambda'_{\text{ext},k}(t) \right]. \qquad (3.9)$$

The above equation of motion implies that the ellipsoid does not rotate with respect to the tidal field. Therefore the relation $A_3 \geq A_2 \geq A_1$ is conserved all the time since $\lambda_1 \geq \lambda_2 \geq \lambda_3$ at the initial time.

In the equation of motion (3.9), the interior tidal force b'_k within the ellipsoids is computed by

$$b'_k(t) = \prod_j A_j(t) \int_0^\infty \frac{d\tau}{(A_k^2(t) + \tau) \prod_j \sqrt{A_j^2(t) + \tau}} - \frac{2}{3}. \qquad (3.10)$$

Also, the exterior tidal force $\lambda'_{\text{ext},k}$ is described by

$$\lambda'_{\text{ext},k}(t) = \frac{D(t)}{D(t_{\text{ini}})} \left[\lambda_k(t_{\text{ini}}) - \frac{\delta(t_{\text{ini}})}{3} \right]. \qquad (3.11)$$

Equation (3.10) is the exact expression only for the homogeneous density as considered here. On the other hand, Equation (3.11) assumes the exact linear growth regime even when the later evolution may not be the case. Unlike $\lambda'_{\text{ext},k}$, the density contrast $\delta(t)$ is calculated at each time so that the mass inside the ellipsoid $(4\pi\bar{\rho}/3)(1 + \delta)A_1 A_2 A_3$ is constant. For the spherical case ($\lambda_1 = \lambda_2 = \lambda_3 = \delta_{\text{ini}}/3$ and $A_1 = A_2 = A_3 = R$), both b'_k and $\lambda'_{\text{ext},k}$ vanish, and the equation of motion simply reduces to $d^2 R/dt^2 = \Omega_{\Lambda,0} H_0^2 R - (4\pi/3)G\bar{\rho}(1 + \delta)R$.

According to Equation (3.9), all the axis lengths A_k eventually collapse to zero, as in the spherical case. Therefore an additional assumption is needed to predict the eventual axis lengths A_k. In the spherical collapse model, it is conventionally assumed that the final (virial) radius r_{vir} and overdensity Δ_{vir} of a homogeneous sphere are computed from the virial theorem.

In the case of EC, however, there may be no widely accepted treatment of anisotropic virialization of different axes. In this paper, we adopt the one proposed by Bond & Myers (1996). They assumed each A_k *separately* stops collapsing when A_k reaches $a(t) \times (\Delta_{\text{vir}})^{-1/3}$, using the virial overdensity $\Delta_{\text{vir}}(z = 0)$ in the *spherical* virial theorem. Such an ellipsoid corresponds to a halo which is virialized at $z = 0$.

In summary, EC describes the evolution of a homogeneous and isolated ellipsoid, based on the liner growth of density fluctuations. The treatment of the virialization is based on the non-trivial assumption that each axis separately virialize; the axis lengths A_k at low redshifts ($z \lesssim 1$) are determined mainly by this virialization criterion.

3.3 Probability Distribution for Non-sphericity of Simulated Halos

One of the most important findings in simulations studies on the non-sphericity of dark matter halos is brought about by Jing & Suto (2002). They fitted triaxial ellipsoids withe

with axis length A_1, A_2, A_3 ($A_1 \leq A_2 \leq A_3$) to isodensity surfaces of their simulated halos. Then they found the following universal probability distribution functions (PDFs) for axis ratios A_1/A_3 and A_2/A_3:

$$p(A_1/A_3; M_{200}, z) = \frac{(M_{200}/M_*)^{0.07[\Omega_m(z)]^{0.7}}}{\sqrt{2\pi}0.113} \exp\left[-\frac{[A_1/A_3(M_{200}/M_*)^{0.07[\Omega_m(z)]^{0.7}} - 0.54]^2}{2(0.113)^2}\right],$$
(3.12)

and

$$p(A_2/A_3; A_1/A_3) = \frac{3}{2(1-\omega)}\left[1 - \left(\frac{2A_2/A_3 - 1 - \omega}{1-\omega}\right)^2\right],$$
(3.13)

where $\omega = \max(A_1/A_3, 0.5)$, and M_* is the characteristic non-linear mass scale at which the rms top-hat smoothed overdensity becomes $\delta_{\mathrm{lin,col}} = 1.68$. The PDF (3.12) states that more massive halos tend to be less spherical, although the mass dependence is very weak. More recently, Bonamigo et al. (2015) and Vega et al. (2016) constructed PDFs of axis ratios by using their simulated halos with higher resolution in a wider mass range, they still found that more massive halos tend to be less spherical.

The PDFs (3.12) and (3.13) are based on the isodensity contour at $\rho = 100\rho_c$. Jing & Suto (2002) assumed, for simplicity, that the density distribution of halos are "self-similar", i.e., the isodensity surfaces follow a set of ellipsoids with the same axis ratio and the same central position. They also showed, however, that that their halos are actually not necessarily self-similar; the self-similarity was assumed just for simplicity. Based on the self-similarity assumption, Jing & Suto (2002) normalize the PDFs for $\rho = 100\rho_c$ by M_{200}. Note that the "self-similarity" of the density distribution of dark matter halos should not be confused with the "self-similar" solution of spherical collapse in Section 2.3.

The PDFs (3.12) and (3.13) have been widely used as a reference to compare with theoretical models and with observation data. Among them, we present the studies by Rossi et al. (2011), Oguri et al. (2010) and Kawahara (2010) that strongly motivate this thesis.

3.4 Discrepancy between EC and Simulation Results

Rossi et al. (2011) solved the ellipsoidal collapse model (EC, Section 3.2) with the Gaussian random initial conditions (3.1). Then they calculated the PDF of the axis ratio A_1/A_3. The resulting PDF is, in a sense, a purely theoretical prediction.

They found that the results from EC and the Gaussian random field state that more massive halos tend to be more spherical, keeping the mass dependence at the initial time. In contrast, as stated in the previous section, the PDF (3.12) of Jing & Suto (2002) (hereafter JS02) predicts that more massive halos are less spherical.

Figure 3.2 is a reproduction of the work of Rossi et al. (2011). The figure shows the PDF of JS02 (black curve) and the PDF calculated from EC with the Gaussian random initial conditions (red histogram) for three different mass ranges; $10^{13}M_\odot < M < 10^{14}M_\odot$ (top), $10^{14}M_\odot < M < 10^{15}M_\odot$ (middle), $M > 10^{15}M_\odot$ (bottom). Indeed, while the theoretical prediction is shifted to the *right* at heavier mass ranges, the PDF of JS02 is shifted to the *left* at heavier mass ranges.

This manifests the discrepancy between the theory and the simulations, although the mass dependence itself is very weak. In Chapter 4, we try to better understand the discrepancy by following the evolution of the non-sphericity of individual simulated halos.
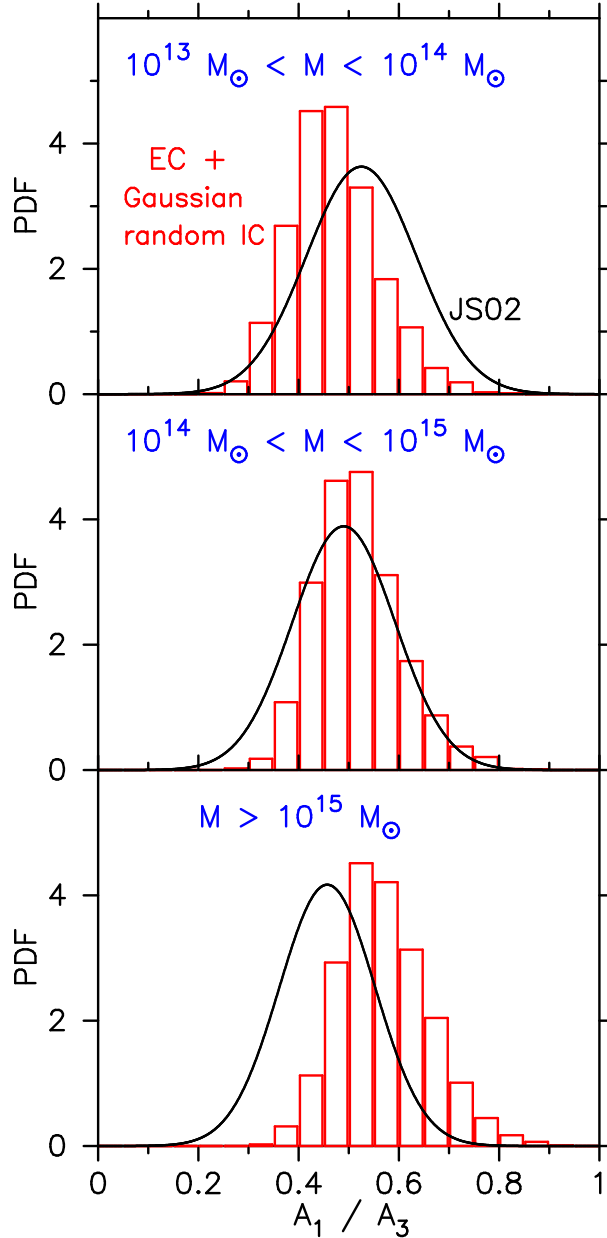
Figure 3.2: Comparison between the PDF of axis ratio A_1/A_3 of dark matter halos at $z = 0$ predicted by Jing & Suto (2002) from their simulations (black curve), and the one calculated from the Gaussian random initial conditions via EC (red histogram), for the three different mass ranges; $10^{13} M_\odot < M < 10^{14} M_\odot$ (top), $10^{14} M_\odot < M < 10^{15} M_\odot$ (middle), $M > 10^{15} M_\odot$ (bottom). For both PDFs, the same cosmological parameters are chosen as Jing & Suto (2002); $\Omega_{m,0} = 0.3$, $\Omega_{\Lambda,0} = 0.7$, $h = 0.7$, $\sigma_8 = 0.9$.

3.5 Observational Studies on Non-sphericity of Halos

Comparisons of the PDF (3.12) of Jing & Suto (2002) (JS02) with observation data have been already implemented, although the number of available data is limited at this stage. In the later chapters, we compare our simulation results with observation data by Oguri et al. (2010) in the weak lensing analysis, and by Kawahara (2010) in the X-ray observations. Here we briefly summarize their analysis methods and results.

3.5.1 Weak lensing

Oguri et al. (2010) anaylized Subaru/Suprime-cam observation data for 18 galaxy clusters with the mean redshift $z \sim 0.23$ and the mean mass $M_{\mathrm{vir}} \sim 7 \times 10^{14} M_{\odot}$. They estimated the axis ratio of the shear map of the clusters assuming the cluster density in the three-dimensional space follows the self-similar "elliptical NFW" profile:

$$\rho(R_e) = \frac{\rho_0}{(R_e/R_s)(1 + R_e/R_s)^2}, \tag{3.14}$$

where

$$R_e^2 = A_3^2 \sum_{i=1}^{3} \frac{x_i^2}{\tau + A_i^2}. \tag{3.15}$$

Note that the density profile is self-similar (concentric, common axis ratios) if and only if the density can be written as a function of R_e alone.

Since the observed density distribution is projected on the sky, a PDF of *projected* axis ratio based on Equation (3.12) is needed in order to compare the observation data with the simulation results. Oguri et al. (2010) adopted the PDF of projected axis ratio calculated by Oguri et al. (2003) described in what follows.

For the axis ratios $\mu_{13} = A_1/A_3$ and $\mu_{23} = A_2/A_3$ that follow the PDFs (3.12) and (3.13), the axis ratio $q = a_1/a_2$ of the projected ellipse with axis length a_1 and a_2 ($a_1 \leq a_2$) is obtained by (Binney, 1985)

$$q(\theta, \phi; \mu_{13}, \mu_{23}) = \sqrt{\frac{A + C - \sqrt{(A - C)^2 + B^2}}{A + C + \sqrt{(A - C)^2 + B^2}}} \tag{3.16}$$

where

$$
\begin{aligned}
A &= \mu_{13}^{-2} \cos^2 \theta \left(\sin^2 \varphi + \mu_{23}^{-2} \cos^2 \varphi \right) + \mu_{23}^{-2} \sin^2 \theta, \\
B &= \mu_{13}^{-2} \left(1 - \mu_{23}^{-2} \right) \cos \theta \sin 2\varphi, \\
C &= \mu_{13}^{-2} \left(\mu_{23}^{-2} \sin^2 \varphi + \cos^2 \varphi \right)
\end{aligned}
$$

and θ and φ represent the spherical coordinates with the axis set to the line-of-sight. For the uniform distribution of (θ, φ) and sets of (A_1, A_2, A_3) that follows the PDFs (3.12) and (3.13), one can calculate the PDF of axis ratio q of the projected isopotential surfaces.

Oguri et al. (2010) compare the above PDF of projected axis ratio with their observation data. Figure 3.3 reproduces the comparison. The red symbols indicate the observation data, and the blue solid curve shows the PDF of projected axis ratio by

Oguri et al. (2003). Oguri et al. (2010) further convolved the PDF of Oguri et al. (2003) with the Gaussian function ($\sigma = 0.15$), in order to incorporate the typical error in estimates of axis ratio q. The result is shown in the blue dashed curve. Given the large uncertainty, they concluded the observation data and the simulation results are barely consistent.
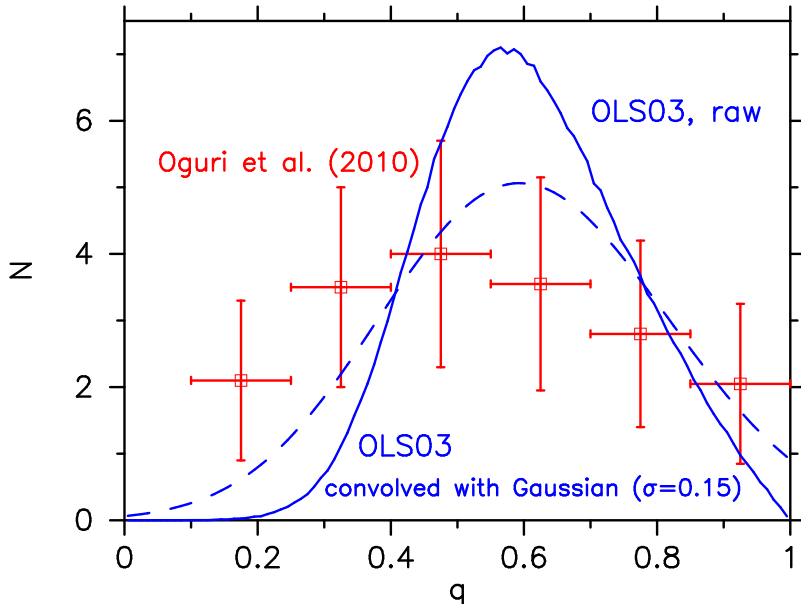
Figure 3.3: Comparison of the weak lensing data by Oguri et al. (2010) (red symbols with error bars) and the prediction by Oguri et al. (2003) (blue solid curve). The prediction of Oguri et al. (2003) is convolved with the Gaussian function ($\sigma = 0.15$) to incorporate the horizontal errors, and plotted in the blue dashed curve.

3.5.2   X-ray

While the gravitational lensing analyses directly estimate the projected total density distribution of galaxy clusters, X-ray surface brightness of intracluster gas also provides the information on the dark matter density distribution, assuming that the gas distribution is correlated with the dark matter distribution.

Kawahara (2010) fitted ellipses to the X-ray surface brightness maps of galaxy clusters observed by *XMM-Newton* (Snowden et al., 2008). The fitted ellipses have the semi-major axis lengths a_2/r_{200}=0.1, 0.2, 0.3, 0.4, and Kawahara (2010) found the mean axis ratio q is roughly 0.8 with no significant radial dependence.

The mean $q \approx 0.8$ is larger than that of dark matter ($q \approx 0.6$) predicted by Oguri et al. (2003). This is fully expected because, under the conventional hydrostatic equilibrium:

$$\frac{1}{\rho_{\rm gas}}\nabla p = -\nabla \phi, \tag{3.17}$$

the gas density roughly follows *isopotential* surfaces that is in general more spherical than *isodensity* surfaces.

In order to compare the observation data with the simulation results of Jing & Suto (2002), Kawahara (2010) calculated the projected axis ratio of isopotential surfaces based on the PDF (3.12), as described in what follows.

For a self-similar density distribution $\rho(R_e)$, the gravitational potential $\phi(\boldsymbol{x})$ is given by

$$\phi(\boldsymbol{x}) = -\pi G \left(\frac{A_2 A_3}{A_1}\right) \int_0^\infty d\tau \frac{\psi(\infty) - \psi(R_e(\tau))}{\sqrt{(A_1^2 + \tau)(A_2^2 + \tau)(A_3^2 + \tau)}}, \tag{3.18}$$

where

$$\psi(R_e(\tau)) = \int_0^{R_e(\tau)} \rho(R) dR^2 \tag{3.19}$$

and

$$R_e^2(\tau) = A_3^2 \sum_{i=1}^3 \frac{x_i^2}{\tau + A_i^2}. \tag{3.20}$$

For the elliptical NFW profile:

$$\rho(R_e(\tau)) = \frac{\rho_0}{(R_e(\tau)/R_s)(1 + R_e(\tau)/R_s)^2}, \tag{3.21}$$

$\psi(R_e(\tau))$ is given by

$$\psi(R_e(\tau)) = \frac{2R_s \rho_0}{1 + R_s/R_e(\tau)}. \tag{3.22}$$

Then $\phi(\boldsymbol{x})$ is calculated through Equation (3.18). An isopotential surface of the resulting $\phi(\boldsymbol{x})$ is, strictly speaking, not an ellipsoid, but can be approximated by an ellipsoid with the minor-to-major axis ratio μ_{13} and the intermediate-to-major axis ratio μ_{23} are given by

$$\mu_{13} = \frac{x_1^*}{x_3^*} \quad ; \quad \mu_{23} = \frac{x_2^*}{x_3^*}, \tag{3.23}$$

where x_i^* $(i = 1, 2, 3)$ satisfy

$$\phi(x_1^*, 0, 0) = \phi(0, x_2^*, 0) = \phi(0, 0, x_3^*) = \text{const.} \tag{3.24}$$

Finally the *projected* axis ratio q of the isopotential surfaces is calculated through Equation (3.16).

Figure 3.4 is a reproduction of the result of Kawahara (2010). The blue symbols show the observation data, and the black curve illustrates the PDF of axis ratio of isopotential surfaces predicted from the PDF of JS02. While the uncertainty is large, similarly to the case of the weak lensing analysis by Oguri et al. (2010), Kawahara (2010) concluded the observation data is roughly consistent with the PDFs of Jing & Suto (2002).
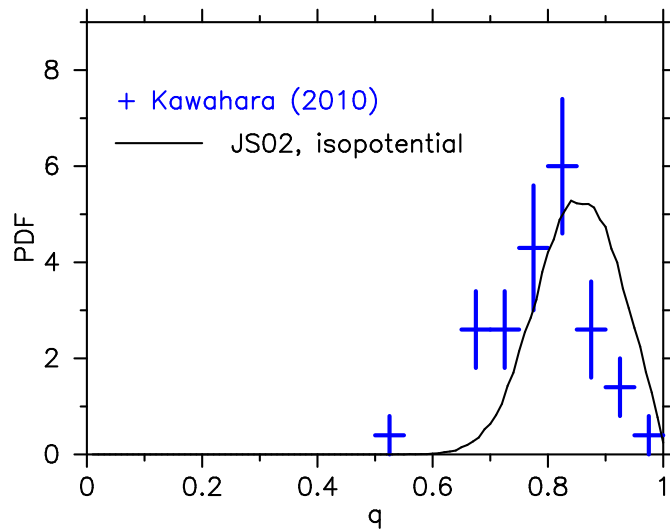
Figure 3.4: Comparison of the PDFs of axis ratio between the X-ray surface brightness of actual clusters by Kawahara (2010) and the isopotential surfaces estimated from the PDF of JS02.

It is important to note that both Oguri et al. (2010) and Kawahara (2010) prepared the PDF of projected axis ratio based on the PDF (3.12) to compare with the observation data. The simulation results of Jing & Suto (2002) are, however, based on the self-similarity assumption for dark matter density distribution. Since Jing & Suto (2002) showed that the density distribution is not necessarily self-similar, the true projected axis ratio can be different from that predicted under the self-similarity assumption. In addition, for X-ray observations, the hydrostatic equilibrium assumption is not necessarily valid due to the dynamical motion of intracluter gas(Lau et al., 2009, 2013; Fang et al., 2009; Suto et al., 2013).

Therefore more reliable prediction for PDFs of projected axis ratio (of dark matter or X-ray surface brightness) will be obtained by directly measuring projected axis ratio from cosmological simulation data. This is exactly what we are aiming at this thesis.

In Chapter 5, we point out that the self-similarity assumption adopted by Jing & Suto (2002) is not necessarily valid, and directly calculate the PDF of projected axis ratio of dark matter density distribution to compare with the observation data by Oguri et al. (2010). Subsequently, in Chapter 6, we calculate the PDF of axis ratio of X-ray surface brightness by using cosmological hydrodynamical simulations, and compare the results with the observation data by Kawahara (2010).

Chapter 4

Confrontation of Top-Hat Spherical Collapse against Dark Halos from Cosmological N-Body Simulation

4.1 Motivation

As presented in Section 3.4, Rossi et al. (2011) found the discrepancy in the probability distribution function (PDF) of axis ratio between the simulation results by Jing & Suto (2002) and the theoretical prediction from the ellipsoidal collapse (EC) with the Gaussian random initial conditions; more massive simulated halos are less spherical, but more massive halos are less spherical in theory.

The above discrepancy indicates that EC does not necessarily reproduce the evolution of simulated halos. As seen in Section 3.2, EC includes a variety of strong assumptions; homogeneous density, neglect of velocity dispersion, instantaneous and separate virialization of three axes, etc. In Chapter 5, we examine how and when these assumptions become invalid by comparing the evolution of individual simulated halos with the prediction of EC.

Before doing so, we suspect that even the top-hat spherical collapse (TSC) also does not necessarily reproduce the evolution of simulated halos, since TSC adopts the strong assumptions including homogeneous density, neglect of velocity dispersion and instantaneous virialization.

TSC is widely used in *statistical contexts*; e.g., it is applied to the halo identification in simulations, and the mass measurements and scaling relations of galaxy clusters, etc. Nevertheless, the validity of TSC for the evolution of *individual* halos has never been tested. In this chapter, we compare the TSC prediction with the evolution of halos extracted from the N-body simulation, *on the object-wise basis*, and clarify how and when the strong assumptions in TSC become invalid for the simulated halos.

In Section 4.2, we describe the N-body simulation we use and how to trace back the simulated halos identified at present to the past. We there show the velocity dispersion of dark matter plays an important role, and investigate its evolution in the phase space. The evolution of the simulated halos is compared with TSC in Section 4.3. In Section 4.4, the main part of this chapter, we examine how the velocity dispersion affects the virialization

process of halos. Finally, Section 4.4 summarizes this chapter.

4.2 Halos from cosmological N-body simulation

4.2.1 Numerical simulation and halo catalog

We use a cosmological N-body simulation performed with the TreePM code `Gadget-2` (Springel, 2005). The simulation is run from $z = 99$ to $z = 0$ in a periodic box of $360\,h^{-1}$Mpc (comoving) on a side, and the number of dark matter particles is 1024^3 and the mass of each particle is $m_p = 3.4 \times 10^9 h^{-1} M_\odot$. The initial condition is generated by `MUSIC` code (Hahn & Abel, 2011), which employs second order Lagrangian perturbation theory. The transfer function at the initial redshift $z_{\rm ini} = 99$ is generated by the linear Boltzmann code `CAMB` (Lewis et al., 2000). The adopted cosmological parameters are consistent with the *Wilkinson Microwave Anisotropy probe* (WMAP) 9 year result (Hinshaw et al., 2013): $(\Omega_{\rm m,0}, \Omega_{\Lambda,0}, h, n_s, \sigma_8)$=(0.279, 0.721, 0.7, 0.972, 0.821). The gravitational softening length is fixed at $20\,h^{-1}$kpc comoving.

To identify halos in our simulation, the friends-of-friends (FOF) algorithm (Davis et al., 1985) is performed with the linking parameter $b = 0.159$, corresponding to the virial density $\Delta_{\rm vir} = 355.4$. Some authors (More et al., 2011; Courtin et al., 2011) have pointed out that the overdensity within a FOF halo varies with its mass even for the same linking parameter b. In our study, however, this issue would not be important since the mass range of the simulated halos is relatively narrow and a "halo" is redefined using the spherical overdensity.

We obtain 17535 halos with mass $> 10^{13} h^{-1} M_\odot$ at $z = 0$, and we choose to analyze 100 most massive halos with mass range $2.06 < M/(10^{14} h^{-1} M_\odot) < 16.6$ in order to have a good mass resolution for each halo. In particular, Figures 4.1 - 4.4 below utilize six halos listed in Table 4.1 for illustration.

Name	M	$\delta_{\rm ini}$	$z_{\rm ta}$
	$[10^{14} h^{-1} M_\odot]$	$[10^{-2}]$	
Halo I	16.6	2.72	1.12
Halo II	16.3	2.61	1.21
Halo III	8.38	2.86	0.870
Halo IV	4.87	2.36	0.891
Halo V	4.13	2.79	1.04
Halo VI	2.65	3.06	1.28

Table 4.1: Six halos selected for Figures 4.1 - 4.4 below. The turn-around redshift is estimated from the maximum point of the cubic-spline interpolated radius $R(z)$ of the simulated halo from the fifteen redshift data (see text in Section 4.2.2).

4.2.2 How to trace back the evolution of simulated halos

Using the above simulation data, we compare the evolution of each halo with TSC. To this end, we define a sphere that corresponds to a halo identified by the FOF algorithm at $z = 0$ as follows. First we calculate the center-of-mass of the FOF member particles of a halo. Starting from the center-of-mass, we find the radius within which the overdensity becomes $\Delta_{\mathrm{vir}} = 355.4$. Then we calculate the center-of-mass of all the particles in the sphere (not necessarily the FOF member particles), and repeat the procedure again. This process is iterated until the center-of-mass position of the particles in the sphere matches to the center of the sphere within $1\ h^{-1}$ kpc in comoving coordinates. After the iteration converges, we denote the mass and radius of the sphere by M_{355} and $R_M(z = 0)$, respectively, for that halo.

For the purpose of our current study, we need the protohalos at different redshifts, which correspond to the halos identified at $z = 0$ according to the above procedure. We have stored fifteen simulation snapshots; $z_i = 99$ (initial), 49, 9, 5, 4, 3, 2, 1.5, 1, 0.8, 0.6, 0.4, 0.2, 0.1 and 0. We use them to trace back the evolution of halos identified at $z = 0$. For each redshift $z = z_i(\neq 0)$, we trace the distribution of the FOF member particles back to z_i, and calculate the center-of-mass of the distribution at z_i. From the center-of-mass, we find the radius inside which the mass is equal to M_{355} computed from each halo at $z = 0$. The iteration process described above is carried out to determine the center of the sphere. Finally, we define $R_M(z_i)$ as the radius of the sphere. Note that the mass M_{355} is constant while $R_M(z_i)$ is a function of redshift.

The left panels of Figure 4.1 plot all the particles within the thickness of $0.03\ R_M(z)$ at each redshift around its center of mass. In order to clarify the degree of mixing of the particles, they are plotted in different colors according to their initial positions (at $z = 99$). By $z = 9$, the particles are little mixed, and the particles with the same color roughly keep the shape of the spherical shell. By $z = 3$, however, filament-like structures already started to emerge, indicating that the uniform density assumption begins to break.

The colors of the particles at z=1, 0.4 and 0 are defined according to their positions at $z = 1$. The redshift $z = 1$ approximately corresponds to the turn-around epoch of Halo I. The colors are violently mixed by $z = 0.4$ (after about 3.5 Gyr), in contrast to the period from the initial time to $z = 2$ (about 3.3 Gyr). This is because the relaxation has finished in the inner part of the halo, and particles in the relaxed region are stirred due to shell-crossing.

4.2.3 Evolution of velocity dispersion in phase space

In order to see the degree of particle-mixing more clearly, we consider the phase space as well. Note that, throughout this chapter, we refer to the space of radial coordinate and radial velocity (r, v_r) as the "phase space", for the comparison with the spherical model (e.g., Colombi et al., 2015; Sousbie & Colombi, 2015). The right panels of Figure 4.1 demonstrate the phase space distribution of particles colored in the same way as the left panels. The right panels plot a randomly selected one percent of the particles inside the sphere within the shown radial range while the left panels plot all the particles in the slice region.
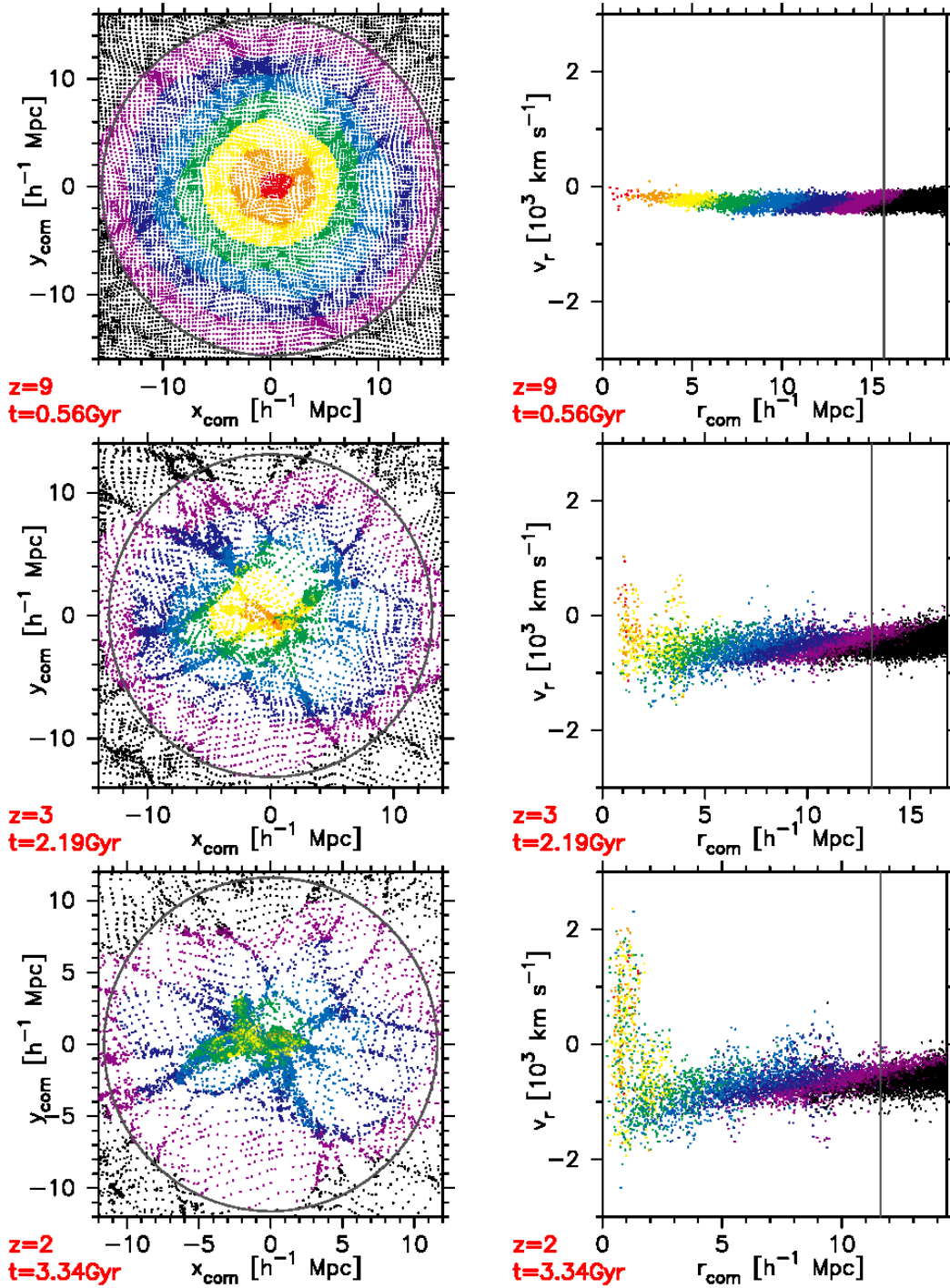
Figure 4.1: The particle distribution of Halo I in the comoving space (left) and the phase space (right). We select a slice of thickness 3 % of $R_M(z)$ at each redshift, and plot all the particles within the slice in the lect panel. In contrast, we consider a large sphere that encloses the protohalo defined at each halo and plot randomly selected 1 % of the particles in the sphere. The gray circles in the left panels and the vertical lines in the right panels indicate $R_M(z)$. (The caption continues to the next page.)
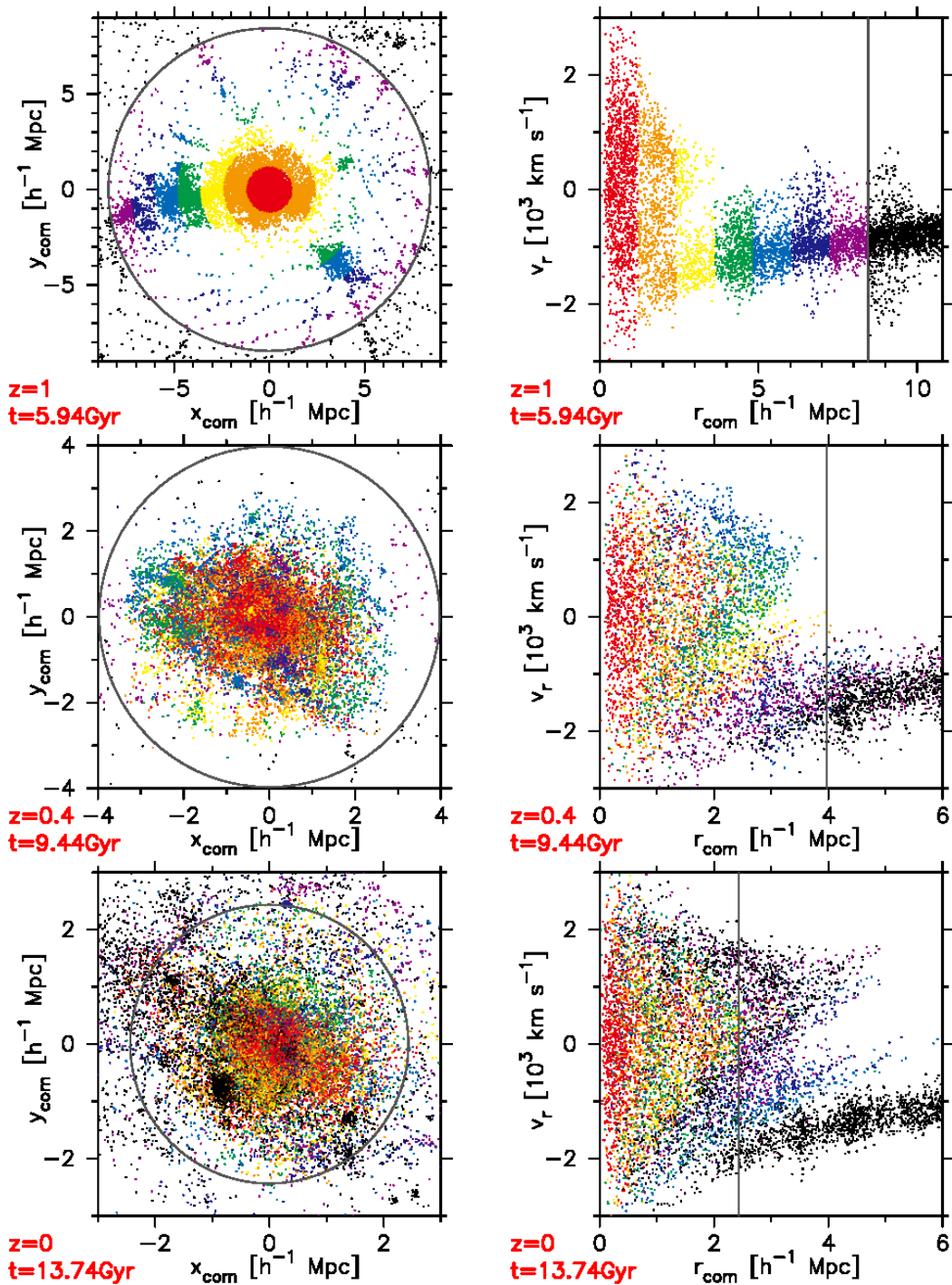
Figure 4.1: (Continued.) The particles are color-coded according to the initial position at $z = 99$; the sphere of radius $R_M(z = 99)$ is divided into seven equal radial shells, and particles in each bin are plotted in different colors. Black points correspond to particles outside the initial halo at $z = 99$. Those different color particles become mixed due to the subsequent evolution. In order to clarify the later evolution visually. we redefine the colors of the particles at $z = 1$ (approximately the turn-around epoch), and keep the color convention until $z = 0$.

45

By definition, the initial particle distribution looks like seven color bars. These bars become gradually tilted by $z \sim 2$. Although the coordinate space distribution has exhibited clear non-sphericity by $z = 3$, the phase space distribution looks still well ordered. The innermost particles, however, have fallen into the center and then have positive (outward) radial velocity. By $z = 2$, the region with large velocity dispersion σ_r^2 has formed. The region gradually expands outward, and finally reaches outside the halo radius $R_M(z = 0)$. This is one of the most remarkable differences between the simulation and the description of TSC.

To look into the region with large σ_r^2 more carefully, we fully exploit all the particles and visualize the phase space density in Figure 4.2; $z = 1$ (top), $z = 0.4$ (middle), $z = 1$ (bottom). The figure clearly shows the high density region around the outer end of the large σ_r^2 region, indicating the stream of the particles that have (more than) once fallen into the center. Such a motion of particles creates the large σ_r^2 region expanding outward.

It is informative to consider here the prediction of the self-similar model for the EdS universe (see Section 2.3; Fillmore & Goldreich, 1984; Bertschinger, 1985). In the self-similar model, a spherical shell falls toward the center, and moves outward again after shell-crossing. The shell turns-around at some radius and falls back toward the center. Such oscillations of a number of shells account for the development of the velocity dispersion in a halo. The physical size of the halo increases with time as more shells infall with larger turn-around radius.

The above picture explains, at least qualitatively, the evolution of σ_r^2 of Halo I shown in Figure 4.2. From $z = 1$ to $z = 0$, the velocity dispersion develops from the center of the halo. The profile of σ_r^2 exhibits a sharp drop-off at the radius corresponding to the end of the large velocity dispersion region. In contrast, the radial (peculiar) velocity v_r almost vanishes in the central region, while it is negative in the outer region, representing the falling particles. All these features are consistent with the self-similar model.

To visualize the consistency between the self-similar model and the simulation results, the the self-similar solution is overplotted on the phase space distribution at $z = 0$ (bottom left panel of Figure 4.2). The overall feature of the simulated halo is followed, at least qualitatively, by the self-similar solution. Especially, groups of the particles in course of the first and second turning-arounds are apparent in the phase space distribution.

Strictly speaking, however, the self similar model describes a *spherical* halo in the *EdS universe*, which naturally leads to the big difference between the simulation data and the overplotted self-similar solution. In addition to the "regular" development of σ_r^2 described in the self-similar model, the inhomogeneity contributes to the evolution of σ_r^2 in the simulated halos. For example, the infall and the subsequent turn-around of a substructure generates an additional velocity dispersion that is not described in the self-similar model. Such a process enhances individuality of halos, and makes it difficult to find universality (if any) of the evolution of σ_r^2, as will be discussed again in later sections.

Furthermore, the density profile of the self-similar solution is predicted to be asymptotically proportional to $r^{-9/4}$, which is inconsistent with the Navarro-Frenk-White (NFW) density profile (Navarro et al., 1995, 1996, 1997), the universal density profile common in observed and simulated halos. Therefore the self-similar solution is not fully reliable when we *quantitatively* investigate the evolution of velocity dispersion.

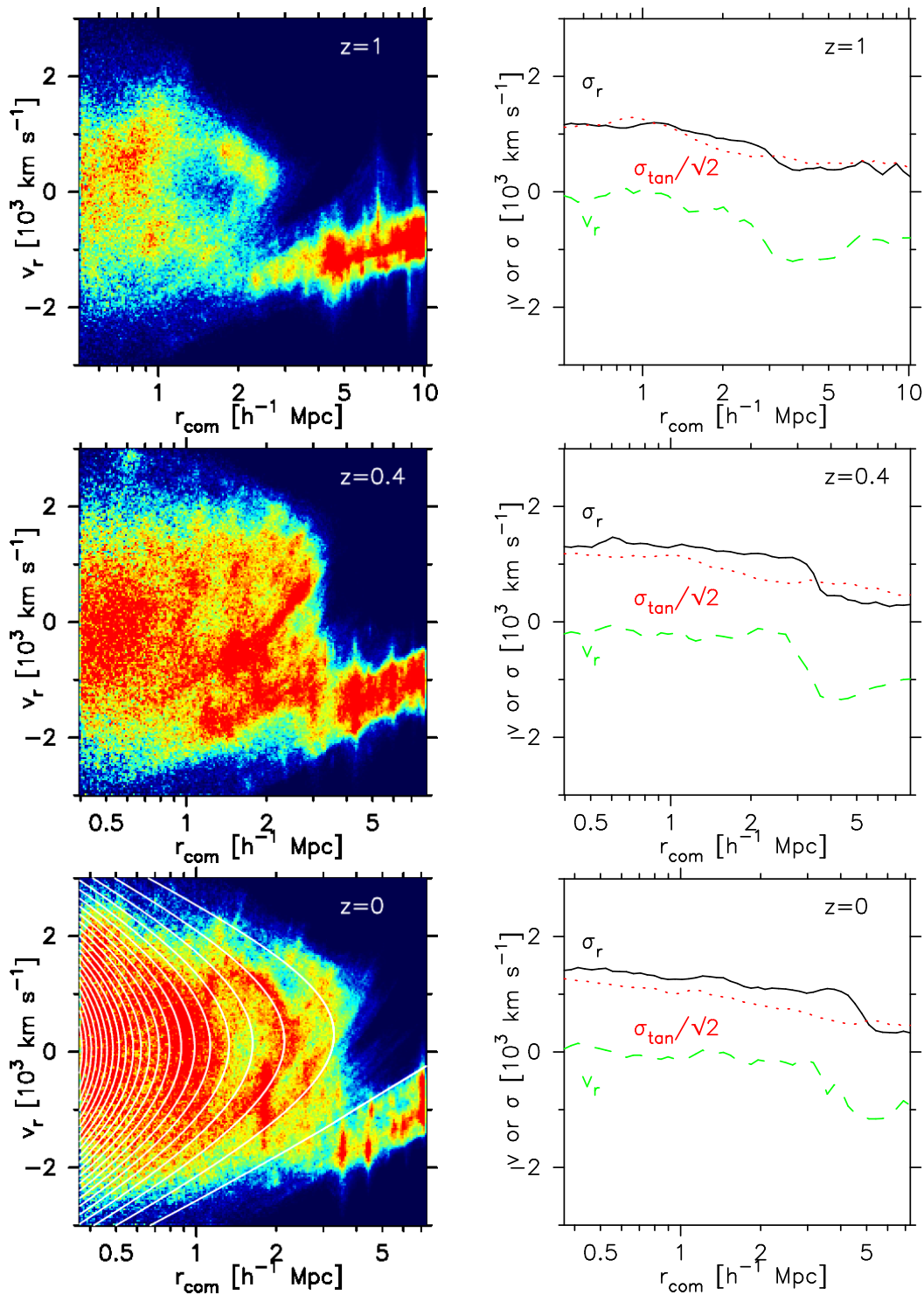Figure 4.2: Halo I's color contrast images of the phase space density (left) and the corresponding profiles (right) of radial velocity (green dashed), radial (black solid) and tangential (red dotted) velocity dispersions, for z =1 (top), 0.4 (middle) and 0 (bottom). For the contrast image for $z = 0$, the self-similar solution (Fillmore & Goldreich, 1984; Bertschinger, 1985) in the EdS universe is overplotted.

Adhikari et al. (2014) have also considered the region with large velocity dispersion in a different context. They refer to the radius where the density sharply drops as "splashback radius", which is essentially the same as the locus where the velocity dispersion sharply drops. They proposed the splashback radius as a more physically motivated definition of a dark halo, instead of the traditional definition by using some threshold overdensity. Although the splashback radius is often much beyond the X-ray observed region of galaxy clusters, More et al. (2015) have shown that the relation between the splashback and R_{200m}, within which the overdensity is 200 times the mean matter density, can be written as a function of the peak height inside R_{200m}. Furthermore, More et al. (2015) indicated that the splashback radius may be already observed as a caustic of line-of sight velocity of galaxies by Rines et al. (2013). Although Adhikari et al. (2014) claimed that it is difficult to unambiguously determine the splashback radius of individual halos, these studies indicate the importance of velocity dispersion in the halo evolution.

4.3 Comparison of Halo Radius Evolution Against TSC and Spherically Averaged Jeans Equation

We now compare the evolution of the sphere characterized by the radius $R_M(z)$ defined in Section 4.2.2, with the prediction of TSC. Figure 4.3 demonstrates the results for the six halos in Table 4.1. The TSC predictions (black solid line) are calculated from the initial overdensity of each halo. From the initial time until shortly before the turn-around epoch z_{ta}, $R_M(z)$ is very close to the model prediction, despite the fact that non-sphericity and non-uniformity develop by $z \sim 3$. From around z_{ta}, $R_M(z)$ deviates from the model prediction; the turn-around epoch is delayed, and thereafter the radius of the simulated halo becomes systematically larger than the model. Finally, the radius $R_M(z)$ does not collapse to zero (naturally), but settles into a finite radius. In addition, the present radius is also larger than the model prediction. Although the degree of the deviation from TSC varies from halo to halo, the above trend holds for majority of the simulated halos: the simulated halos turn around later, and have larger radii both at z_{ta} and $z = 0$ than those predicted by TSC.

We suspect that the difference between the simulation and TSC is mostly due to the velocity dispersion focused on in the previous section. In numerical simulations, the motion of dark matter particles should be described not by Equation (2.30), but by the (three-dimensional) Jeans equation. We here focus only on their radial motion to see the effect of the velocity dispersion in the framework of spherical symmetry. The spherically symmetric version of the Jeans equation is

$$\frac{Dv_r}{Dt} = -\frac{1}{\rho}\frac{\partial(\rho\sigma_r^2)}{\partial r} - \frac{2\sigma_r^2 - \sigma_{tan}^2}{r} - \frac{GM}{r^2}, \tag{4.1}$$

where D/Dt denotes the Lagrangian differentiation, and σ_{tan}^2 is the tangential velocity dispersion of dark matter. Note that σ_{tan}^2 includes dispersions in two directions (θ and φ directions in the spherical coordinates). The density and velocity dispersion usually decrease as a function of radius, so the first term is expected to delay the collapse epoch.
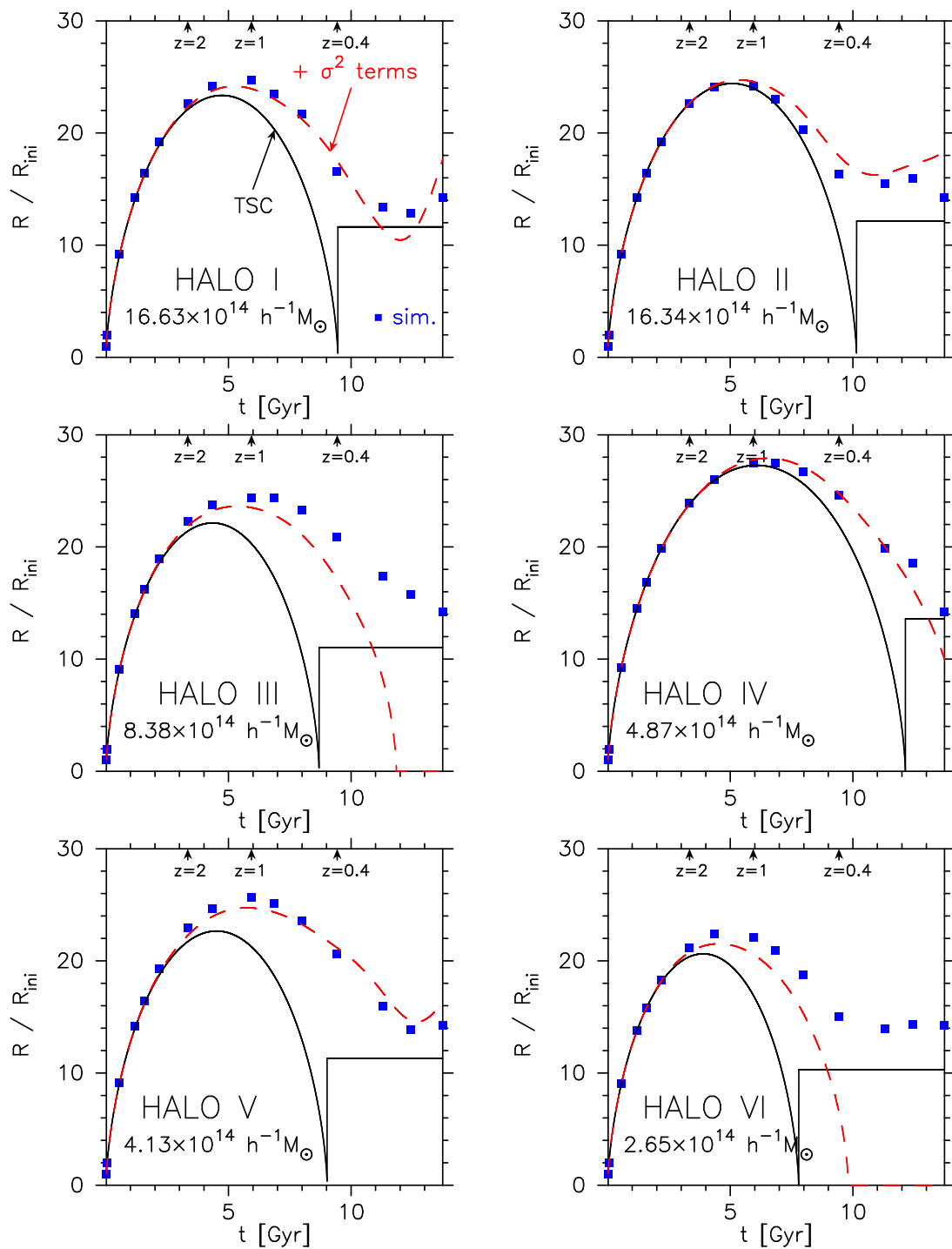
Figure 4.3: The comparison of the evolution of the halo radius predicted by TSC (solid) with the simulation (squares). The model prediction is calculated by using the initial condition of each simulated halos. The red dashed line shows the solution of the collapse model with the velocity dispersion terms included (see text), which improves the prediction for the evolution of the halo radius.

To confirm this, we evaluate the first two terms at $r = R_M(z)$ in the right-hand-side of Equation (4.1) from the simulation data for each of the fifteen redshifts, and solve the Equation (4.1) with the two terms replaced by using the cubic-spline interpolated values from the fifteen redshifts.

The results are illustrated by the dashed lines in Figure 4.3. The prediction based on Equation (4.1) reproduces the simulation results much better than that of TSC at least for Halos I, II, IV and V. Therefore, we confirm that velocity dispersion explains the delayed turn-around and the stopped contraction. For Halos III and VI, on the other hand, the modification is not so successful. This is probably attributed to the strong non-sphericity of the dark matter distribution. In fact, as shown in Figure 4.4, Halo III has undergone a drastic merger of two similar mass objects. Halo VI, on the other hand, does not undergo such a big merger, but its mass accretion occurs prominently along a single direction. In the other four halos, matter assembles around the central structure from every direction (The distribution of Halo I is shown in Figure 4.1).

Hence, the level of the improvement depends on the sphericity in the evolution of the halos. Also, the velocity dispersion terms in Equation (4.1) are not uniquely determined, so the details of the result depend on their evaluated values. Our present purpose, however, is not to precisely improve TSC, but to confirm the effect of velocity dispersion. Thus we conclude that the velocity dispersion plays an important role in the halo evolution from the above comparison.
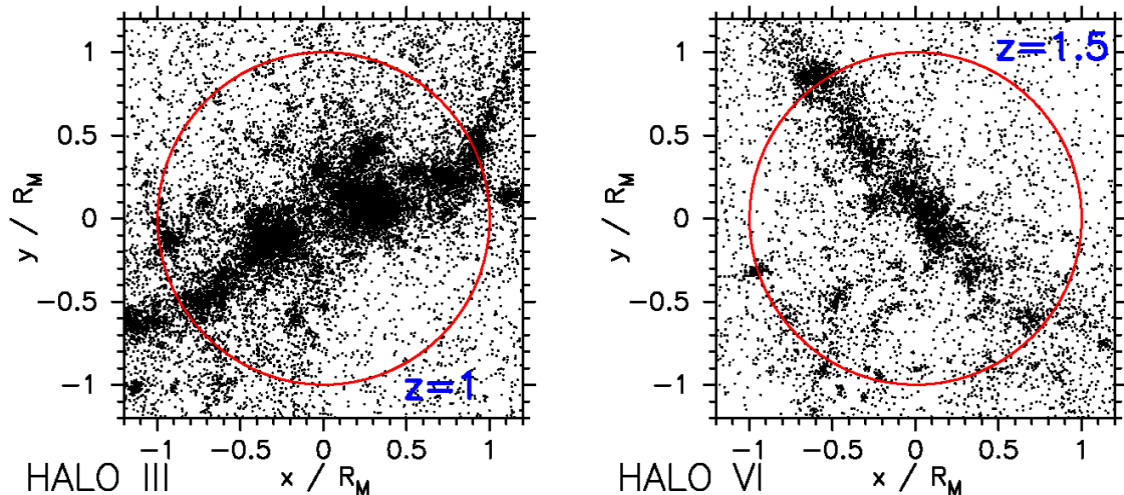
Figure 4.4: The particle distributions of Halo III at $z = 1$, and of Halo VI at $z = 1.5$, showing their highly non-spherical evolution. The plotted particles are a randomly selected 5 % of those in the box $1.2\,R_M(z)$ on a side, centered on the halo center.

If we can model the evolution of σ_r^2 of an individual halo fully from initial conditions, such a model helps us understand the halo evolution beyond the spherical collapse model. We have found, however, that the profiles of σ_r^2 and density vary sensitively from halo to halo: Although we made sure that σ_r^2 calculated from the linear power spectrum of the matter density fluctuations can approximate that of simulated halos at the early stage ($z \gtrsim 5$), the late evolution strongly depends on merger and mass accretion processes of

each halo. Also, as stated in Section 4.2, the evolution of σ_r^2 in the self-similar model is not quantitatively successful in describing that of the simulated halo. Thus the improved modelling, we do not attempt here, remains as an important future work.

As a preliminary step to the above challenge, therefore, we evaluate more quantitatively the deviation from TSC. In the next section, we do so by comparing the radii of the halos at the initial, the turn-around, and the present times.

4.4 Effect of Velocity Dispersion on Prediction for Present Radius

In this section, we focus on the difference in the present radius R_0 between the simulation and TSC prediction. We first compare R_0 and R_{ta} of the simulated halos. Next, we compare R_0 of the simulated halos with the predicted value by TSC from the initial conditions. To investigate the origin of the difference, it is essential to factorize the ratio into energy terms, and we here provide relevant definitions for preparation.

The ratio of radii at two epochs may be predicted from the conservation of the total energies E at those epochs. We decompose the total energy E into the kinetic energy K (due to both the Hubble expansion and the peculiar velocity), the gravitational potential energy W and the energy W^Λ due to the cosmological constant.

The potential energies W and W^Λ within the sphere of mass M and radius R are given by

$$W = -\gamma \frac{GM^2}{R} \tag{4.2}$$

and

$$W^\Lambda = -\gamma^\Lambda \Lambda M R^2, \tag{4.3}$$

respectively, where the parameters γ and γ^Λ depend on the density profile inside the halo (see, e.g., Equation 4.14 and discussion therein). Even if the particle distribution is non-spherical, the above parametrization is valid as long as a sphere of radius R is considered.

In order to derive a radial ratio at two epochs, the kinetic energy K must be associated with the other energy terms. In the settings of TSC, $K = 0$ at $z = z_{\mathrm{ta}}$, and $K = -(1 - 5\delta_{\mathrm{ini}}/3)W$ at $z = z_{\mathrm{ini}}$, In order to consider the difference from these predictions, we define the parameter α as

$$\alpha = -\frac{K}{W}. \tag{4.4}$$

Then the total energy E can be written as

$$\begin{aligned} E &= K + W + W^\Lambda \\ &= -(1-\alpha)\gamma \frac{GM^2}{R} - \gamma^\Lambda \Lambda M R^2, \end{aligned} \tag{4.5}$$

From now on, in order to represent the above quantities at different epochs, we use the subscript X to mean either of "ini", "ta", and "0", denoting the quantity at $z = z_{\mathrm{ini}}$, z_{ta} and 0 (present), respectively.

In the following sections, we use the ratio between the radii at $z = 0$ and another epoch, assuming that the virial theorem is applicable to the halos at $z = 0$. By equating the total energies E_X ($X =$ "ta" or "ini") and E_0, one obtains the ratio R_0/R_X in terms of those coefficients of the energies. Strictly speaking, R_0/R_X is a solution of the cubic equation, and the exact expression is not useful in understanding how each energy term contributes the difference between the simulation and TSC. The contribution of Λ is, however, very small compared to W:

$$\frac{W^\Lambda}{W} = \frac{6}{\Delta} \frac{\gamma^\Lambda}{\gamma} \frac{\Omega_\Lambda}{\Omega_m}, \tag{4.6}$$

which is, for example, less than 1 % at $z = 0$ ($\Delta = 355.4$ by definition for our adopted cosmology). Hence we can treat W^Λ/W as an infinitesimal.

Note, however, that, according to the virial theorem in the universe with Λ (Nowakowski et al., 2002), a virialized halo satisfies $-K/W = 1/2 - W^\Lambda/W = 0$ in the same settings as TSC, i.e., α'_0 includes an additional W^Λ/W. Hence we define another parameter α'_0 only for $z = 0$ as

$$\alpha'_0 = -\frac{K_0}{W_0} + \frac{W_0^\Lambda}{W_0}, \tag{4.7}$$

although the difference between α_0 and α'_0 is negligible at the level of the following discussion.

Then the total energy E_0 at $z = 0$ is $E_0 = (1 - \alpha'_0)W + 2W^\Lambda$. By equating E_0 and $E_X = (1 - \alpha_X)W_X + W_X^\Lambda$, we solve R_0/R_X perturbatively up to the leading term in W^Λ/W ($\propto \Lambda R^3/(GM)$). The result is

$$\frac{R_0}{R_X} = \frac{1 - \alpha'_0}{1 - \alpha_X} \frac{\gamma_0}{\gamma_X} \frac{1}{\beta_X^0}(1 - \epsilon_X^0), \tag{4.8}$$

where

$$\beta_X^0 = \frac{E_0}{E_X} \tag{4.9}$$

and

$$\epsilon_X^0 = \left[\frac{\gamma_X^\Lambda}{\gamma_X(1 - \alpha_X)} - \frac{2\gamma_0^\Lambda}{\gamma_0(1 - \alpha'_0)}\left(\frac{\gamma_0(1 - \alpha'_0)}{\gamma_X(1 - \alpha_X)\beta_X^0}\right)^3\right]\frac{\Lambda R_X^3}{GM}. \tag{4.10}$$

A substantial fraction of the particles in a simulated halo defined in Section 4.2.2 indeed move into and out of the sphere between the two epochs, and the total energy within the sphere is not necessarily guaranteed to be conserved. The parameter β indicates the degree of the energy conservation.

We calculate the above parameters α, β and γ for the 100 simulated halos. For a simulated halo, the kinetic energy K is calculated as

$$K = \frac{1}{2}\sum_i m_i(\boldsymbol{v}_i + H\boldsymbol{x}_i)^2, \tag{4.11}$$

where m_i, $\boldsymbol{x}_i$ and $\boldsymbol{v}_i$ are mass, position and peculiar velocity of the i-th particle, and H is the Hubble parameter at the epoch. The summation is taken over all the particles within the sphere of radius R.

The gravitational potential energy W is calculated as

$$W = -G \sum_{i<j} \frac{m_i m_j}{|\boldsymbol{x}_i - \boldsymbol{x}_j|}, \tag{4.12}$$

where the summation is taken over all the combinations of the i-th and j-th particles within the sphere of radius R. The parameter γ is simply computed by $\gamma = W/(GM^2/R)$.

4.4.1 Comparison of R_0 and R_{ta}

The TSC prediction (2.37) is based on the energy conservation between the turn-around and the collapse epochs. As seen in Section 4.3, however, it is difficult to define unambiguously its collapse time. So, we first compare the *present* radius R_0 with the turn-around radius R_{ta} instead. If TSC is exact, R_0 defined with $\Delta_{\mathrm{vir}} = 355.4$ should correspond to R_{vir} for objects that collapsed at $z = 0$. Note that, both R_0 and R_{ta} in this section are of the simulated halos.

The ratio R_0/R_{ta} predicted by TSC is 0.483, which can be compared with the simulation. The top-left panel of Figure 4.5 shows that the R_0/R_{ta} of the simulated halos is 0.56 on average, with roughly 10 - 20 percent scatter. This level of the deviation may be fully expected, given the extremely simplified assumptions of TSC.

In order to identify the origin of the discrepancy more quantitatively, we use Equation (4.8). In TSC, $\epsilon_{\mathrm{ta}}^0 = 0.032$, which explains the difference between the values of R_0/R_{ta} between the EdS universe ($R_0/R_{\mathrm{ta}} = 0.5$) and the universe with Λ ($R_0/R_{\mathrm{ta}} = 0.483$). For simplicity, we do not consider the contribution of each parameter in ϵ_X^Y to R_0/R_{ta}, and use the following:

$$\frac{R_0}{R_{\mathrm{ta}}} = 0.483 \frac{1 - \alpha_0'}{0.5} \frac{1}{1 - \alpha_{\mathrm{ta}}} \frac{\gamma_0}{\gamma_{\mathrm{ta}}} \frac{1}{\beta_{\mathrm{ta}}^0}. \tag{4.13}$$

Note that the contribution of Λ is partly incorporated in β_{ta}^0. TSC predicts that the kinetic energy vanishes at z_{ta} ($\alpha_{\mathrm{ta}} = 0$), and the virial theorem states that $\alpha_0' = 1/2$. In addition, the density profile is always uniform ($\gamma_{\mathrm{ta}} = \gamma_0 = 3/5$). Thus, combined with energy conservation ($\beta_{\mathrm{ta}}^0 = 1$), one obtains $R_0/R_{\mathrm{ta}} = 0.483$.

The number of our available snapshots of the simulation is limited, so we define the energy terms of each halo at z_{ta} as follows. First, for a simulated halo, the values of radius at fifteen redshifts are cubic-spline interpolated, and its maximum value and the corresponding epoch are defined as R_{ta} and t_{ta}, respectively. We calculate the energy terms for the two snapshots bracketing t_{ta}, and define the energy at t_{ta} with the linear-interpolation.

Let us consider β_{ta}^0 first. The top-right panel of Figure 4.5 shows the calculated β_{ta}^0 for 100 halos. The average $\langle \beta_{\mathrm{ta}}^0 \rangle$ is 0.96, so the total energy is conserved to a good approximation. This is not trivial, since a significant fraction ($\sim 20\%$) of the particles in the sphere is changed. While we take into account the factor, β_{ta}^0 does not play a major role in Equation (4.13).
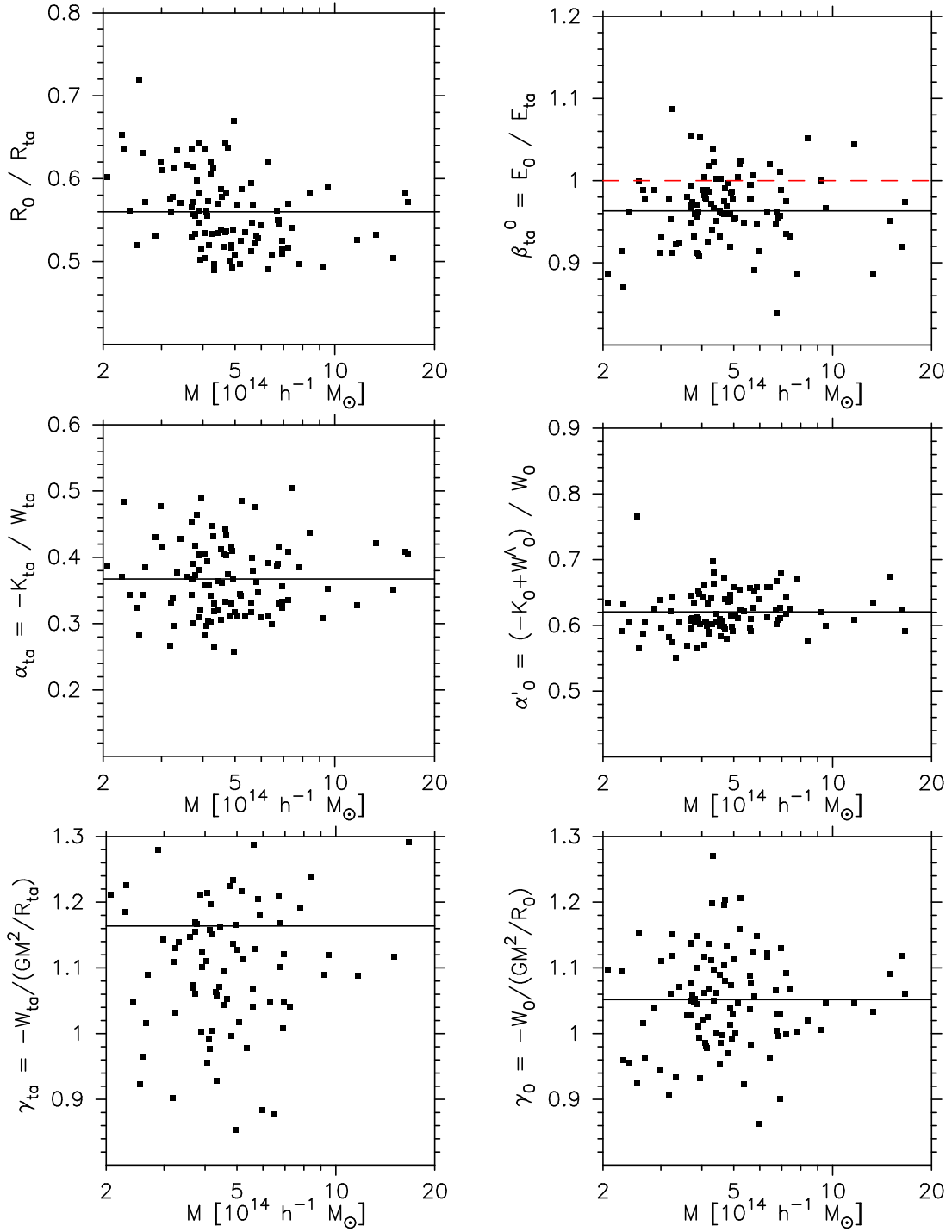
Figure 4.5: Comparison of the turn-around radius with the present radius of the 100 simulated halos (top-left). Their difference can be attributed to the parameters α_{ta} (middle-left), α'_0 (middle-right), γ_{ta} (bottom-left) and γ_0 (bottom-right). The energy conservation is also checked in terms of β^0_{ta} (top-right). The solid line in each panel indicates the average value. The red dashed line in the top-right panel shows unity , meaning the total energy in the sphere is conserved between the two epochs.

The middle panels in Figure 4.5 plot α_{ta} and α_0'. While TSC states that $\alpha_{\mathrm{ta}} = 0$, the simulated halos have roughly $\alpha_{\mathrm{ta}} = 0.37$ on average. This is the largest deviation from TSC, and can be attributed to the velocity dispersion in the central region of halos; at the turn-around, the halo expansion velocity of the outer shell almost vanishes, but the velocity dispersion of the inner region significantly contributes to the kinetic energy.

At the present time, α_0' is 0.62 on average, which is larger than $1/2$ predicted by the virial theorem. This result can be understood according to Łokas & Mamon (2001), who study the virialized state of a spherical halo with the NFW density profile. They defined the virialized state as a solution of the spherical Jeans equation, and derived the ratio K/W as a function of radius with the concentration parameter, c, and parametrized velocity-anisotropy. Since this model is for the equilibrium state, the halo has no average velocity, but finite velocity dispersion, which yields the substantial kinetic energy. For any concentration parameter and velocity-anisotropy, they find that K/W is larger than $1/2$ at any radius, and increases toward the center. This is mainly due to the density and velocity dispersion inside the sphere, and the matter surrounding the halo is not important. In most cases, K/W at the virial radius is in the range from 0.5 to 1, which is in qualitative agreement with our simulated halos. The difference in α_0' between the simulation and TSC is also attributed to the velocity dispersion that is naturally expected in the inside-out collapse model in the CDM universe.

Next, we look at γ_{ta} and γ_0, which are shown in the bottom panels in Figure 4.5. Both are distributed around unity, which is different from $3/5$ for the uniform density profile. As stated before, γ depends on the density profile inside the sphere. For example, the single power-law density profile $\rho \propto r^{-p}$ $(p < 5/2)$ results in $\gamma = (3-p)/(5-2p)$. Hence $\gamma = 1$ implies $p = 2$.

For the NFW profile with the concentration parameter c, we obtain

$$\gamma = c \left[\frac{c(2+c)}{2(1+c)^2} - \frac{\log(1+c)}{1+c} \right] \left[\log(1+c) - \frac{c}{1+c} \right]^{-2} \tag{4.14}$$

at the virial radius. Figure 4.6 plots Equation (4.14), showing that γ is a increasing function of c and $\gamma(c = 0) = 2/3$. Hence, for any c, the NFW profile predicts larger values of γ than $3/5$ from the uniform profile. According to Oguri et al. (2012), halos with the mass range $2. < M/(10^{14}h^{-1}M_\odot) < 20$ (our sample) typically have $3 < c < 10$, implying $0.9 < \gamma < 1.3$. The range agrees well with our γ_0. At z_{ta}, the density profile of the halo is not necessarily described by the NFW profile, so the above discussion can not be applied. The difference between γ_{ta} and γ_0 is small, so they do not play a major role. Also, as long as R_0/R_{ta} is concerned, the deviation of γ from $3/5$ itself is not important, but difference at the two epochs contributes the budget.

In summary, the ratio $R_0/R_{\mathrm{ta}} = 0.48$ in TSC is increased by $(1 - \alpha_{\mathrm{ta}})^{-1} = 1.6$ (not 1), and decreased by $(1 - \alpha_0')/0.5 = 0.76$ relative to the TSC prediction, which finally yields $R_0/R_{\mathrm{ta}} = 0.58$, approximately explaining the mean value of $R_0/R_{\mathrm{ta}} = 0.56$. This implies that, although the non-zero velocity dispersion effect is fairly large, the other effects tend to cancel it in practice.
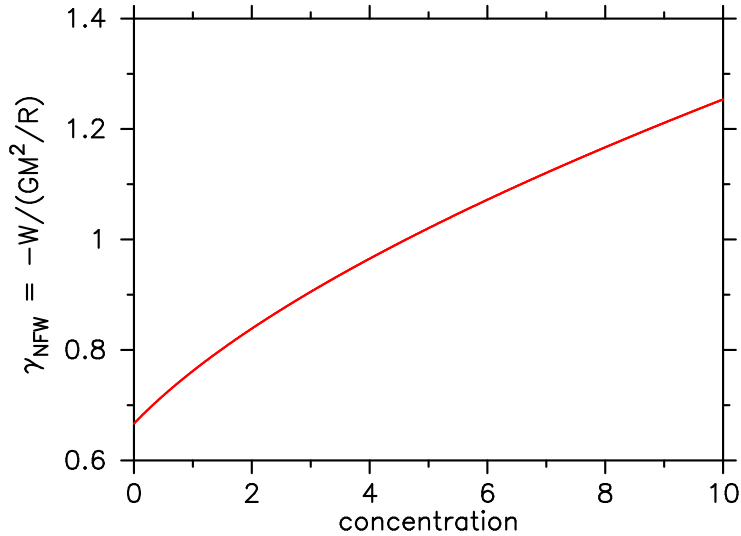
Figure 4.6: The parameter γ, defined by $W = -\gamma GM^2/R$, for the NFW density profile at the virial radius as a function of the concentration parameter.

4.4.2 Comparison of R_0 and $R_{\rm ini}$

An important advantage of TSC is its definite prediction for evolution of a halo *from the initial condition* and also the insensitivity of the result to M. Hence, we now compare the TSC prediction of the halo radius $R_{0,\rm TSC}$ at $z = 0$ from the initial condition ($z = 99$) measured for the simulation, against the radius $R_{0,\rm sim}$ measured for simulated halos $z = 0$. From now, we distinguish the two by denoting "TSC" or "sim".

The upper-left panel of Figure 4.7 plots the ratio $R_{0,\rm sim}/R_{0,\rm TSC}$ for the 100 simulated halos. For most halos, $R_{0,\rm sim}/R_{0,\rm TSC}$ is greater than unity. We suspect that the velocity dispersion produces this trend, and investigate its effect in the following.

We again use the spherical collapse model to describe $R_{0,\rm TSC}$ for simplicity. In the linear regime ($\theta \ll 1$), $R \approx R_{\rm ta}\theta^2/4$ and $\delta \approx 3\theta^2/20$ (cf. Equation (2.39)). Combined with $R_0 = R_{\rm ta}/2$, the model prediction for the present radius is given by

$$R_{0,\rm TSC} = \frac{3}{10}\delta_{\rm ini}^{-1}R_{\rm ini}. \tag{4.15}$$

(Here we have derived the above expression based on TSC in the EdS universe, but it holds in the flat universe up to the first order of W^Λ/W.) Using the ratio $R_{0,\rm sim}/R_{\rm ini}$ that can be written in the form of Equation (4.8); we obtain

$$\begin{aligned}
\frac{R_{0,\rm sim}}{R_{0,\rm TSC}} &= \frac{10}{3}\delta_{\rm ini}\frac{R_{0,\rm sim}}{R_{\rm ini}} \\
&= \frac{10}{3}\delta_{\rm ini}\frac{1-\alpha_0'}{1-\alpha_{\rm ini}}\frac{\gamma_0}{\gamma_{\rm ini}}\frac{1}{\beta_{\rm ini}^0},
\end{aligned} \tag{4.16}$$

where $\alpha_{\rm ini}$, $\beta_{\rm ini}^0$ and $\gamma_{\rm ini}$ are defined at $z = z_{\rm ini}$ as we did at $z = z_{\rm ta}$ (Section 5.1). Since $R_{\rm ini}$ is very small, we neglect the correction due to $\epsilon_{\rm ini}^0$.

We calculate α_{ini}, β_{ini}^0 and γ_{ini} from the simulation data. We again begin with looking at the energy conservation. We find that the particles within a halo change by about 30 % from $z = z_{\mathrm{ini}}$ to $z = 0$. As a result, the upper-right panel of Figure 4.7 shows that the total energy within the sphere changes within by ~ 7 % from $z = z_{\mathrm{ini}}$ to $z = 0$
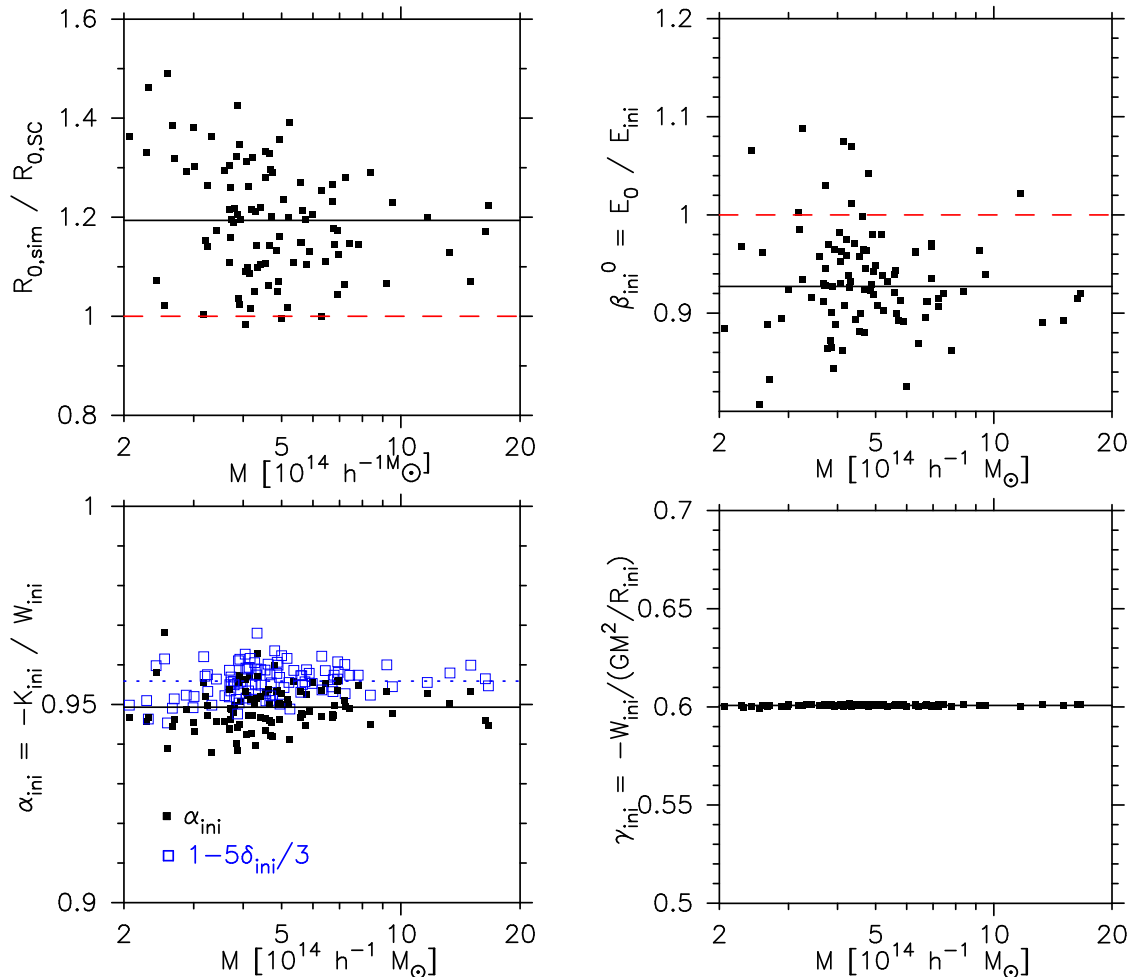
Figure 4.7: Comparison of the prediction of TSC with the present radius of the simulated halos (upper-left). Their difference is attributed to α_{ini} (lower-left), β_{ini}^0 (upper-right) and γ_{ini} (lower-right), and α_0' and γ_0 in Figure 4.5 (see text for the definition of the parameters). The solid line in each panel indicates the average value. The parameter α_{ini} is compared with the theoretical prediction $1-5\delta_{\mathrm{ini}}/3$ (blue open squares), and its average value is shown by the blue dotted line. The red dashed lines in the upper panels show unity for comparison; if TSC prediction is perfect, the radios of the radii and total energies become unity.

At the initial time, the density is almost uniform, so $\gamma_{\mathrm{ini}} = 3/5$, and $\alpha_{\mathrm{ini}} = 1 - 5\delta_{\mathrm{ini}}/3$ for small δ. Actually, the simulated halos have the values of γ_{ini} and α_{ini} very close to the theoretical values, as shown in the lower panels of Figure 4.7. Thus Equation (4.16)

practically reduces to

$$\frac{R_{0,\text{sim}}}{R_{0,\text{TSC}}} = \frac{1 - \alpha'_0}{0.5} \frac{\gamma_0}{0.6}, \tag{4.17}$$

which indicates that the deviation of $R_{0,\text{sim}}/R_{0,\text{TSC}}$ from unity is largely dictated by α'_0 and γ_0. If $\alpha'_0 = 1/2$ and $\gamma_0 = 3/5$, $R_{0,\text{sim}}/R_{0,\text{TSC}} = 1$. In reality, however, $(1 - \alpha'_0)/0.5 = 0.76$ reduces $R_{0,\text{sim}}/R_{0,\text{TSC}}$, and $\gamma_0/0.6 = 1.6$ increases $R_{0,\text{sim}}/R_{0,\text{TSC}}$ to 1.3, which approximates the average $\langle R_{0,\text{sim}}/R_{0,\text{TSC}} \rangle = 1.2$. Therefore, the deviation $R_{0,\text{sim}}/R_{0,\text{TSC}}$ is mainly attributed to the non-uniformity of the *present* density profile and the *present* kinetic energy due to the velocity dispersion.

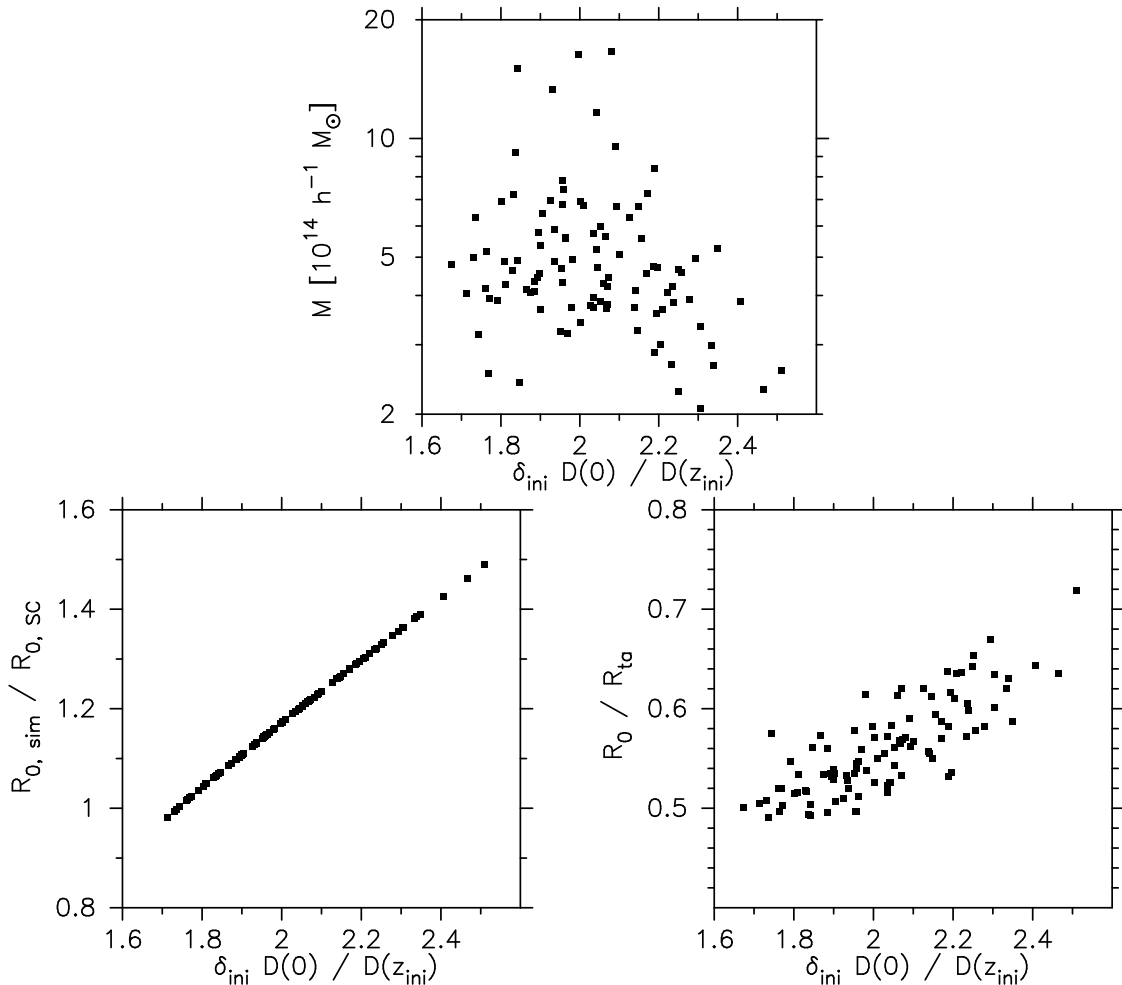Figure 4.8: The halo mass (upper) and the difference in the radial ratios between TSC and the simulation (lower), vs. the initial overdensity (normalized by the linear growth factor).

It is interesting to see how the above results depend on the initial overdensity δ_{ini} of the simulated halos since the TSC predictions are almost independent of the halo mass and mainly determined by δ_{ini}.

We have defined the spherical region for each halo based on the overdensity Δ_{vir}. The value of Δ_{vir} corresponds to a halo that is predicted to collapse exactly at $z = 0$ by TSC. Figure 4.3 shows, however, the simulated haloes collapse significantly earlier (although it is difficult to precisely determine when they collapse, since the radius does not shrink to zero). This implies that δ_{ini} of the simulated halos is larger than predicted by TSC.

In fact, the upper panel of Figure 4.8 shows that all the simulated halos have the initial overdensity (normalized by the linear growth factor) larger than the linearly extrapolated threshold of $\delta_{\mathrm{c}} = 1.67$ for a halo that is expected to collapse at present in TSC. In addition, there seems a weak trend that mass is anti-correlated to δ_{ini}; more massive halos have smaller δ_{ini}. Although the statistical significance is not strong, this is consistent with the initial density distribution of random-Gaussian field first derived by Doroshkevich (1970).

Because of the above correlation of mass and δ_{ini}, we attempt to replot $R_{0,\mathrm{sim}}/R_{0,\mathrm{TSC}}$ and R_0/R_{ta} now in terms of δ_{ini}. Here we recall that we have defined the sphere for each present halo based on the common Δ_{vir}. So, by definition, $R_{0,\mathrm{sim}}/R_{0,\mathrm{TSC}}$ is proportional to $((1 + \delta_{\mathrm{ini}})/\Delta_{\mathrm{vir}})^{1/3} \times \delta_{\mathrm{ini}}$ (cf. Equation (4.16)). In fact, the lower-left panel of Figure 4.8 shows that $R_{0,\mathrm{sim}}/R_{0,\mathrm{TSC}}$ follows a single curve as expected.

Similarly to $R_{0,\mathrm{sim}}/R_{0,\mathrm{TSC}}$, R_0/R_{ta} should follow a single curve if TSC were an exact description of the evolution of simulated halos. In reality, however, their relation has a relatively larger scatter around the mean relation as shown in the lower-right panel of Figure 4.8. This corresponds to the deviation from the TSC prediction at $z = z_{\mathrm{ta}}$. While the degree of the scatter may be related to the non-sphericity of each simulated halo, we were not able to identify a clear dependence of non-sphericity on δ_{ini}. We also confirmed that there is no clear dependence on δ_{ini} in the parameters such as α_{ta}, γ_{ta}, etc. A further study on non-sphericity of halos may need a precise non-spherical definition of the region of simulated halos, and a wider mass range of halos, which we plan to study and present elsewhere.

4.5   Short Summary

We summarize the results of the object-wise comparison between TSC and the simulation results as follows:

1. Even though the averaging and the dynamics do not commute, the overall predictions of TSC approximately describe the evolution of the simulated halos fairly well, in particular prior to their turn-around epochs. In reality, however, the non-uniformity/inhomogeneity of dark matter density profiles and the non-zero velocity dispersions, both of which are neglected in TSC, turn out to play an important dynamical role.

2. Unlike a simplified TSC picture of the instantaneous collapse, dense clumps inside a halo collapse first, and merge and fall into the central region. Thus a large velocity dispersion is developed from the center to outer parts. The region with the velocity dispersion expands outward, and finally reaches outside the "virialized" region predicted by TSC.

3. The velocity dispersion inside the halos strongly affects the size of the present *virial* radius of halos. At the turn-around epoch z_{ta}, the kinetic energy K amounts to 37 % of the gravitational potential energy W, which increases the ratio R_0/R_{ta} of the radii of the simulated halos at $z = 0$ and $z = z_{\mathrm{ta}}$ by ~ 58 %. The velocity dispersion also contributes to the kinetic energy, and K/W becomes 0.62 on average (larger than 0.5 in TSC), which decreases R_0/R_{ta} by 25 %. In total, R_0/R_{ta} is 0.56 on average, which is larger than the TSC prediction (≈ 0.483) by 16 %.

4. Moreover, the ratio $R_{0,\mathrm{sim}}/R_{0,\mathrm{TSC}}$ of the present radius of the simulated halos to the TSC prediction significantly deviates from unity; $R_{0,\mathrm{sim}}/R_{0,\mathrm{TSC}}$ is 1.2 on average. The deviation from the TSC prediction is explained on average by ~ 20 % decrease due to the non-zero velocity dispersion effect, and ~ 60 % increase due to the non-uniformity of dark matter density profile at $z = 0$. While the two effects tend to cancel each other, those two effects need to be properly taken into account in the dynamical description of evolution of actual individual halos in the CDM universe.

Chapter 5

Evolution and Statistics of Non-Sphericity of Dark Matter Halos from Cosmological N-Body Simulation

5.1 Motivation

In the previous chapter, we have seen that the spherical collapse model does not necessarily reproduce the evolution of *individual* simulated halos. Just like in the case of the spherical collapse model, how well the ellipsoidal collapse model (EC; Section 3.2) reproduces the evolution of *individual* halos has never been tested before. Given the results in the previous chapter, one can easily expect that the prediction of EC is not always valid, since EC also adopts the strong assumptions including the homogeneous density, neglect of velocity dispersion and the separate virialization of three axes, etc.

In fact, as described in Section 3.4, Rossi et al. (2011) pointed out the discrepancy in the mass dependence of the non-sphericity of halos, between simulations and theory; more massive simulated halos are less spherical, in contrary to the prediction of EC with the Gaussian random initial conditions. This finding implies that the EC prediction indeed does not necessarily reproduce the evolution of individual simulated halos.

In order to better understand the above discrepancy between simulations and theory, in this chapter, we compare the evolution of simulated halos with the EC prediction *on the object-wise basis*, and clarify how and when the simulation results deviate from the EC prediction. Especially, we examine how the difference between simulations and theory appears in probability distribution functions (PDFs) of the non-sphericity (axis ratio) of halos. Discussion on the PDFs of axis ratio of dark matter density distribution will be helpful in the next chapter, where we approach the main goal of this thesis; we compare the PDFs of axis ratio of X-ray surface brightness between simulations and the currently available X-ray data.

Section 5.2 describes the N-body simulation used in this chapter, and how to follow the evolution of our simulated halos. We compare the evolution of individual halos with EC in Section 5.3. Section 5.4 discusses the statistical evolution of halo non-sphericity.

There we also examine the difference between our simulation results and the prediction of JS02, in three-dimensional space. In Section 5.5, we compute PDFs of projected (two-dimensional) axis ratio are constructed, and the results are compared with the currently available weak lensing data by Oguri et al. (2010). Section 5.6 summarizes this chapter.

5.2 Triaxial Modelling of Simulated Halos

5.2.1 N-body simulation

We use cluster-scale halos identified from a different cosmological N-body simulation from the one used in Chapter 4; the adopted cosmological parameters are the same, but the initial conditions are different. The details of the simulation and the halo-finding procedures are described in this subsection.

The simulation is started at $z = 99$, where $N = 1024^3$ particles distributed in a periodic cube with a side length of 360 h^{-1}Mpc (comoving). Their initial conditions are generated with a parallel code developed by Nishimichi et al. (2009) and Valageas & Nishimichi (2011), which is based on the second-order Lagrangian perturbation theory (Scoccimarro, 1998; Crocce et al., 2006).

The simulation employs the matter transfer function computed by a linear Boltzmann solver `CAMB` (Lewis et al., 2000) for a flat ΛCDM cosmology with the nine-year WMAP parameters (Hinshaw et al., 2013); $\Omega_{m,0} = 0.279$, $h = 0.7$, $n_s = 0.972$, and $\sigma_8 = 0.821$ are the current matter density in units of the critical density, the Hubble constant in units of $100\,\mathrm{km\,s^{-1}Mpc^{-1}}$, the scalar spectral index, and the amplitude of the density fluctuation (linearly extrapolated to the present) smoothed with a top-hat filter of radius 8 h^{-1}Mpc, respectively. With the above parameters, mass of each simulation particle m_{particle} is $3.4 \times 10^9\,h^{-1}M_\odot$, which is sufficient to resolve massive halos ($\gtrsim 10^{14}h^{-1}M_\odot$) at $z = 0$.

The particle distribution is then evolved using a publicly available parallel cosmological N-body solver `Gadget2` (Springel, 2005). The long-range gravitational force is computed on 2048^3 mesh points based on the fast Fourier transform, while the tree algorithm with the softening length of $20\,h^{-1}$kpc is adopted on short range. Snapshots at redshifts $z = 49$, 9, 5, 4, 3, 2, 1.5, 1, 0.8, 0.6, 0.4, 0.2, 0.1 and 0 are stored. Halos at $z = 0$ are identified using the friends-of-friends (`FOF`) algorithm (Davis et al., 1985) with the linking length of 0.159 times the mean inter-particle separation in one dimension. This length is chosen so that the corresponding virial overdensity Δ_{vir} matches 355.4 in units of the cosmic mean density at $z = 0$, which is motivated by the spherical collapse model (Gunn & Gott, 1972; Gunn, 1977; Peebles, 1980). Indeed, we confirmed that the total mass of the linked particles M_{FOF} approximately corresponds to the virial mass M_{vir}. Furthermore, `SUBFIND` algorithm (Springel et al., 2001) implemented in Nishimichi & Oka (2014), is applied to each FOF halo to identify substructures as well as unbound particles.

In this chapter, we use the FOF halos with $M_{\mathrm{FOF}} > 6.25 \times 10^{13}h^{-1}M_\odot$, corresponding to the mass range of galaxy clusters which are well resolved in optical and X-ray observations. The total number of those halos is 2004.

$M/10^{14}h^{-1}M_\odot$		> 2.5	$1.25 - 2.5$	$0.625 - 1.25$	total
single	$M_2/M_1 < 0.2$	171	429	1172	1772
multiple	$M_2/M_1 > 0.2$	32	68	132	232
total		203	497	1304	2004

Table 5.1: The numbers of single- and multiple-halos, where M_1 and M_2 are the masses of the main halo and the most massive substructure.

5.2.2 Morphology of FOF halos

Before modelling the 2004 simulated halos by triaxial ellipsoids, we classify the halos by the amount of substructures. This is useful in understanding the extent to which the definition of the non-sphericity of the FOF halos is sensitive to the presence of substructures.

Due to the nature of the FOF algorithm, an FOF halo may comprise two or more prominent components. Such a halo tends to yield higher non-sphericity, which should be distinguished from a very elongated *single* structure.

According to the result of the SUBFIND algorithm, we obtain the mass M_i of the i-th most massive component for each FOF halo. The most massive component ($i = 1$) is called the "main halo", and we call the other components "substructures". The values of M_2/M_1 and M_3/M_1 roughly serve as measures of amount of substructures in each FOF halo.

The upper-left, upper-right and lower-left panels of Figure 5.1 show the snapshots of FOF member particles of three halos with different morphology. The halo in the upper-left panel has very small values of M_2/M_1 and M_3/M_1, representing a single isolated structure. In contrast, the halo in the upper-right panel has relatively large M_2/M_1 and small M_3/M_1, corresponding to a "double-structure". The third halo in the lower-left panel has relatively large values both for M_2/M_1 and M_3/M_1, and is classified as a "triple-structure".

The lower-right panel of Figure 5.1 indicates the cumulative fraction of the halos with a given threshold of M_2/M_1 or M_3/M_1. The majority of our halos have small M_2/M_1 and even smaller M_3/M_1. For later convenience, we set the threshold $M_2/M_1 = 0.2$, and call a halo with $M_2/M_1 < 0.2$ a "single-halo". Also, a halo with $M_2/M_1 > 0.2$ is referred to as a "multiple-halo". Then the halos in the upper-right and the lower-left panels of Figure 5.1 are multiple-halos. Such multiple-halos occupy approximately 10 % of all the 2004 halos.

The threshold $M_2/M_1 = 0.2$ is somewhat arbitrary. According to the right panel of Figure 5.1, if we set the threshold by $M_2/M_1 = 0.1$, for example, ~ 20 % of our sample are classified as multiple-halos. As will be seen in the later sections, the choice of the threshold does not make a major difference in the main results of this chapter.

Table 1 lists the number of the single- and multiple-halos out of our sample, corresponding to the threshold $M_2/M_1 = 0.2$.
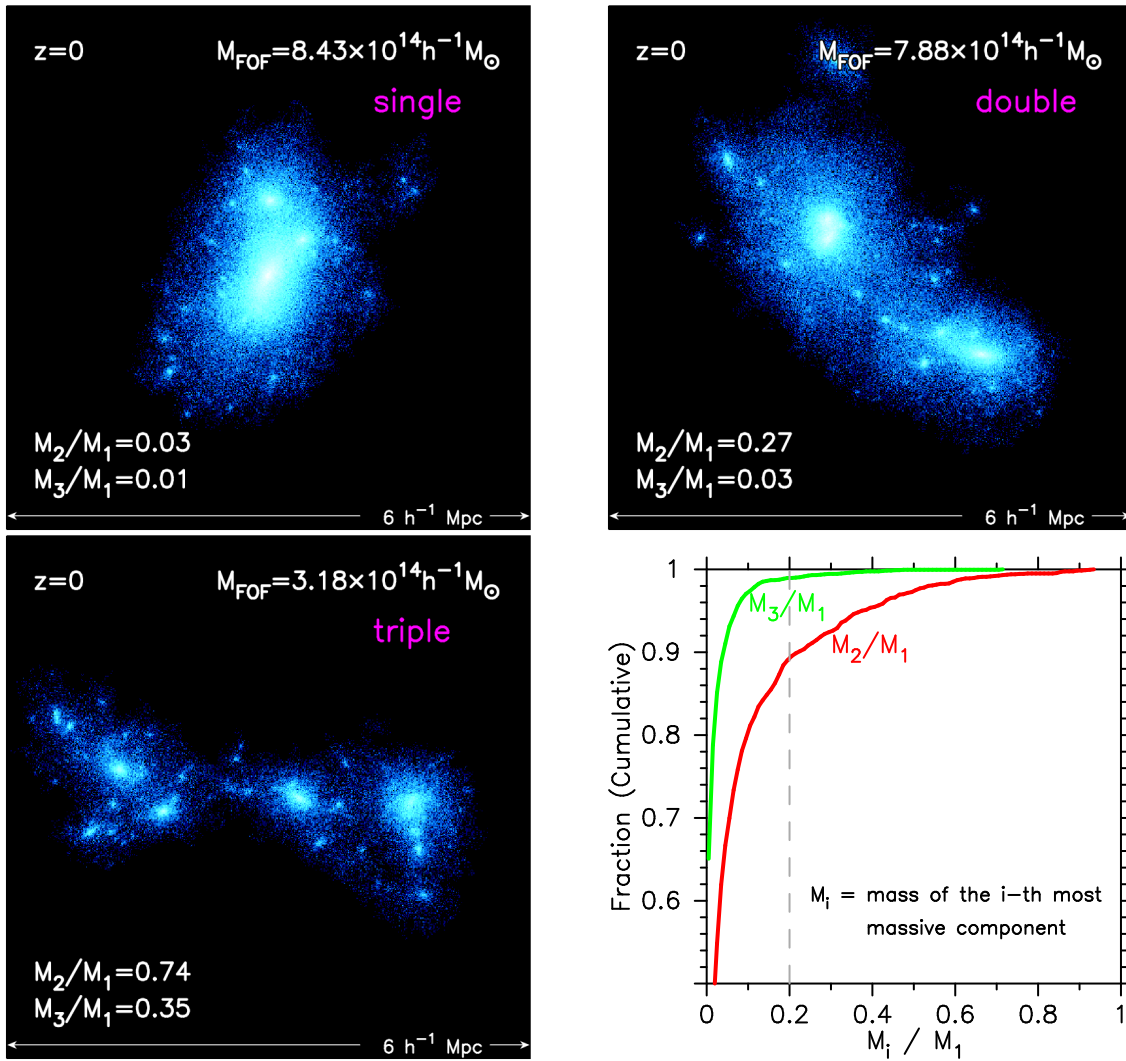
Figure 5.1: Examples of morphology of dark matter halos. The upper panels and the lower-left panel show the FOF member particles of halos comprising one, two and three major components in the cubic region 6 h^{-1} Mpc a side around the halo. The FOF mass $M_{\rm FOF}$ of each halo is 8.43, 7.88 and 3.18 $\times 10^{14} h^{-1} M_\odot$, respectively. The ratios of mass of the second and third massive components (M_2 and M_3) compared to the mass of the most massive one (main halo) M_1 are also indicated in the three panels. The cumulative fractions of M_2/M_1 and M_3/M_1 for our 2004 FOF halos are illustrated in the lower-right panel. For example, $\sim 90\,\%$ of the halos have $M_2/M_1 < 0.2$. In this chapter, we call the halos with $M_2/M_1 > 0.2$ "multiple-halos". In this figure, the halos in the upper-right and lower-left panels are multiple-halos.

5.2.3 Comparison of different methods of triaxial modelling: mass tensor vs. isodensity surface

We approximate the density distribution of the simulated halos by a triaxial ellipsoid with the axis lengths A_k ($k = 1, 2, 3$). The boundary of the ellipsoid is described by

$$\left(\frac{x_1}{A_1}\right)^2 + \left(\frac{x_2}{A_2}\right)^2 + \left(\frac{x_3}{A_3}\right)^2 = 1, \tag{5.1}$$

where x_k ($k = 1, 2, 3$) denotes the coordinate defined along the three axes with the origin set to the center of the ellipsoid.

One measure of the non-sphericity of each halo is the minor-to-major axis ratio A_1/A_3. The ellipticity e:

$$e = \frac{A_3 - A_1}{2(A_1 + A_2 + A_3)}. \tag{5.2}$$

is also used as an indicator of the non-sphericity in the literature. Thus we consider both A_1/A_3 and e in the following sections.

The values of axis lengths A_k are not constant for an entire simulated halo. Within the approximation of triaxial modelling, A_k should be expressed as $A_k(M_{\mathrm{ellipsoid}})$, where $M_{\mathrm{ellipsoid}}$ is the mass enclosed by the ellipsoid. Accordingly, A_1/A_3 and e also depend on $M_{\mathrm{ellipsoid}}$.

In this chapter, we compute the axis lengths $A_k(M_{\mathrm{ellipsoid}})$ on the basis of the mass tensor $I_{\alpha\beta}$ (defined below) in an iterative fashion as follows. For a given set of $A_k(M_{\mathrm{ellipsoid}})$, we compute the mass tensor $I_{\alpha\beta}$:

$$I_{\alpha\beta} = \sum_{i=1}^{N} x_\alpha^{(i)} x_\beta^{(i)}, \tag{5.3}$$

where $x_\alpha^{(i)}$ ($\alpha = 1, 2, 3$) is the coordinate of the i-th particle along the three axes of the ellipsoid, and the summation is taken over the $N(= M_{\mathrm{ellipsoid}}/m_{\mathrm{particle}})$ particles inside the ellipsoid. That mass tensor is now diagonalized and rotate the coordinate accordingly. The square root of the eigenvalues multiplied by some constant now become a new set of axis lengths $A_k(M_{\mathrm{ellipsoid}})$. The constant is determined so that the ellipsoid encloses $M_{\mathrm{ellipsoid}}$. The coordinate system is redefined along the new axis lengths $A_k(M_{\mathrm{ellipsoid}})$, and the center is reset to the center-of-mass of the particles inside the new ellipsoid. Starting from the sphere centered on the center-of-mass of the FOF members, the above procedure is iterated until all the eigenvalues converge within one percent. Hence, in the following parts of this chapter, the axis ratio A_1/A_3 and the ellipticity e are also determined roughly within one percent. In the above procedure, we use the all the particles *including substructures and non-FOF members*.

In literature, there are several methods to determine the axis lengths A_k of simulated halos, including isodensity surfaces and other definitions of mass tensors (JS02; Despali et al., 2014; Ludlow et al., 2014; Bonamigo et al., 2015; Vega et al., 2016). We decide to use the mass tensor $I = \sum xx$, and we explain why we prefer $I = \sum xx$ in what follows.

An alternative method to determine A_k is the direct fitting to local isodensity surfaces, as adopted by JS02. Since the shape of isodensity surface is sensitive to substructures

around halos, the removal of substructures is required in this method. The goal of this chapter is, however, to construct the PDF of projected non-sphericity of halos for observational applications. Since it is difficult to definitely remove the effect of substructures in real observations, we do not use isodensity surfaces in the later sections.

We note, however, that the fitting to isodensity surfaces yields similar results to the mass tensor $I = \sum xx$ after substructures are removed. Figure 5.2 shows the main halo of the same single-halo in top-left panel of Figure 5.1 *without substructures*. We also plot the projections of the two ellipsoids with the same mass determined by the mass tensor $I = \sum xx$ (green) and the isodensity surface $\rho = 100\rho_{\mathrm{crit}}$ (red), where ρ_{crit} is the cosmic critical density. The two ellipsoids are similar, indicating that the fitting to isodensity surfaces is an effective method to determine A_k if substructures are removed.

Slightly different versions of mass tensors are also used in literature, including the following two;

$$\hat{I}_{\alpha\beta} = \sum_{i=1}^{N} \frac{x_{\alpha}^{(i)} x_{\beta}^{(i)}}{|\boldsymbol{x}^{(i)}|^2} \equiv \sum_i n_{\alpha}^{(i)} n_{\beta}^{(i)} \tag{5.4}$$

and

$$\tilde{I}_{\alpha\beta} = \sum_i \frac{x_{\alpha}^{(i)} x_{\beta}^{(i)}}{[R_e^{(i)}]^2} \equiv \sum_i \tilde{n}_{\alpha}^{(i)} \tilde{n}_{\beta}^{(i)}, \tag{5.5}$$

where

$$R_e^{(i)} = \left[\left(\frac{x_1^{(i)}}{A_1} \right)^2 + \left(\frac{x_2^{(i)}}{A_2} \right)^2 + \left(\frac{x_3^{(i)}}{A_3} \right)^2 \right]^{1/2} \tag{5.6}$$

is the ellipsoidal distance of the i-th particle.

To discuss the difference between the three mass tensors $I = \sum xx$, $\hat{I} = \sum nn$ and $\tilde{I} = \sum \tilde{n}\tilde{n}$, we consider a "self-similar" density distribution. Throughout this chapter, we refer to the density distribution that is expressed by concentric ellipsoids with the same axis ratio and orientation as "self-similar" distribution.

For example, in the two-dimensional space, for a self-similar ellipse with axis lengths p and q, the two-dimensional counterparts of the mass tensors $I = \sum xx$, $\hat{I} = \sum nn$ and $\tilde{I} = \sum \tilde{n}\tilde{n}$ yield ellipses with axis ratio p/q, $\sqrt{p/q}$ and p/q, respectively. Although $\hat{I} = \sum nn$ can be used as an estimator of the non-sphericity of halos, it does not reproduce the axis ratio of isodensity surfaces even for a self-similar density distribution. In contrast, $\tilde{I} = \sum \tilde{n}\tilde{n}$ reproduces the isodensity surfaces of a self-similar density distribution, but the weighting by $R_e^{(i)}$ in Equation (5.5) is not appropriate when the density distribution is not self-similar. Hence we adopt the mass tensor $I = \sum xx$, which is free from such a weighting scheme and reproduces the isodensity surfaces of a self-similar density distribution.

The definition of mass tensor varies with authors in the previous literature, and therefore the applied method of triaxial modelling in each study should be carefully noticed. For example, JS02 fitted ellipsoids to isodensity surfaces of their simulated halos. Also, the mass tensors $I = \sum xx$, $\hat{I} = \sum nn$, $\tilde{I} = \sum \tilde{n}\tilde{n}$ are considered by Despali et al. (2014), Ludlow et al. (2014) and Vega et al. (2016), respectively (although the results of Vega et al. (2016) are mainly based on $I = \sum xx$). We emphasize that these results should not be *quantitatively* compared unless the same method of triaxial modelling is applied.
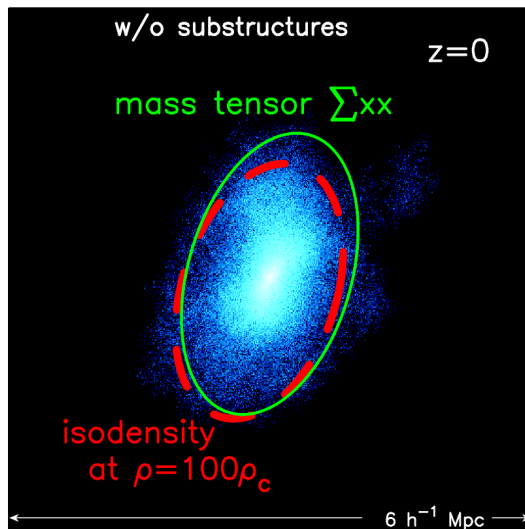
Figure 5.2: Same as the top-left panel of Figure 5.1, but excluding substructures. The projection of the ellipsoid fitted to the isodensity surface at $\rho = 100\rho_c$ is shown in the red dashed curve. The ellipsoid enclosing the same mass as that inside the isodensity surface ($M_{\mathrm{ellipsoid}} = 6.25 \times 10^{14} h^{-1} M_\odot$) is determined by using the mass tensor $I = \sum xx$ and its projection is plotted in the green solid curve. The resulting two ellipsoids are similar; $A_1/A_3 = 0.57$ (isodensity surface) and $A_1/A_3 = 0.55$ (mass tensor).

5.3 Confrontation of EC Prediction against N-body Results

On the basis of the ellipsoids defined via the mass tensor $I = \sum xx$ (Equation (5.3)), we compare the evolution of the individual simulated halos with the prediction of EC *on the object-wise basis*. For each FOF halo identified at $z = 0$, we trace back the positions of the FOF member particles to each redshift. We then determine an ellipsoid of mass M_{FOF} at each redshift via the mass tensor $I = \sum xx$ by using all the particles including non-FOF particles. Throughout this chapter, we call the ellipsoids determined at $z \neq 0$ through the above procedure "protohalos" of each FOF halo. Note that the protohalos are *not* halos identified by the FOF algorithm at each redshift.

Figure 5.3 demonstrates the evolution of the single-halo in the top-left panel of Figure 5.1 ($M_{\mathrm{FOF}} = 8.43 \times 10^{14} h^{-1} M_\odot$). The top-left panel shows the evolution of the axis lengths A_k of the protohalos enclosing $M_{\mathrm{ellipsoid}} = M_{\mathrm{FOF}}$ in units of their initial values at $z = 99$. The axis lengths A_k determined by the mass tensor are plotted in filled squares; A_1, A_2 and A_3 are plotted in red, green and blue, respectively. The corresponding EC predictions are illustrated in solid and dotted lines with the same color as the simulation results. The solid lines adopt λ_k evaluated from A_k of the corresponding protohalo at $z = 99$ through Equation (3.7); $\lambda_k = 1 - A_k(1 - \delta_{\mathrm{ini}}/3)/(A_1 A_2 A_3)^{1/3}$. On the other hand, the dashed lines identify λ_k with the eigenvalues of $\nabla_{ij}\phi/(4\pi G\bar{\rho}a^3)$ calculated from the top-hat smoothed density field at the scale $[3M_{\mathrm{FOF}}/(4\pi\bar{\rho})]^{1/3}$, at the central position of

the protohalo at $z = 99$. The difference between the solid and dashed lines implies that the EC prediction is somewhat sensitive to the initial conditions, but the two sets of lines are roughly the same.

The simulation results and the EC prediction agree at least approximately for $z < 9$. At around $z = 9$, however, the simulation results begin to deviate from the EC prediction. As shown in the top-right panel, the corresponding ellipticity (magenta open circle) becomes larger than the EC prediction (magenta thick line), even though the linear regime still holds at $z \sim 9$. The density distribution around the protohalo at $z = 9$ is shown in the middle-left panel, and the projections of the ellipsoids with mass $M_{\mathrm{ellipsoid}}/M_{\mathrm{FOF}} = 0.2, 0.4, 0.6, 0.8, 1$ are also plotted. The density distribution at $z = 9$ is almost homogeneous, and so the triaxial modelling of the density distribution is not easy.

In EC, Equation (3.10) assumes the density distribution inside the ellipsoid is homogeneous. Inside the simulated halo, however, the density distribution becomes highly inhomogeneous from $z = 3$ to $z = 1$, as shown in the middle-right and bottom-left panels; particles falls into the central region of the protohalo along filamentary structures, and the innermost region ($M_{\mathrm{ellipsoid}} \lesssim 0.2 M_{\mathrm{FOF}}$) becomes highly denser. Due to the filamentary structures developed during these redshifts, the triaxial modelling is still a poor approximation of the density distribution. The inhomogeneity of density distribution is one of the reasons why the simulation results deviate from the EC prediction. In addition, the internal density distribution is far from self-similar; for example, the orientation of the inner ellipsoids at $z = 1$ is considerably different from the outer ones.

Nevertheless, the evolution of the axis lengths A_k very crudely follows the EC prediction up to the turn-around epoch ($z \sim 1$) as seen in the top-left panel. Given that the various simplifications of EC, even this level of agreement between the simulation and EC may be surprising.

After the turn-around epoch, however, the simulation results more strongly deviate from the EC prediction. For example, the major axis A_3 (blue squares) rapidly increases and then decreases after $z = 1$. Finally at $z = 0$, the ellipticity e is much larger than the EC prediction (top-right panel), although the triaxial modelling of the density distribution seems to work well at $z = 0$ (bottom-right panel). The five ellipsoids at $z = 0$ in the bottom-right panel are well aligned compared to $z = 1$, but the density distribution is still not self-similar; the innermost ellipsoid is tilted with respect to the outermost one, and inner ellipsoids are slightly more elongated than outer ones.

As an another example, Figure 5.4 shows the results for another single-halo ($M_{\mathrm{FOF}} = 3.44 \times 10^{14} h^{-1} M_{\odot}$). Similarly to the case of Figure 5.3, especially after the turn-around epoch, the simulation results substantially deviate from the EC prediction. As seen in the bottom and middle panels, the density distribution inside the halo is not self-similar, as well as the halo in Figure 5.3.

We have found that the difference between the simulation and EC strongly depends on individual halos. Basically, however, the EC prediction very roughly reproduces the simulation results up to the turn-around. After that, the difference between the simulation and EC becomes larger.

One might expect that the difference between the simulation results and the EC prediction is larger for a multiple-halo than a single-halo. We have found that, however, this is not necessarily the case; the individuality of the halos is more noticeable.
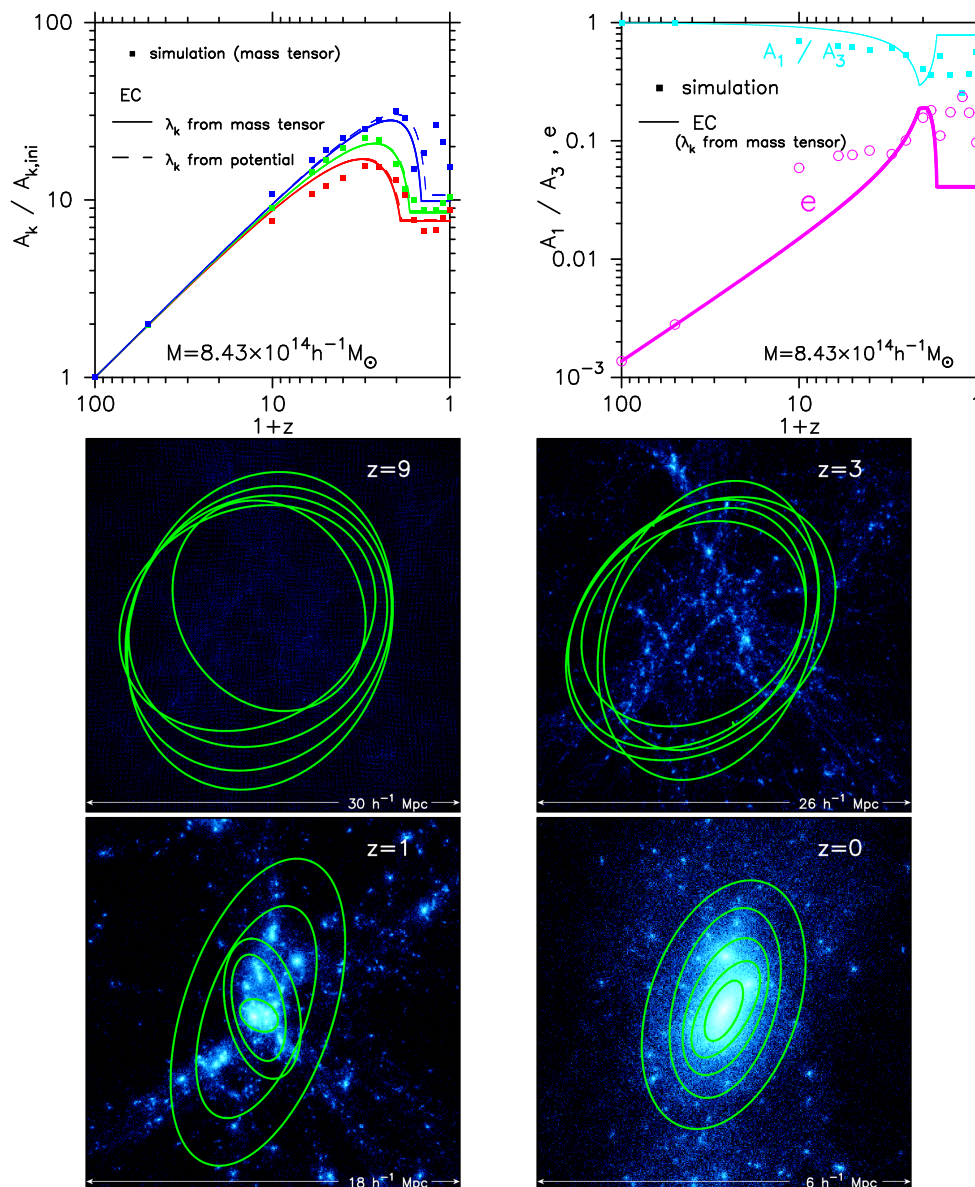
Figure 5.3: Evolution of the single-halo ($M_{\mathrm{FOF}} = 8.43 \times 10^{14} h^{-1} M_\odot$) plotted in the top-left panel of Figure 5.1. *top-left*: Evolution of the axis lengths A_k. The squares indicate A_k calculated from the mass tensor; A_1, A_2, A_3 are colored in red, green, blue, respectively. The solid lines indicate the EC prediction with the initial λ_k are calculated from A_k at $z = 99$ through Equation (3.7). The dashed lines are also the EC prediction, but the initial λ_k are eigenvalues of the tensor $\nabla_{ij}\phi/(4\pi G\bar\rho a^3)$ calculated from the top-hat smoothed density field at the scale $(3M_{\mathrm{FOF}}/(4\pi\bar\rho))^{1/3}$. *top-right*: Evolution of the axis ratio A_1/A_3 (cyan) and the ellipticity e (magenta); A_1/A_3: filled squares (simulation) and thin line (EC), e: open circles (simulation) and thick line (EC). *middle and bottom*: Density distributions around the halo at $z = 9$, 3, 1 and 0. The projections of the ellipsoids are determined by the mass tensor $I = \sum xx$ for the five different mass scales inside the halos ($M = (s/5)M_{\mathrm{FOF}}$; $s = 1,..., 5$) and plotted in green curves. All the particles including the non-FOF members are shown, and used in determining the ellipsoids.
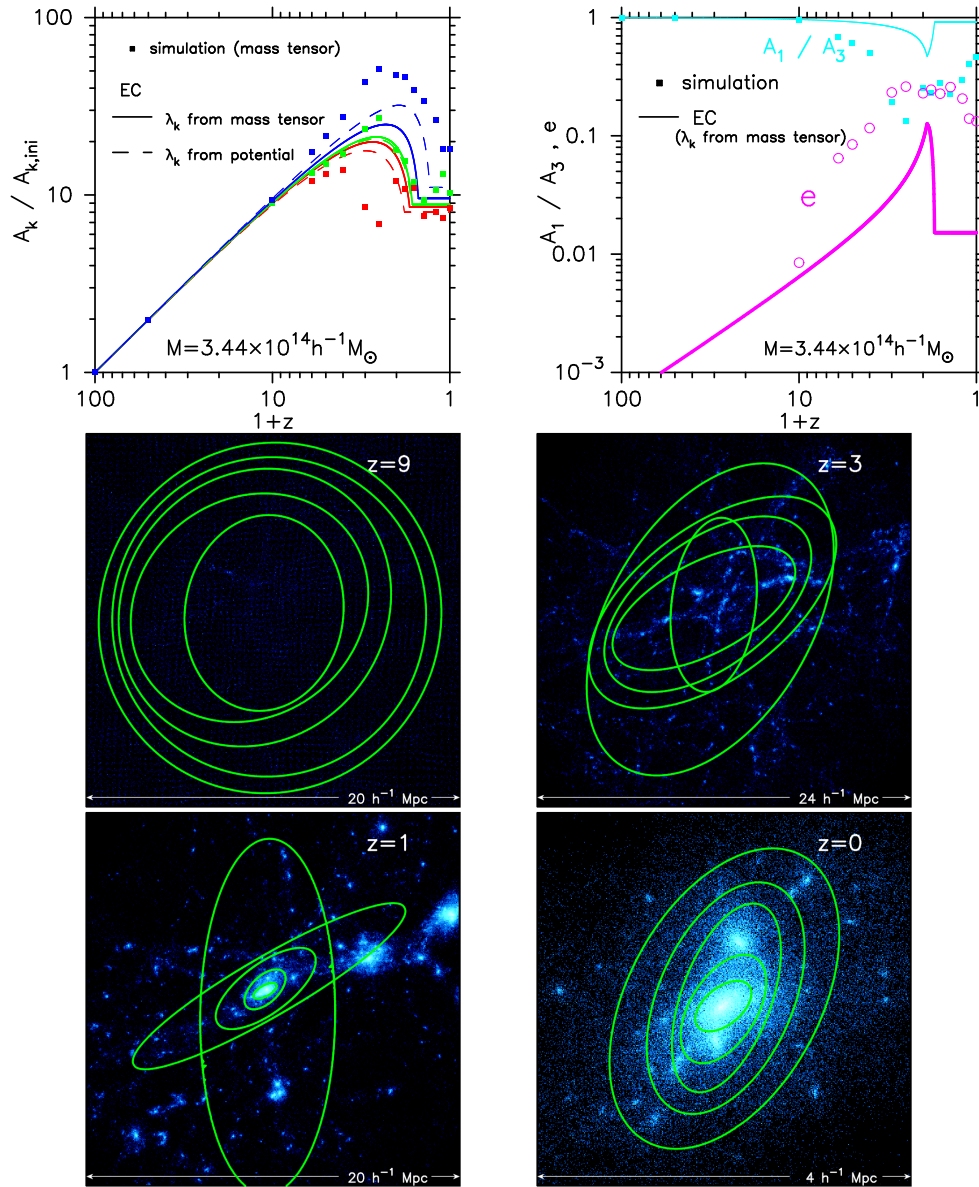
69

Figure 5.4: Same as Figure 5.3, but for another single-halo ($M_{\mathrm{FOF}} = 3.44 \times 10^{14}h^{-1}M_\odot$).

Actually, the difference between the model prediction and the simulation results is not peculiar to EC. In Chapter 4, we compare the evolution of the spherical radius of individual simulated halos with the prediction of the spherical collapse model. We then showed that the spherical collapse model fairly well reproduce the evolution of the simulation results up to the turn-around epoch. After the turn-around epoch, however, the evolution of simulated halos deviates from the prediction of the spherical collapse model. In this subsection, it has turned out that EC does not improve the difference between simulations and theoretical models. This rather implies that the spherical assumption works surprisingly well despite the highly non-spherical structure and evolution of halos.

In Chapter 4, we also showed the difference is mainly caused by the velocity dispersion

developed after the turn-around epoch. In order to better understand the difference between the simulation results and the EC prediction, we focus on the evolution of the simulated halos *after the turn-around epoch* ($z \sim 1$). Because the difference between the simulation results and the EC prediction varies appreciably from halo to halo, we *statistically* compare them in the next section.

5.4 Evolution and Statistics of Axis Ratio

5.4.1 Evolution and mass dependence of non-sphericity of halos

One of the well-known discrepancies between EC and simulations is the mass dependence of ellipticity of halos at $z = 0$. Rossi et al. (2011) calculated EC for initial conditions described by the Gaussian random field and reported that more massive halos have smaller ellipticity in EC, while those in simulations have larger ellipticity at $z = 0$.

We examine the evolution of axis ratio A_1/A_3 and ellipticity e of our simulated halos. We have found that the initial $\lambda_k(z = 99)$ measured from the simulation precisely reproduces the prediction for the Gaussian random field; more massive protohalos have smaller ellipticity at $z = 99$. Also, more massive halos indeed have larger ellipticity on average at $z = 0$ in our simulation, as reported in the previous studies Jing & Suto (2002); Despali et al. (2014); Bonamigo et al. (2015); Vega et al. (2016). Therefore the dependence of the non-sphericity of the simulated halos on their mass has changed sometime before the present time.

Figure 5.5 demonstrates the mass dependence of axis ratio A_1/A_3 and ellipticity e at $z = 9, 1, 0.6, 0.2, 0$. Each symbol indicates A_1/A_3 or e of each halo; red circles are for single-halos ($M_2/M_1 < 0.2$) and green square are for multiple-halos ($M_2/M_1 > 0.2$). Note that, for $z \neq 0$, the results are for the protohalos of each FOF halo identified at $z = 0$.

The thick solid line illustrates the averaged value $\langle A_1/A_3 \rangle$ or $\langle e \rangle$ over all the simulated halos with the root-mean-square scatter shown in thin lines. We have found that $\langle A_1/A_3 \rangle$ and $\langle e \rangle$ only slightly change if we exclude the multiple-halos, although they are systematically less spherical than single-halos. This is because the fraction of the multiple-halos is small ($\sim 10\%$). The blue dashed line indicates the EC prediction from the initial condition λ_k calculated from A_k at $z = 99$ through Equation (3.7).

As shown in the top-left panel of Figure 5.5, at $z = 9$, more massive halos have larger A_1/A_3 both in EC and the simulation results, reflecting the tendency at the initial time. The large scatter for the symbols implies the strong individuality of halos, i.e., the mass dependence of axis ratio is clear only when it is seen *statistically*. The simulation results have systematically smaller values of A_1/A_3 than the EC prediction, implying that the axis ratio A_1/A_3 of the majority of individual halos deviate from the EC prediction even at around $z = 9$, as in the top-right panel of Figure 5.3.

At $z = 1$ (second-top panel), the mass dependence is preserved in EC, but it becomes weaker at small mass scales for the simulated halos. From $z = 0.6$ to $z = 0$ (bottom three panels), $\langle A_1/A_3 \rangle$ becomes gradually larger. The increase of A_1/A_3 is predicted by EC as in the top-right panels of Figures 5.3 and 5.4, although the values of A_1/A_3 are much different between EC and the simulation.
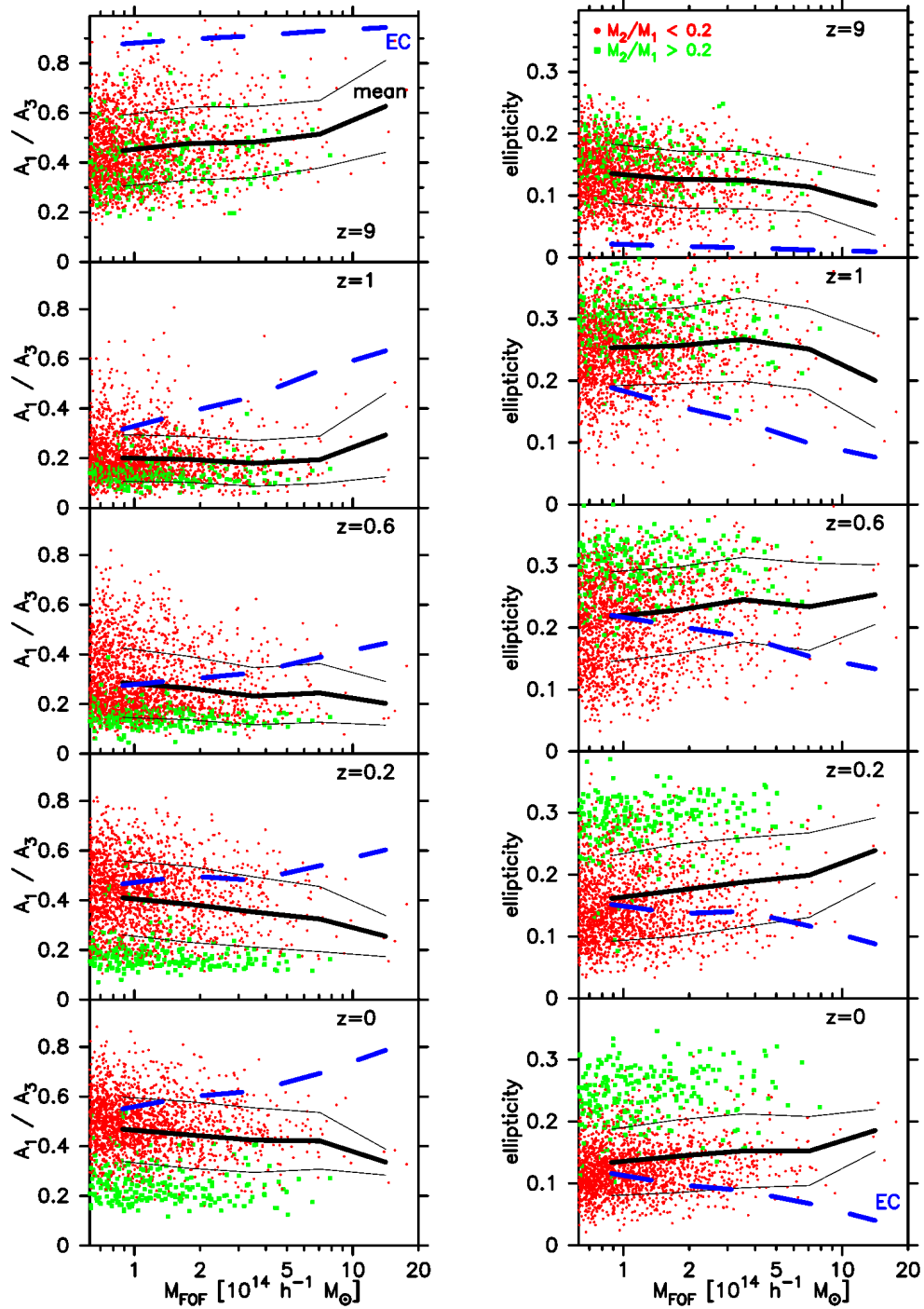
Figure 5.5: Axis ratio A_1/A_3 (left) and ellipticity e (right) of each halo against its FOF mass M_{FOF} at the five different redshift ($z = 9$, 1, 0.6, 0.2, 0). Each symbol indicates the result for each of the 2004 simulated halos; red circle are single-halos ($M_2/M_1 < 0.2$), green squares are for multiple-halos ($M_2/M_1 > 0.2$). The thick and thin solid lines indicate the mean and the standard deviation, respectively, for all the halos. For comparison, the blue dashed lines indicate the EC prediction calculated with the initial conditions λ_k determined from A_k at $z = 99$ of each halo through Equation (3.7). Note that the multiplicity (M_2/M_1) of the halos is determined only at $z = 0$.

72

Most importantly, the mass dependence of $\langle A_1/A_3 \rangle$ of the simulated halos exhibits a clear *transition* after $z = 1$; the mass dependence becomes even weaker, and finally at $z = 0$, massive halos tend to be less spherical, opposite to that at the initial time. In contrast, the mass dependence of $\langle A_1/A_3 \rangle$ in EC is preserved from the initial time to the present time; massive halos are more spherical. The mass dependence of $\langle e \rangle$ exhibits a similar transition to $\langle A_1/A_3 \rangle$, as shown in the right panels of Figure 5.5. The redshift $z = 1$ corresponds, on average, to the turn-around epoch where the difference between the EC prediction and the evolution of individual halos becomes large (see Figures 5.3 and 5.4). We then expect that a similar transition of the mass dependence of $\langle A_1/A_3 \rangle$ or $\langle e \rangle$ occurs earlier at inner mass scales of the halos, since inner regions turn-around earlier than outer regions.
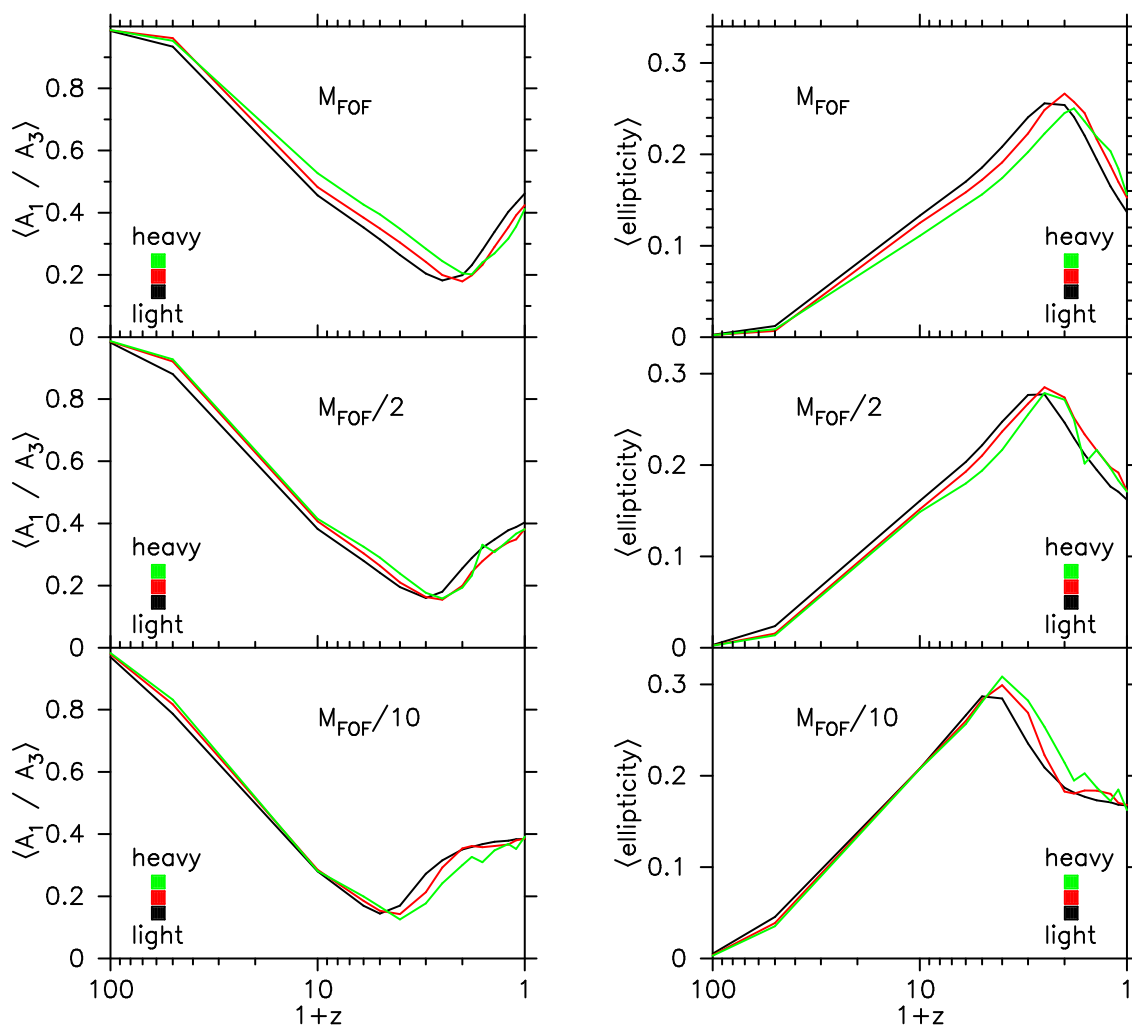

Figure 5.6: Evolution of the axis ratio $\langle A_1/A_3 \rangle$ (left) and ellipticity $\langle e \rangle$(right), averaged over the three different mass ranges ($M_{\mathrm{FOF}} > 2.5 \times 10^{14} h^{-1} M_\odot$; green, $1.25 \times 10^{14} h^{-1} M_\odot < M_{\mathrm{FOF}} < 2.5 \times 10^{14} h^{-1} M_\odot$; red and $6.25 \times 10^{13} h^{-1} M_\odot < M_{\mathrm{FOF}} < 1.25 \times 10^{14} h^{-1} M_\odot$; black) at the three different mass sales (M_{FOF}; top, $M_{\mathrm{FOF}}/2$; middle, $M_{\mathrm{FOF}}/10$; bottom).

To confirm this, we compute the $A_k(M_{\text{ellipsoid}})$ at the mass scales $M_{\text{ellipsoid}}(< M_{\text{FOF}})$ for each halo. Figure 5.6 compares the evolution of $\langle A_1/A_3 \rangle$ and $\langle e \rangle$ at the three different mass scales $M_{\text{ellipsoid}} = M_{\text{FOF}}$, $M_{\text{FOF}}/2$ and $M_{\text{FOF}}/10$. The values of A_k are averaged over the three different mass ranges; heavy: $M_{\text{FOF}} > 2.5 \times 10^{14} h^{-1} M_\odot$ (green), intermediate: $1.25 \times 10^{14} h^{-1} M_\odot < M_{\text{FOF}} < 2.5 \times 10^{14} h^{-1} M_\odot$ (red) and light: $6.25 \times 10^{13} h^{-1} M_\odot < M_{\text{FOF}} < 1.25 \times 10^{14} h^{-1} M_\odot$ (black).

The top-left panel of Figure 5.6 illustrates the redshift evolution of $\langle A_1/A_3 \rangle$ at $M_{\text{ellipsoid}} = M_{\text{FOF}}$. At $z = 99$, massive halos tend to be less spherical. Keeping this tendency, $\langle A_1/A_3 \rangle$ decreases up to $z \sim 1$, corresponding to the turn-around epoch. After that, $\langle A_1/A_3 \rangle$ begins to increase and its mass dependence changes, as seen in Figure 5.5.

The middle-left and the bottom-left panels of Figure 5.6 show the results for the mass scales $M_{\text{ellipsoid}} = M_{\text{FOF}}/2$ (middle) and $M_{\text{FOF}}/10$ (bottom), respectively. Indeed, the mass dependence of $\langle A_1/A_3 \rangle$ changes earlier at inner mass scales; at $z \sim 2$ for $M_{\text{FOF}}/2$, and at $z \sim 4$ for $M_{\text{FOF}}/10$. These redshifts approximately correspond to the turn-around epochs of the mass scales $M_{\text{FOF}}/2$ and $M_{\text{FOF}}/10$. Similar things occur also in the mass dependence of $\langle e \rangle$, as shown in the right panels of Figure 5.6.

Therefore the mass dependence of $\langle A_1/A_3 \rangle$ or $\langle e \rangle$ changes after the turn-around epoch of each region. We then suspect that the change in the mass dependence may be related to the development of the velocity dispersion after the turn-around epoch. Hence we examine the radial profile of the velocity dispersion after $z = 1$ and compare it with the radial profiles of $\langle A_1/A_3 \rangle$ and $\langle e \rangle$ in the next subsection.

5.4.2 Radial profile of axis ratio inside FOF halos and the origin of the mass dependence of axis ratio

Figure 5.7 shows the radial profiles of the radial velocity dispersion σ_r^2 and the "velocity isotropy measure" defined by $(\sigma_\theta^2 + \sigma_\varphi^2)/(2\sigma_r^2)$ at $z = 1, 0.8, 0.6, 0.4, 0.2, 0.1, 0$ (after the turn-around epoch). We here use spherical mass coordinate M_{sphere} for simplicity, and calculate each component of velocity dispersion in the spherical coordinate. In the left panel, the radial velocity dispersion σ_r^2 is normalized by the circular velocity $v_{\text{circ}}^2(M_{\text{FOF}})$ at $M_{\text{sphere}} = M_{\text{FOF}}$:

$$v_{\text{circ}}^2(M_{\text{FOF}}) = \frac{GM_{\text{FOF}}}{R_{\text{FOF}}}, \tag{5.7}$$

where R_{FOF} is the radius of the sphere enclosing the mass M_{FOF}. We first compute the radial profiles of $\sigma_r^2/v_{\text{circ}}^2$ and $(\sigma_\theta^2 + \sigma_\varphi^2)/(2\sigma_r^2)$ for an individual halo, and then average further the radial profiles over the 2004 halos to obtain the "mean" radial profiles, $\langle \sigma_r^2/v_{\text{circ}}^2 \rangle$ and $s \equiv \langle (\sigma_\theta^2 + \sigma_\varphi^2)/(2\sigma_r^2) \rangle$. Note that, for $z \neq 0$, the results are for the protohalos of each FOF halo identified at $z = 0$. We have confirmed that the radial profiles in Figure 5.7 are almost unchanged even if we include/exclude the multiple-halos.

The left panel of Figure 5.7 indicates that the radial velocity dispersion $\langle \sigma_r^2/v_{\text{circ}}^2 \rangle$ is larger at the innermost regions at every redshift. At around $M_{\text{sphere}} = M_{\text{FOF}}$, σ_r^2 rapidly decreases and becomes roughly constant at outer regions. The small values of $\langle \sigma_r^2/v_{\text{circ}}^2 \rangle$ at outer regions can be attributed to the particles coherently falling toward the central region with small radial velocity dispersion.

In the right panel of Figure 5.7, the averaged radial profile of the velocity isotropy measure s at each redshift has roughly three different regions. At the innermost region, s is approximately unity, indicating that the velocity is almost isotropic. At around $M_{\mathrm{sphere}} = M_{\mathrm{FOF}}$, s rapidly increases, corresponding to the decrease of $\langle \sigma_r^2/v_{\mathrm{circ}}^2 \rangle$ in the left panel. Then s reaches a maximum. We indicate the maximum point by an arrow in the figure. Outside the maximum point, s slowly decreases.

We indicate the location where the velocity isotropy measure s reaches the maximum by an arrow also in the left panel. At this location, the radial profile of $\langle \sigma_r^2/v_{\mathrm{circ}}^2 \rangle$ becomes roughly flat. We find that this location approximately corresponds to the "splash-back radius" r_{sb} (Adhikari et al., 2014; Diemer & Kravtsov, 2014; More et al., 2015) that represents the physical halo boundary. We note that r_{sb} moves outward with time, indicating that the velocity dispersion develops and extends outward. We next examine how the radial profiles of the axis ratio $\langle A_1/A_3 \rangle$ and $\langle e \rangle$ behaves inside and outside r_{sb}.

Figure 5.8 illustrates the radial profiles of axis ratio $\langle A_1/A_3 \rangle$ and ellipticity $\langle e \rangle$ averaged over our 2004 halos for $z = 1, 0.8, 0.6, 0.4, 0.2, 0.1, 0$. The horizontal axis $M_{\mathrm{ellipsoid}}$ indicates the mass of ellipsoids determined by the mass tensor $I = \sum xx$ using internal and external density distributions for each halo. We refer to the sequence of $\langle A_1/A_3 \rangle$ or $\langle e \rangle$ of such ellipsoids as "radial profiles". Note that the central position differs from inner to outer ellipsoids belonging to the same FOF halo (see bottom panels of Figures 5.3 and 5.4). We have confirmed that the radial profiles in Figure 5.8 are almost unchanged even if we include/exclude the multiple-halos.

The left panel of Figure 5.8 shows the evolution of the radial profile of $\langle A_1/A_3 \rangle$. At least after $z \sim 0.4$, the radial profile of $\langle A_1/A_3 \rangle$ rapidly decreases beyond a certain mass scale around $M_{\mathrm{ellipsoid}} \sim M_{\mathrm{FOF}}$. Similarly, as shown in the right panel of Figure 5.8, the profile of ellipticity $\langle e \rangle$ rapidly increases there. This corresponds to the development of filamentary structures surrounding the halos (cf. the bottom-left panel of Figure 5.3). The characteristic mass scale moves outward with time, and eventually becomes larger than M_{FOF} after $z \lesssim 0.4$.

We indicate the location where the velocity isotropy measure s reaches a maximum, roughly corresponding to the splash-back radius r_{sb}, at each redshift by an arrow in both panels of Figure 5.8. The characteristic mass scale in the radial profile of $\langle A_1/A_3 \rangle$ or $\langle e \rangle$ roughly corresponds to r_{sb}, given that M_{sphere} is not exactly identical to $M_{\mathrm{ellipsoid}}$. These two mass scales may give a rough indication of the physical boundary of halos inside which the velocity dispersion has been developed.

Figures 5.5 to 5.8 imply that the mass dependence of axis ratio $\langle A_1/A_3 \rangle$ changes almost simultaneously the velocity dispersion $\langle \sigma_r^2/v_{\mathrm{circ}}^2 \rangle$ becomes larger. We note, however, that the halos have a significant mean ellipticity $\langle e \rangle$ inside the splash-back radius r_{sb}. This may seem inconsistent with the fact that the velocity dispersion is almost isotropic at the innermost region (Figure 5.7). Hence some unknown mechanism other than the velocity anisotropy is needed to maintain the highly non-spherical density distribution of the halos, which remains as a puzzle.

Figure 5.8 shows that the radial dependence of $\langle A_1/A_3 \rangle$ or $\langle e \rangle$ at $M_{\mathrm{ellipsoid}} \lesssim M_{\mathrm{FOF}}$ gradually changes from $z = 1$ to $z = 0$. While inner regions are more spherical at $z = 1$, inner regions are less spherical at $z = 0$. This radial dependence may seem small, but indicates that the halos are not self-similar. In the next section, we examine how the PDF
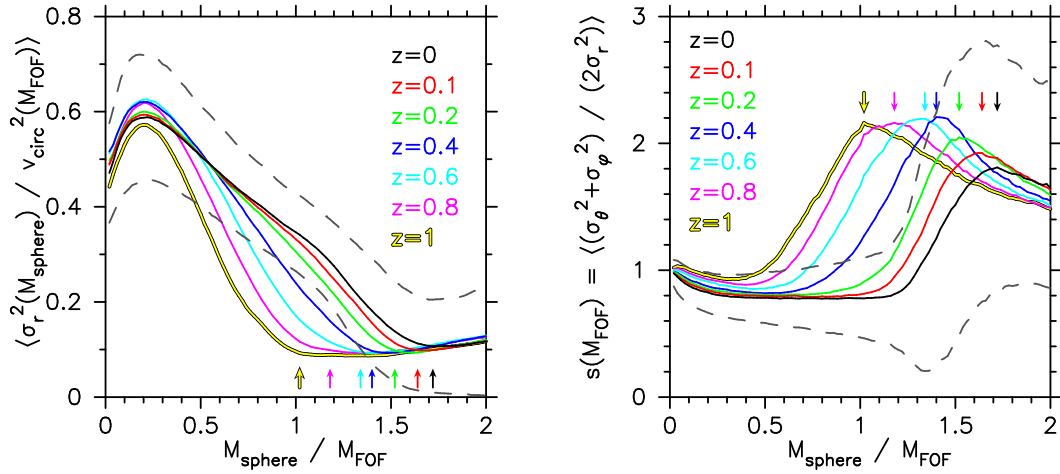
of A_1/A_3 depends on $M_{\text{ellipsoid}}$.

Figure 5.7: Radial profiles of the radial velocity dispersion σ_r^2 (left) and the velocity isotropy measure $s = (\sigma_\theta^2 + \sigma_\varphi^2)/(2\sigma_r^2)$ (right), averaged over the 2004 simulated halos, at the seven different redshifts; $z = 1, 0.8, 0.6, 0.4, 0.2, 0.1, 0$. The velocity dispersion in the left panel is normalized by the circular velocity $v_{\text{circ}}^2(M_{\text{FOF}}) = GM_{\text{FOF}}/R_{\text{FOF}}$ of each halo at each redshift. The dashed lines indicate the standard deviation for $z = 0$. At each redshift, the mass scale where s reaches a maximum is indicated by an arrow in both panels.
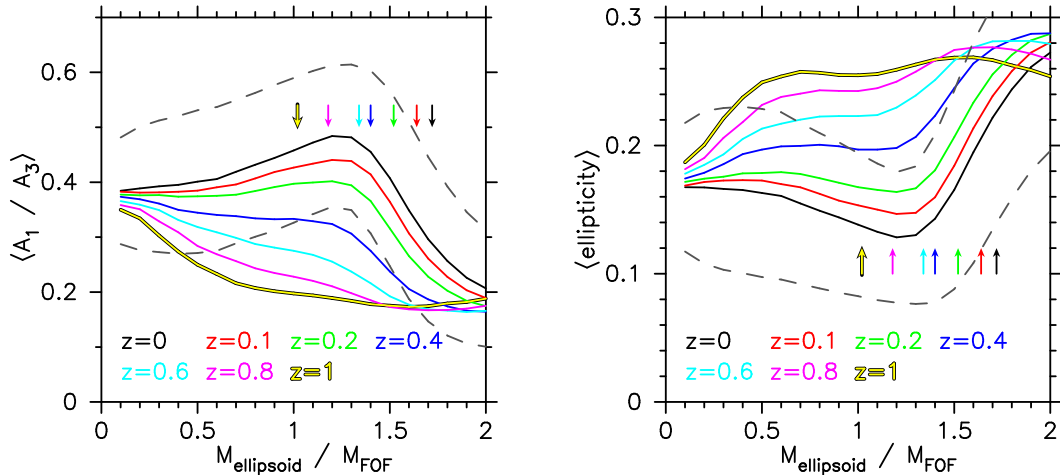

Figure 5.8: Radial profiles of the axis ratio $\langle A_1/A_3 \rangle$ (left) and the ellipticity $\langle e \rangle$ (right), averaged over the 2004 simulated halos, at the seven different redshifts; $z = 1, 0.8, 0.6, 0.4, 0.2, 0.1, 0$. The dashed lines indicate the standard deviation for $z = 0$. At each redshift, the *spherical* mass scale where s reaches a maximum (Figure 5.7) is indicated by an arrow for both panels.

5.4.3 Probability distribution function of axis ratio

Previously, JS02 measured the minor-to-major axis ratio A_1/A_3 of the isodensity surface at $\rho = 2500\rho_c$ (approximately corresponding to 0.3 $r_{\rm vir}$) of their simulated halos. They further assumed the self-similarity of the density distribution inside the halos, and obtained the following fitting formula at the virial mass $M_{\rm vir}$:

$$
\begin{aligned}
P(A_1/A_3; M_{\rm vir}, z) = \frac{1}{\sqrt{2\pi}0.113} \left(\frac{M_{\rm vir}}{M_*}\right)^{0.07\Omega_m(z)^{0.7}} \\
\times \exp\left[\frac{[(A_1/A_3)(M_{\rm vir}/M_*)^{0.07\Omega_m(z)^{0.7}} - 0.54]^2}{2(0.113)^2}\right],
\end{aligned}
\tag{5.8}
$$

where $M_*(z)$ is the characteristic non-linear mass scale. The scale is determined so that the top-hat smoothed mass fluctuation $\sigma(M_*, z)$ becomes $\delta_c = 1.68$, where δ_c is the linearly-extrapolated critical density contrast in the spherical collapse model.

In the previous subsection, however, we have seen that the axis ratio $A_1/A_3(M_{\rm ellipsoid})$ is not constant as a function of $M_{\rm ellipsoid}$ (Figure 5.8). This result implies that the formula (5.8) may not be reliable since it is based on the self-similarity assumption. Therefore, we here quantitatively show the extent to which the departure from self-similarity affects the probability distribution function (PDF) of A_1/A_3.

Figure 5.9 illustrates the PDFs of axis ratio A_1/A_3 of our 2004 halos, determined by $I = \sum xx$ at the three different mass scales $M_{\rm ellipsoid} = M_{\rm FOF}$, $M_{\rm FOF}/2$ and $M_{\rm FOF}/10$. The simulated halos are classified into three categories according to the mass of the most massive substructure M_2 compared to that of the main halo M_1; $M_2/M_1 < 0.1$ (red), $0.1 < M_2/M_1 < 0.2$ (blue), $M_2/M_1 > 0.2$ (green). The red and blue portions correspond to the single-halos defined in Section 2.2, and the green portion corresponds to the multiple-halos.

The bottom panel of Figure 5.9 shows the result for $M_{\rm ellipsoid} = M_{\rm FOF}/10$, approximately corresponding to the region enclosed by the isodensity surface $\rho = 2500\rho_c$. The PDF of our halos is shifted to the left compared to Equation (5.8). Their difference may be partly explained by the different methods of triaxial modelling of halos; the mass tensor and the isodensity surfaces.

As shown in the middle panel of Figure 5.9, the PDF of A_1/A_3 for $M_{\rm ellipsoid} = M_{\rm FOF}/2$ is shifted to the right compared with that of $M_{\rm FOF}/10$. Hence the region at $M_{\rm ellipsoid} = M_{\rm FOF}/2$ inside the halos is, on average, more spherical than $M_{\rm FOF}/10$, corresponding to the radial profiles of A_1/A_3 and e in Figure 5.8. Similarly, as shown in the top panel, the region $M_{\rm ellipsoid} = M_{\rm FOF}$ is even more spherical, clearly indicating that the PDF of A_1/A_3 depends on $M_{\rm ellipsoid}$ due to the non-self-similarity of halos. Quantitatively, the mean value $\langle A_1/A_3 \rangle$ at $M_{\rm ellipsoid} = M_{\rm FOF}/2$ and $M_{\rm ellipsoid} = M_{\rm FOF}/10$ is smaller by $\sim 10\%$ and $\sim 15\%$ than that at $M_{\rm ellipsoid} = M_{\rm FOF}$.

For $M_{\rm ellipsoid} = M_{\rm FOF}$, the PDF of our halos is similar to Equation (5.8), except for the fraction by the multiple-halos. This is most likely just a coincidence; the difference in A_k by the mass tensor and the isodensity surfaces, and the radial profile of A_1/A_3 are accidentally compensated. At $M_{\rm ellipsoid} = M_{\rm FOF}/2$ and $M_{\rm FOF}$, the multiple-halos are significantly less spherical than single-halos. In contrast, the multiple-halos do not have

such a tendency at $M_{\mathrm{ellipsoid}} = M_{\mathrm{FOF}}/10$. This is because the multiplicity of halos is determined by the amount of substructures with all the FOF members; For example, the region of $M_{\mathrm{FOF}}/10$ of a halo comprising two comparable mass objects may include only one of them.

Previously, Vega et al. (2016) calculated the PDF of A_1/A_3 of their simulated halos at the two different mass scales $M_{\mathrm{ellipsoid}} \approx M_{\mathrm{FOF}}$ and $M_{\mathrm{ellipsoid}} \approx M_{\mathrm{FOF}}/2$ *without* the self-similarity assumption. They then found that $\langle A_1/A_3 \rangle$ at the inner mass scale is smaller by $\sim 10\,\%$ than that at the outer mass scale. This is consistent with our results, although their methods of triaxial modelling and halo identification are slightly different from ours.
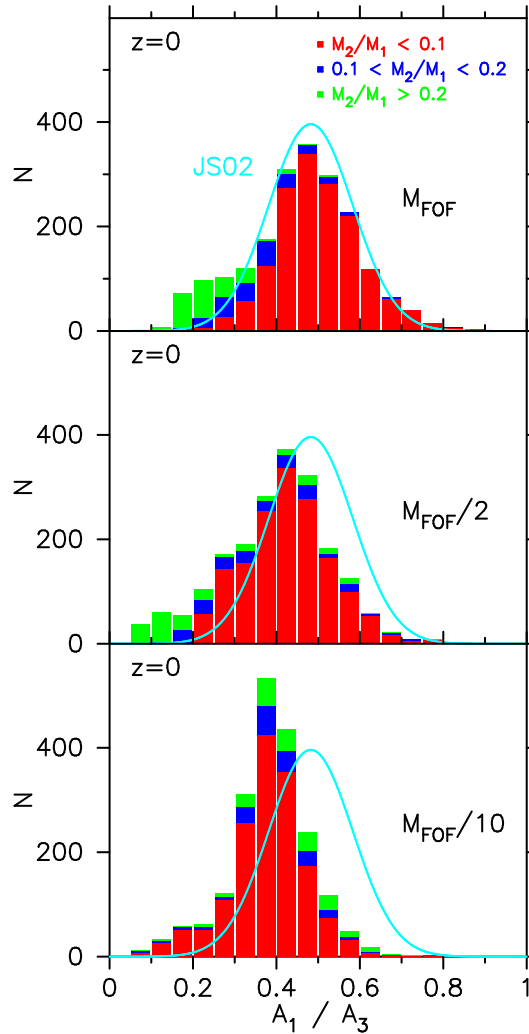

Figure 5.9: PDF of the minor-to-major axis ratio A_1/A_3 of triaxial ellipsoid at $z = 0$ for the three different mass scales: $M_{\mathrm{ellipsoid}} = M_{\mathrm{FOF}}$, $M_{\mathrm{FOF}}/2$ and $M_{\mathrm{FOF}}/10$. The histogram is divided by three types of halos; $M_2/M_1 < 0.1$ (red), $0.1 < M_2/M_1 < 0.2$ (blue), $M_2/M_1 > 0.2$ (green). The cyan curve shows the fitting formula of JS02 (Equation (5.8)) that is based on the isodensity surface $\rho = 2500\rho_c$, approximately corresponding to $0.3r_{\mathrm{vir}}$ and $M_{\mathrm{FOF}}/10$.

In observations, since the density distribution of halos is projected on the sky, the PDF of projected axis ratio is more relevant in interpreting observational data. In fact, OLS03 calculated the PDF of projected axis ratio by integrating imaginary halos whose axis lengths A_k follow the formula (5.8). The scale dependence of the PDF of A_1/A_3 indicates that the self-similar assumption is not valid when constructing a PDF of projected axis ratio through a PDF of A_1/A_3, as employed previously (e.g., OLS03; Kawahara, 2010). Therefore, we instead directly measure the projected axis lengths by projecting the density distribution of the simulated halos in the next subsection.

5.5 Probability Distribution Function of Projected Axis Ratio

5.5.1 Axis ratio of projected density distribution from simulations

Figure 5.10 (a) shows the histograms of the projected axis ratio of our halos at $z = 0$. Instead of M_{FOF}, $M_{\mathrm{FOF}}/2$, $M_{\mathrm{FOF}}/10$ in Figure 5.9, we measure three observationally more relevant mass scales; M_{vir}, M_{500} and M_{2500}. The virial mass M_{vir} is defined as the mass of the sphere within which the averaged overdensity becomes $\Delta_{\mathrm{vir}}(z = 0) = 355.4$ times cosmic mean matter density, and M_{500} and M_{2500} are the masses of the sphere within which the mean density is 500 and 2500 times the cosmic critical density. Actual lensing halos are observed roughly up to the scale of M_{500}. Typically, $M_{500} \sim 0.5 M_{\mathrm{vir}}$ and $M_{2500} \sim 0.2 M_{\mathrm{vir}}$. In reality, these mass scales are measured from the projected density distribution on the sky, but here we determine them in the three-dimensional space for simplicity.

We determine an ellipse by using the two dimensional counterpart of $I = \sum xx$ from the projected density distributions of each halo along the x-, y- and z-axes of our simulation. We choose a rectangular box with the depth only along the line-of sight confined so that the region barely encloses all the FOF member particles. Therefore we consider all the particles in the box, but neglect the contribution from foreground and background particles outside the box. The particle number N in Equation (5.3) is set so that the (projected) mass inside the ellipse becomes any of M_{vir}, M_{500} and M_{2500}. We call the axis lengths of the resulting ellipse a_1 and a_2 ($a_1 < a_2$). Note that we obtain three values of a_1/a_2 for each halo.

The top panel of Figure 5.10 (a) shows the histogram for M_{vir} ($\approx M_{\mathrm{FOF}}$) at $z = 0$. The histogram is separately colored by single-halos ($M_2/M_1 < 0.2$) and multiple-halos ($M_2/M_1 > 0.2$). Due to the projection effect, the overall shape of the histogram is broader and more shifted to the right (rounder) than that of A_1/A_3 for M_{FOF} in Figure 5.9. Also, compared to A_1/A_3, the portion of the multiple-halos in the PDF is extended to the right; if two major components of a multiple-halo are along the line-of-sight, it may be regarded a single object from an observer.

We find that the histogram of projected axis ratio is well approximated by the beta

distribution:

$$P(x; a, b) = \frac{x^{a-1}(1-x)^{b-1}}{B(a, b)},$$ (5.9)

where

$$B(a, b) = \int_0^1 x^{a-1}(1-x)^{b-1}dx$$ (5.10)

is the beta function and a and b are parameters. The mean μ and the variance σ^2 of the beta distribution are given by

$$\mu = \frac{a}{a+b}, \qquad \sigma^2 = \frac{ab}{(a+b)^2(a+b+1)},$$ (5.11)

respectively. Table 2 lists the parameters a and b along with the mean value and the standard deviation calculated from a and b. The values of mean μ and variance σ^2 do not change much even when we include/exclude the multiple-halos. Such weak dependence on the multiplicity of halos is useful when the fitting formula is compared with real observational data, since it is difficult to determine the multiplicity of real halos, and to remove substructures in observations.

Our result should be compared with the PDF of a_1/a_2 by OLS03 that integrates the PDF of A_1/A_3 by JS02. We emphasize that the PDF of OLS03 is sensitive to the self-similarity assumption by JS02. When calculating the PDF of OLS03, we substitute $M_{\rm vir} = 2 \times 10^{14} h^{-1} M_\odot$ in Equation (5.8), corresponding to the mean mass of our sample. The PDF of OLS03 is plotted in blue dashed curve in Figure 5.10. Since the PDF of A_1/A_3 for $M_{\rm FOF}(\approx M_{\rm vir})$ well follows the model of JS02 by coincidence (the top-panel of Figure 5.9), the difference between OLS03 and the histogram is mainly due to the self-similarity assumption for the density distribution inside halos, adopted by JS02 and OLS03. This difference clearly demonstrates the importance of the projection effect.

The middle and bottom panels of Figure 5.10 (a) show the histograms for M_{500} and M_{2500}, respectively, compared with OLS03. Since OLS03 assumes the self-similarity of density distribution, the blue-dashed curves in the three panels of Figure 5.10 (a) are the same. These histograms show that the inner region is slightly less spherical than the outer region. This dependence is similar to the case of A_1/A_3 (Figure 5.9), but significantly weaker due to the projection.

The PDF of a_1/a_2 at M_{500} and M_{2500} are also well approximated by the beta distribution, and the best-fit parameters are listed in Table 2. It may seem that, for M_{2500}, the PDF of OLS03 is in better agreement in the simulation results. Given that the significant difference in the bottom panel of Figure 5.9 at $M_{\rm FOF}/10$, however, this is also just a coincidence, and rather implies the importance of the projection effect for non-self-similar halos.

We repeat the same analysis for $z = 0.2$, 0.4 and 1. In doing so, we find halos by the FOF algorithm *at each redshift separately*; in the preceding sections, we have traced back the evolution of protohalos of each FOF halo identified at $z = 0$, which does not correspond to real observational situations because observed halos are defined at each z. The multiplicity of the halos is also defined at each redshift, according to the mass of the most massive substructure M_2 relative to that of the main halo M_1. In addition, we

extract halos with $M_{vir} > 6.25 \times 10^{13} h^{-1} M_\odot$ at each redshift. Hence the number of the halos depends on redshift, and is indicated in Figure 5.10 and Table 2. Note that the virial overdensity $\Delta_{vir}(z)$ depends on redshift; e.g., $\Delta_{vir}(z=1) = 203.2$.

Figure 5.10 (b), (c) and (d) show the results for halos at higher redshifts; $z = 0.2$, 0.4 and 1, respectively. For each redshift, the PDF of OLS03 (blue curves) in the three panels are the same, but it slightly differs with redshift. The result for every redshift is basically similar to $z = 0$. Also, all the histograms are well approximated by the beta distribution (Equation (5.9)) and best-fit parameters are listed in Table 2.
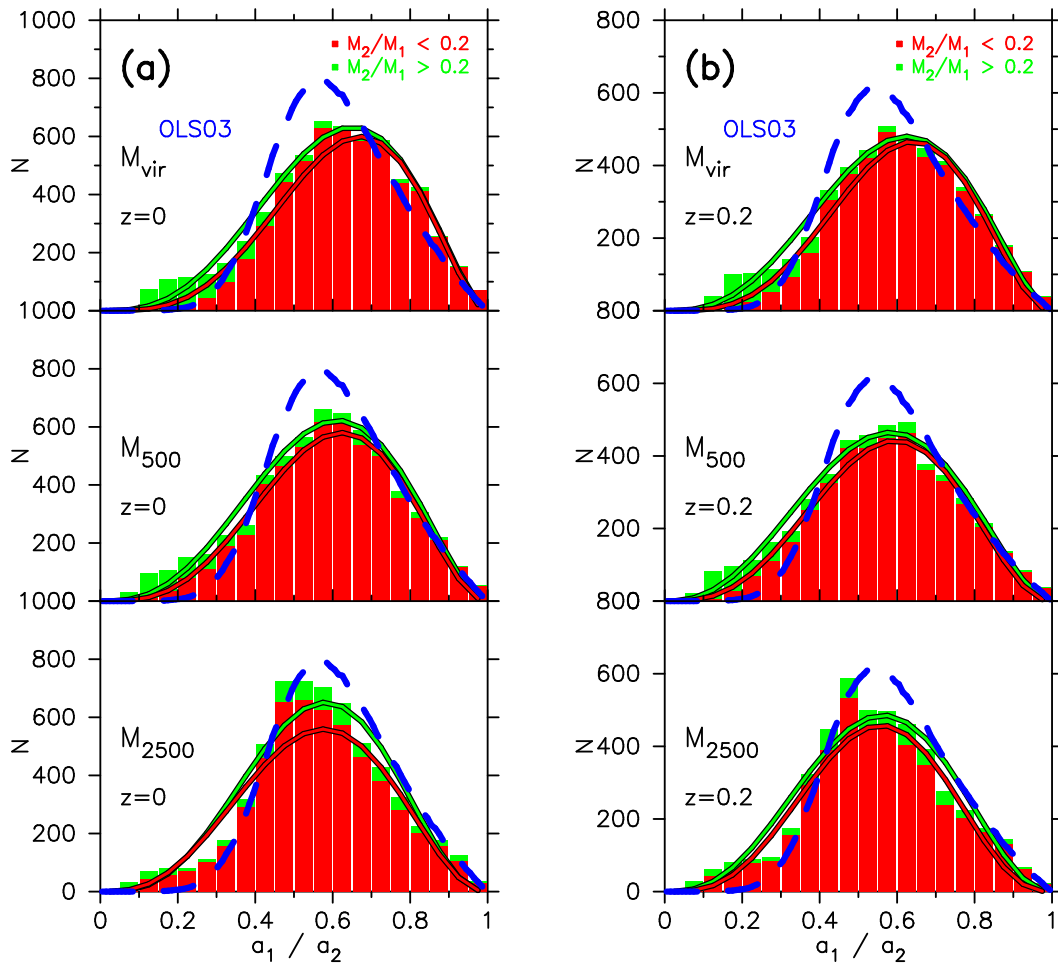

Figure 5.10: PDF of the projected axis ratio at the three different mass scale M_{vir} M_{500} and M_{2500}, for four redshifts; $z = 0$ (a), 0.2 (b), 0.4 (c), 1 (d). The solid curves show the best-fit beta distributions (our model). For comparison, the PDF by OLS03 (based on JS02) is also shown. The histogram is colored according to the multiplicity of halos; $M_2/M_1 < 0.2$ (red), $M_2/M_1 > 0.2$ (green). The multiplicity of halos (M_2/M_1) is determined separately at each redshift. When calculating the PDF of OLS03, $M = 2 \times 10^{14} h^{-1} M_\odot$, corresponding to the mean mass of our halos, is substituted in Equation (5.8). Only the simulated halos with $M_{vir}(z) > 6.25 \times 10^{13} h^{-1} M_\odot$ are selected at each redshift, and the number of halos is 3×2004 ($z = 0$), 3×1550 ($z = 0.4$), 3×1101 ($z = 0.2$), 3×317 ($z = 1$).
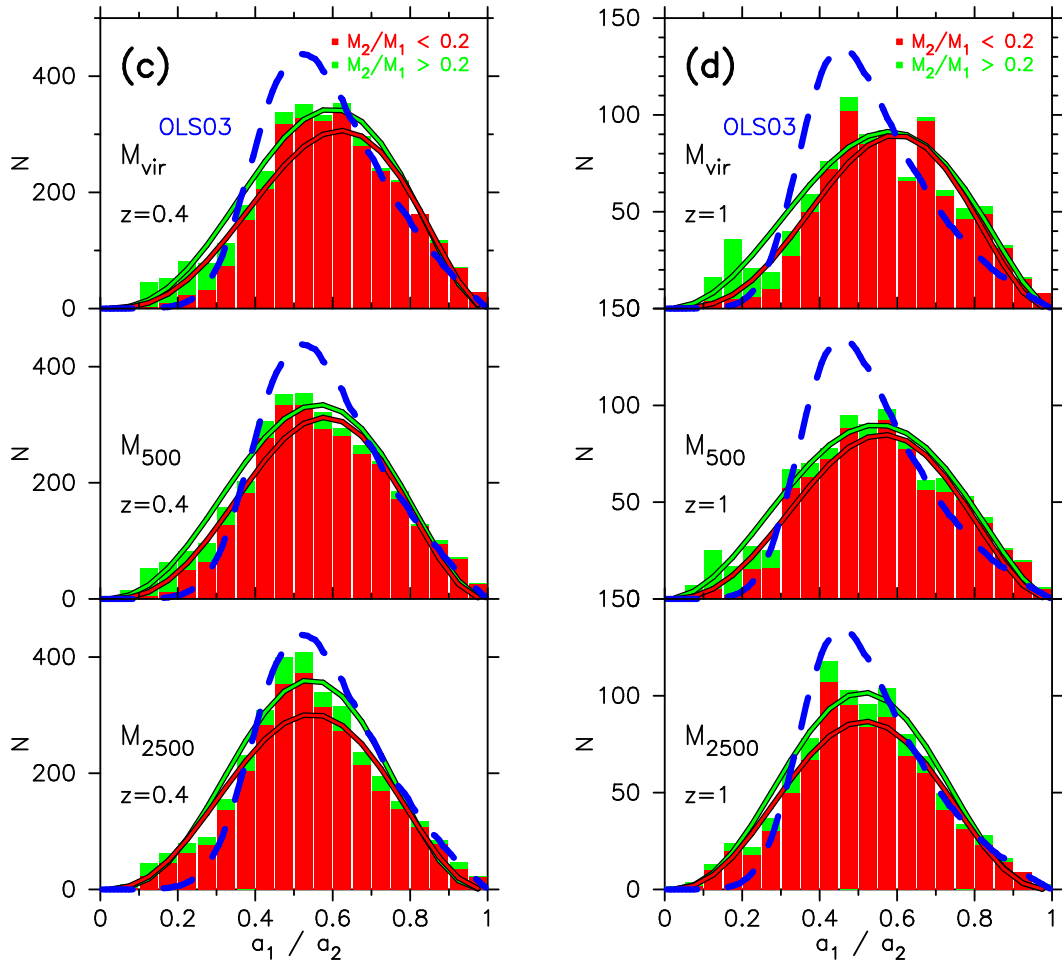
Figure 5.10: Continued.

According to Table 2, The mean value also has weak redshift dependence; it becomes smaller toward earlier redshifts. This is partly due to the fixed minimum mass for the sets of halos at different redshifts. At earlier redshifts, more massive fraction is chosen out of all the halos, so the mean axis ratio becomes smaller.

We have found that the values of mean and standard deviation of a_1/a_2 calculated directly from the simulation results agree within 5 % from those in Table 2. In addition, the dependence of the mean value on mass scale and redshift are the same as discussed above, implying the goodness of the fitting by the beta distribution.

In addition, the statistical mass dependence of a_1/a_2 is also weak. Figure 5.11 shows the axis ratio a_1/a_2 of each halo against its M_{vir} (left panel) and M_{500} (right panel). Except for the most massive part where the number of halos is small, the mass dependence of a_1/a_2 is even weaker than the three-dimensional axis ratio A_1/A_3 plotted in Figure 5.5. Therefore the minimum mass $M_{\mathrm{vir}} = 6.25 \times 10^{13} h^{-1} M_\odot$ set in the above analysis is not so critical. The weak dependence of the PDF of a_1/a_2 on redshift, mass scales (M_{vir}, M_{500}, M_{2500}) and the minimum mass of the halos are useful when the model is compared with observational data.

		all halos				single-halos only			
		a	b	mean	s.d.	a	b	mean	s.d.
$z = 0$	M_{vir}	4.18	2.71	0.61	0.17	5.00	2.99	0.63	0.16
$N = 2004 \times 3$	M_{500}	4.01	2.90	0.58	0.18	4.32	2.98	0.59	0.17
	M_{2500}	4.35	3.39	0.56	0.17	3.92	3.14	0.56	0.17
$z = 0.2$	M_{vir}	4.01	2.81	0.59	0.18	4.83	3.13	0.61	0.16
$N = 1550 \times 3$	M_{500}	3.69	2.92	0.56	0.18	4.18	3.13	0.57	0.17
	M_{2500}	4.34	3.65	0.54	0.17	4.46	3.74	0.54	0.16
$z = 0.4$	M_{vir}	4.02	3.03	0.57	0.17	4.78	3.34	0.59	0.16
$N = 1101 \times 3$	M_{500}	3.72	3.11	0.54	0.18	4.26	3.38	0.56	0.17
	M_{2500}	4.21	3.69	0.53	0.17	3.82	3.32	0.54	0.17
$z = 1$	M_{vir}	3.40	2.74	0.55	0.19	4.45	3.33	0.57	0.17
$N = 317 \times 3$	M_{500}	3.22	2.83	0.53	0.19	3.89	3.25	0.54	0.17
	M_{2500}	3.93	3.80	0.51	0.17	3.95	3.77	0.51	0.17

Table 5.2: List of the parameters of the beta distribution (5.9) that approximates the PDF of projected axis ratio for M_{vir}, M_{500} and M_{2500} for four redshifts. The mean $\mu = a/(a+b)$ and the standard deviation $\sigma = \sqrt{ab/[(a+b)^2(a+b+1)]}$ of the beta distribution are also shown.
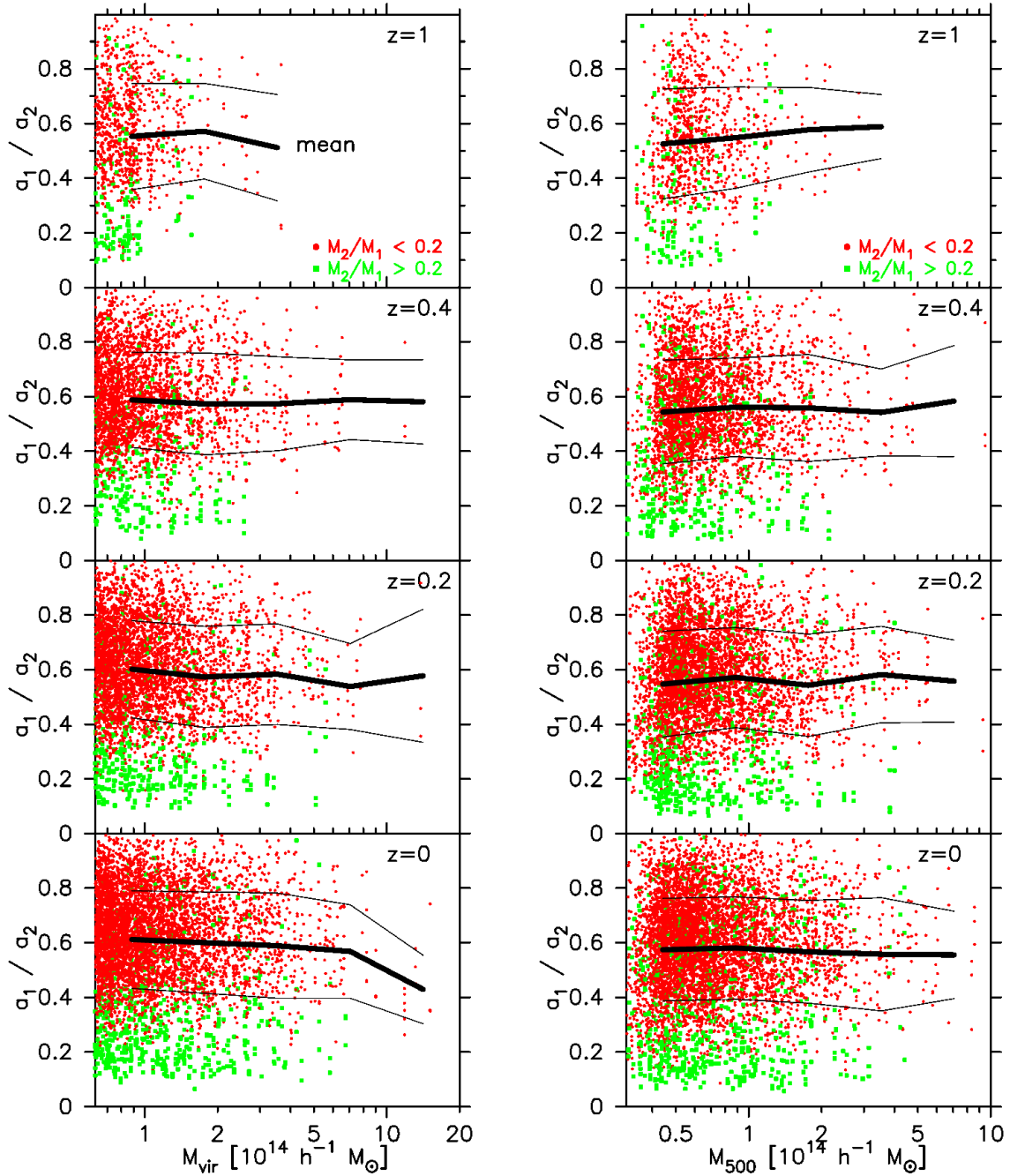
Figure 5.11: Projected axis ratio a_1/a_2 of each halo at the four different redshifts ($z = 1$, 0.4, 0.2, 0) against its M_{vir} (left) and M_{500} (right). Each symbol indicates the result for each of the 2004 simulated halos; red circle are single-halos ($M_2/M_1 < 0.2$), green squares are for multiple-halos ($M_2/M_1 > 0.2$). The thick and thin solid lines indicate the mean and the standard deviation, respectively. The halos are identified at each redshift, and their multiplicity (M_2/M_1) is also defined at each redshift. The number of the simulated halos is 3×2004 ($z = 0$), 3×1550 ($z = 0.4$), 3×1101 ($z = 0.2$), 3×317 ($z = 1$).

5.5.2 Comparison with observational sample

As an example of possible applications of our fitting formula for the PDF of projected axis ratio a_1/a_2, we attempt to compare it with the PDF for the observed halos estimated by Oguri et al. (2010). They measured the projected axis ratio from the weak lensing shear map of 18 clusters. In doing so, they assumed that the three-dimensional density distribution inside each halo follows a self-similar triaxial ellipsoid. The observed region of their clusters roughly corresponds to M_{500}, and their mean redshift is 0.23, so we compare their observation data with our model for M_{500} of all the halos and $z = 0.2$ in Table 2. The mean virial mass M_{vir} of our sample is roughly $2 \times 10^{14} h^{-1} M_{\odot}$.
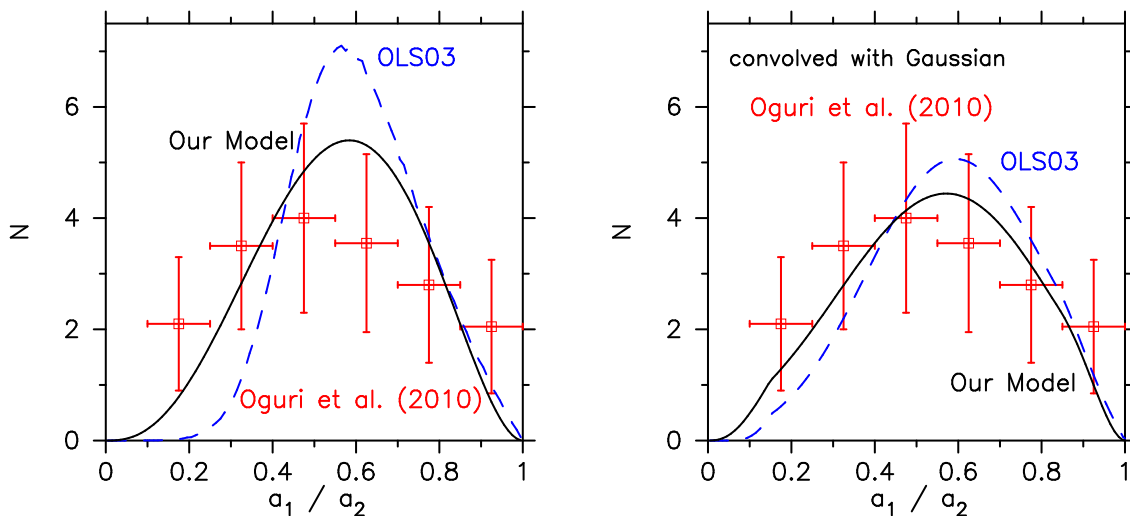

Figure 5.12: Comparison of PDFs of projected axis ratio a_1/a_2. The red symbols with error bars show the results from the 18 clusters in the weak lensing analysis by Oguri et al. (2010). The PDF of OLS03 is plotted in the blue dashed curve. Following Oguri et al. (2010), we use $M_{\mathrm{vir}} = 7 \times 10^{14} h^{-1} M_{\odot}$, corresponding to the mean mass of the observed clusters, when calculating the PDF of OLS03 through Equation (5.8). The black solid curve indicate our fitting formula for the PDF of a_1/a_2 at M_{500} of all the halos at $z = 0.2$ (Table 2). For the PDF of OLS03 and ours, the left panel illustrates the original PDFs, while the right panel shows those convolved with the Gaussian function, corresponding to the typical uncertainty for a_1/a_2 in the lensing analysis (cf. Table 1 of Oguri et al. (2010)).

The left panel of Figure 5.12 plots the PDF of projected axis ratio of the observed halos in red symbols with error bars. Oguri et al. (2010) compared this observational results with the PDF of OLS03 calculated by assuming $M_{\mathrm{vir}} = 7 \times 10^{14} h^{-1} M_{\odot}$ in Equation (5.8), corresponding to the mean mass of the observed clusters. We also plot the same PDF in the blue curve. In addition, our model is plotted in the black curve. The mean mass of our sample is smaller than that of Oguri et al. (2010), but this is not serious since the mass dependence of axis ratio a_1/a_2 is very weak (Figure 5.11).

In order to include the possible effect of the observational uncertainty in a_1/a_2, Oguri et al. (2010) convolved the PDF of OLS03 with the Gaussian function with $\sigma = 0.15$,

corresponding to the typical uncertainty of the measurement of the axis ratio (cf. Table 1 of Oguri et al. (2010)). The resulting PDF is shown in Figure 3.3 (Section 3.5). The PDF, however, has non-zero values at $a_1/a_2 = 0$ and 1, while the existence probability of halos with $a_1/a_2 = 0$ (line) and $a_1/a_2 = 1$ (perfect circle) should be zero. This comes from the constant $\sigma = 0.15$ for all a_1/a_2; e.g., for $a_1/a_2 = 0.95$, the range $0.8 \leq a_1/a_2 \leq 1.1$ is assumed, although a_1/a_2 should be less than unity.

We resolve the above problem in the following way. For $a_1/a_2 > 0.85$, we set $\sigma = 1 - a_1/a_2$, since the upper bound of a_1/a_2 is unity. Similarly, for $a_1/a_2 < 0.15$, we set $\sigma = a_1/a_2$ so that a_1/a_2 does not become negative. By using the above σ the depends on a_1/a_2, we convolve the PDF of OLS03 and our fitting formula with the Gaussian function with σ.

The resulting PDFs are plotted in the right panel of Figure 5.12. Because of the large observational error bars, it is difficult to distinguish the PDF of OLS03 and our fitting formula. Our fitting formula is, however, based on the direct measurement of a_1/a_2 of the simulated halos, and therefore more reliable than that of OLS03 based on the self-similarity of halos. In the near future, precise observational data of numerous clusters will be provided by the Subaru Hyper Suprime-Cam, for example.

5.6 Short Summary

In this chapter, we studied the non-sphericity of dark matter halos by analyzing halos extracted from the (dark matter only) simulation. In the first half of this chapter, we compared the evolution of the non-sphericity of halos with the prediction of the ellipsoidal collapse model (EC). In doing so, we assigned triaxial ellipsoids to approximate the density distribution of each simulated halo by using the mass tensor I (Equation (5.3)). The results are summarized as follows:

1. First, we compared the evolution of the axis lengths A_k ($k = 1, 2, 3$) of individual simulated halos with the EC prediction *on the object-wise basis*, at the mass scale of M_{FOF} (roughly corresponding to the virial mass M_{vir}). In general, the EC prediction roughly reproduces the simulation up to the turn-around epoch ($z \sim 1$). After the turn-around epoch, however, the simulation substantially deviates from the EC prediction.

2. The discrepancy in the *statistical* mass dependence of axis ratio A_1/A_3 at $z = 0$ between the EC prediction and simulations has been reported in literature; massive halos are more spherical in EC, but those in simulations tend to be less spherical. For the first time, we demonstrated how and when the statistical mass dependence of A_1/A_3 of the simulated halos deviates from EC. While massive halos are more spherical initially, they gradually become less spherical after the turn-around epoch. In contrast, more massive halos are always more spherical in the EC prediction. We also confirmed that the above mass dependence of axis ratio changes at earlier epochs in the inner regions by comparing the evolution of axis ratio at the mass scales M_{FOF}, $M_{\mathrm{FOF}}/2$ and $M_{\mathrm{FOF}}/10$.

3. The averaged axis ratio $\langle A_1/A_3 \rangle$ over all the simulated halos has significant radial dependence as a function of enclosed mass $M_{\mathrm{ellipsoid}}$ inside ellipsoids. At $M_{\mathrm{ellipsoid}} \gtrsim M_{\mathrm{FOF}}$, $\langle A_1/A_3 \rangle$ rapidly decreases due to filamentary structures around the halos. Inside $M_{\mathrm{ellipsoid}} \sim M_{\mathrm{FOF}}$, the radial dependence of $\langle A_1/A_3 \rangle$ gradually changes with time; while $\langle A_1/A_3 \rangle$ increases toward the inner region at $z = 1$, it decreases at $z = 0$. As a result, at $z = 0$, $\langle A_1/A_3 \rangle \sim 0.4$ at $M_{\mathrm{ellipsoid}} \sim 0.1 M_{\mathrm{FOF}}$ and $\langle A_1/A_3 \rangle \sim 0.5$ at $M_{\mathrm{ellipsoid}} \sim M_{\mathrm{FOF}}$. The radial dependence of $\langle A_1/A_3 \rangle$ indicates that the halos are not necessarily self-similar (concentric, common axis ratio and orientation).

The above results 1. and 2. imply that the information on the initial ellipticity of halos is largely lost after the turn-around epoch. Hence cosmological N-body simulations play important roles to study the *present* non-sphericity of halos. In the latter part of this chapter, we studied the probability distribution function (PDF) of A_1/A_3. Especially, we examined the validity of the self-similarity assumption for the density distribution of halos adopted by JS02, inspired by the above result 3.

4. We examined how the PDF of A_1/A_3 of halos at $z = 0$ depends on $M_{\mathrm{ellipsoid}}$. The values of $\langle A_1/A_3 \rangle$ at $M_{\mathrm{ellipsoid}} = M_{\mathrm{FOF}}/10$ is smaller than that of JS02 who employ the isodensity surface at $\rho = 2500\rho_{\mathrm{crit}}$ (roughly corresponding to the region of $M_{\mathrm{FOF}}/10$) and adopt the self-similarity assumption. The difference is partly due to the different methods of triaxial modelling of halos; mass tensor and isodensity surface. We also found that $\langle A_1/A_3 \rangle$ becomes larger toward outer mass scales; $\langle A_1/A_3 \rangle \sim 0.4$ at $M_{\mathrm{ellipsoid}} = M_{\mathrm{FOF}}/10$, and $\langle A_1/A_3 \rangle \sim 0.5$ at $M_{\mathrm{ellipsoid}} = M_{\mathrm{FOF}}$.

5. The projected axis ratio a_1/a_2 is a more relevant quantity to compare with observational data, and it is sensitive to the self-similarity assumption for the density distribution of halos. Therefore we calculated the PDF of a_1/a_2, not through those of three-dimensional A_1/A_3, but directly from the projected density distribution of the simulated halos for the first time. We found that the resulting PDFs have mean values $a_1/a_2 \sim 0.6$ only slightly depending on redshifts and mass scales ($M_{\mathrm{ellipsoid}} = M_{\mathrm{vir}}$, M_{500} and M_{2500}); halos seem rounder due to the projection effect.

6. We provided a universal fitting formula (in the form of the beta distribution) for the PDFs resulted from our simulation, and showed that the formula improves those in previous studies, including OLS03, that assume the self-similarity of halos. Hence our fitting formula will be useful in interpreting the future data of Subaru Hyper-Suprime Cam among others.

We used the dark matter only simulation in order to clarify how the non-sphericity of halos *intrinsically* evolves. The non-sphericity of actual halos can be, however, affected by baryons at least inner mass scales ($M_{\mathrm{ellipsoid}} \lesssim 0.5 M_{\mathrm{vir}}$). In the next chapter, we will study the effect of baryons on the non-sphericity of dark matter halos by using simulations with baryons (Section 6.4), although the main target of the next chapter is the non-sphericity of X-ray surface brightness from intracluster gas.

Chapter 6

Probing Non-sphericity of Galaxy Clusters through X-ray Surface Brightness

6.1   Motivation

In the previous chapter, we have constructed the probability distribution function (PDF) of projected axis ratio of dark matter density field, and compared it with the existing data of weak lensing observations. Given the limited number of the available observation data, our PDF of projected axis ratio is roughly consistent with the observation.

It is not clear, however, how faithfully the non-sphericity of the weak lensing shear map represents that measured by the mass tensor in the simulation. For more precise comparison, one should adopt the same estimator of non-sphericity both in simulations and observations. In the case of Oguri et al. (2010), weak lensing shear maps should be calculated directly from simulations. Oguri et al. (2010), however, assumes that their clusters have the self-similar density distribution in the three-dimensional space. Hence the analyses based on the fact that halos are actually not self-similar are not feasible at this stage.

Instead, in this chapter, we consider the non-sphericty of the X-ray surface brightness S_X of galaxy clusters:

$$S_X = \frac{1}{4\pi(1+z)^4} \int dl \quad n_{\mathrm{gas}}^2 \Lambda(T, Z) \tag{6.1}$$

where n_{gas} is the number density of gas and $\Lambda(T, Z)$ is the X-ray cooling function that depends on the gas temperature T and metallicity Z. Also, the integration is carried out along the line-of-sight. Note that, over the typical temperature range of galaxy clusters (1 keV $\lesssim T \lesssim$ 10 keV), Λ is approximately proportional to $T^{1/2}$, and therefore the shape of S_X is largely determined by the gas density.

Since the X-ray surface is one of the primary observables in X-ray observations of galaxy clusters, a number of data is available and will be increased in the near future. They are more easily estimated than weak lensing data that require precise measurements of distortion of many individual lensed galaxies. In fact, Kawahara (2010) has already measured the non-sphericity of the surface brightness of 70 galaxy clusters. While the

uncertainty is large, he obtained a barely consistent result with that expected from the PDF of Jing & Suto (2002) for dark matter.

It should be emphasized that the density distribution of gas is different from that of dark matter (Lee & Suto, 2003). Under the assumption of hydrostatic equilibrium (HSE), the gas mass density ρ_{gas} ($\propto n_{\mathrm{gas}}$) satisfies the following:

$$\frac{1}{\rho_{\mathrm{gas}}}\nabla p = -\nabla \phi, \qquad (6.2)$$

where p is the gas pressure, and ϕ is the gravitational potential mainly determined by the dark matter density distribution. When the gas is isothermal, $\nabla \log n_{\mathrm{gas}} \propto \nabla \phi$, and so the gas distributes along *isopotential* surfaces of dark matter, rather than *isodensity* surfaces. In general, isopotential surfaces tend to be rounder than isodensity surfaces, and therefore the gas density distribution is expected to be more spherical than that of underlying dark matter.

In addition, the conventional assumption of HSE is not so accurate (Lau et al., 2009, 2013; Fang et al., 2009; Suto et al., 2013) due to the dynamical motion of gas. Hence it is essential to use cosmological simulations including gas in order to precisely study the non-sphericity of gas density. In this chapter, we analyze 40 galaxy clusters extracted from cosmological simulations, and clarify the difference in the non-sphericity between gas and dark matter density. We further compare our simulation results with the observation data analyzed by Kawahara (2010).

6.2 Simulations

In this chapter, we analyze clusters extracted from cosmological hydrodynamical simulations performed by Dubois et al. (2014) with the adaptive mesh refinement code `RAMSES` (Teyssier, 2002).

The simulation includes 1024^3 dark matter particles in a periodic cube with a side length of 100 h^{-1} Mpc, where the cosmological parameters are set in accord with the Wilkinson Microwave Anisotropy Probe 7 cosmology (Komatsu et al., 2011); $\Omega_{m,0} = 0.272$, $\Omega_{\Lambda,0} = 0.728$, $\Omega_{b,0} = 0.045$, $\sigma_8 = 0.81$, $H_0 = 70.4$ km s^{-1} Mpc^{-1} and $n_s = 0.967$. Hence the dark matter mass resolution is $8 \times 10^7 M_\odot$. The initial condition is generated with the `MPGRAFIC` software (Prunet et al., 2008).

The size of gas cells is initially set to 136 kpc, and the size is refined if the number of dark matter particles in a cell becomes more than eight, or if the total baryonic mass in a cell is eight times the dark matter mass resolution ($8 \times 10^7 M_\odot$). The mesh refinement is carried out up to 7 times, and therefore the minimum cell size is 1.06 kpc. Star formation occurs if gas hydrogen number density exceeds the threshold of $n_0 = 0.1$ H cm^{-3} following a Poissonian random process (Rasera & Teyssier, 2006; Dubois & Teyssier, 2008).

The radiative cooling of gas due to H and He with a contribution from metals is modelled according to Sutherland & Dopita (1993). Heating from a uniform UV background also takes place following Haardt & Madau (1996). In addition, feedback from supernovae is taken into account; the frequency of Type Ia SN explosions follows Greggio & Renzini (1983), and the mechanical energy from Type II SNe is taken from `STARBURST99` (Leitherer et al., 1999, 2010).

	SIM-DM	SIM-SN	SIM-SA
	DM only	DM + baryons	DM + baryons
radiative cooling	No	Yes	Yes
SN feedback	No	Yes	Yes
AGN feedback	No	No	Yes

Table 6.1: The three simulations used in this chapter. Whether each of radiative cooling, supernova feedback, AGN feedback are included or not is indicated by "Yes" or "No".

Feedback from active galactic nuclei (AGN) is also modelled according to Dubois et al. (2012). Black holes are created where the gas mass density is larger than $\rho > \rho_0$ (ρ_0 is 0.1 times the hydrogen mass per cm^3) with an initial seed mass of $10^5 M_\odot$. The AGN feedback includes two different modes, according to $\chi = \dot{M}_{BH}/\dot{M}_{Edd}$, where the $\dot{M}_{BH}$ is the accretion rate onto the black hole and $\dot{M}_{Edd}$ is the Eddington accretion rate. If $\chi < 0.01$, the feedback is called "the radio mode", and the feedback energy is ejected into a bipolar outflow with a jet velocity of 10^4 km s^{-1} following Omma et al. (2004). Otherwise ($\chi > 0.01$), the feedback consists of isotropic injection of thermal energy into gas, called "the quasar mode". The energy deposition rate satisfies $\dot{E}_{AGN} = 0.015\dot{M}_{BH}c^2$; the coefficient is chosen so that the scaling relations between black hole mass and galaxy properties (mass, velocity dispersion) and black hole density in the local Universe (see Dubois et al., 2012) are reproduced.

For comparison, the simulation with the same settings as above but without the AGN feedback is run. In addition, the dark matter only simulation with the same initial conditions is also run. In this chapter, we refer to the hydrodynamical simulations with and without the AGN feedback as "SIM-SA" and "SIM-SN" for short. Also, the dark matter only simulation is called "SIM-DM". Table 6.1 summarizes the physical processes included in the three simulations.

We extract 40 clusters with $M_{200} > 3 \times 10^{13} M_\odot$ from SIM-SA. For each cluster, corresponding objects are identified in SIM-SN and SIM-DM as well. In the following sections, we analyze the non-sphericity of X-ray surface brightness of gas for the two sets of 40 clusters in SIM-SA and SIM-SN. For comparison, the non-sphericity of dark matter halos is calculated for the three sets of 40 clusters.

6.3 Importance of AGN Feedback: Density and Temperature Profiles

In general, the behavior of simulated clusters depends on baryonic processes included in simulations. Especially, the inclusion or exclusion of AGN feedback makes a significant difference. Since the X-ray surface brightness S_X is the key quantity in this chapter, we have to be careful of the difference in gas properties between SIM-SA and SIM-SN.

While we always show the analysis results for both simulations in parallel throughout this chapter, we consider that SIM-SA is the better model because it reproduces observed properties of clusters better than SIM-SN; we explain the reason for that in this section by looking at the density and temperature profiles of simulated clusters.

Figure 6.1 illustrates the density and temperature profiles of one simulated cluster ($M_{200} \approx 4.5 \times 10^{14} M_\odot$) in SIM-SN. In the left-panel, we plot the density profiles of gas (red), dark matter (black) and stars (blue). Also, the (mass-weighted) gas temperature profile is shown in the right panel.

The stellar density exceeds the dark matter density inside ~ 40 kpc. Since the typical radius of galaxies is roughly 10 kpc, the stellar density is rather high. This indicates that the radiative cooling is in the simulation too efficient. In fact, inside ~ 40 kpc, the gas temperature rapidly decreases toward the center. Due to the high concentration of stars, the gas density suddenly increases toward the center at around 40 kpc. Also, the dark matter density profile becomes slightly steeper around at 20 kpc.

In addition, outside ~ 40 kpc, temperature is much higher than the typical temperature of actual clusters expected from, for instance, the mass-temperature relation by Arnaud & Evrard (1999):

$$M_{200} = 1.5 \times 10^{15} \left(\frac{T_X}{10 \text{ keV}} \right)^{3/2}, \tag{6.3}$$

where T_X is the X-ray spectroscopic temperature. The cluster in Figure 6.1 has $M_{200} \approx 4.5 \times 10^{14} M_\odot$, and so the corresponding temperature is roughly 5 keV. Given that T_X is usually measured inside r_{500} ($\approx 0.5 r_{200}$), the gas temperature in SIM-SN is extraordinarily high. This is mainly due to the SN feedback from the excess amount of stars and the rapid accretion of gas toward the center. The above behavior of density and temperature profiles is not typical for actual clusters.

In contrast, the corresponding cluster in SIM-SA exhibits density and temperature profiles, consistent with observations (see Figure 6.2). The stellar density exceeds the dark matter density inside ~ 10 kpc, corresponding to the typical galactic scale. The gas density profile is flat inside ~ 100 kpc, and does not exhibit a rapid increase unlike in Figure 6.1. Also, the gas temperature gradually increases toward the center, and the temperature at around $r \lesssim 0.5 r_{200}$ is consistent with the mass-temperature relation (6.3).

Based on the results in this section, we use SIM-SA as a fiducial simulation, and show results for SIM-SN just for reference, in the rest of this chapter.

6.4 Non-sphericity of Dark matter and Stars

Before measuring the non-sphericity of the X-ray surface brightness of the simulated clusters, we examine how the non-sphericity of the dark matter density distribution, studied in the previous chapter, is affected by the inclusion of baryonic processes.

As in the previous chapter, we use the following mass tensor to estimate the non-sphericity of dark matter density distribution:

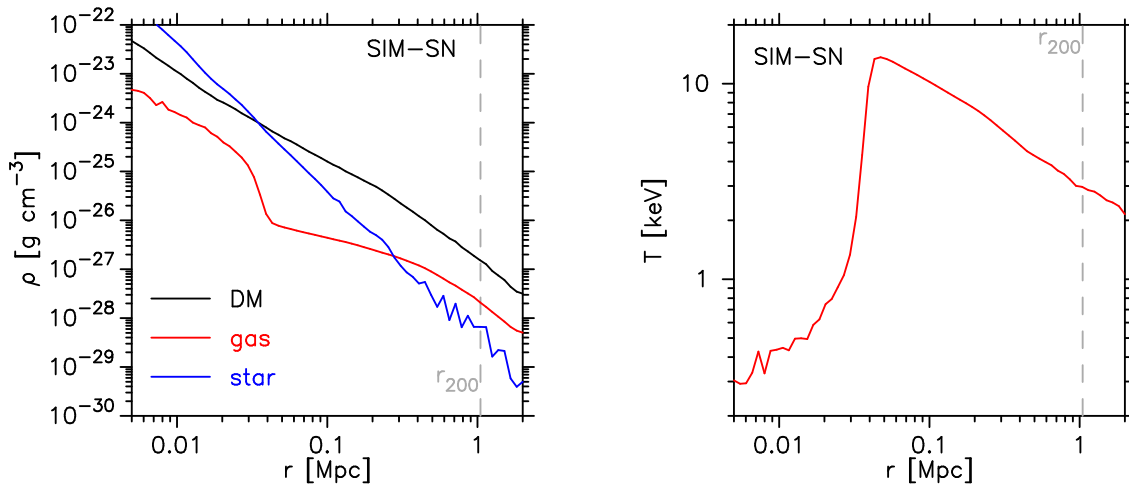$$I_{\alpha\beta} = \sum_i m^{(i)} x_\alpha^{(i)} x_\beta^{(i)}, \tag{6.4}$$

Figure 6.1: Radial profiles of density (left) and mass-weighted gas temperature (right) of the cluster with $M_{200} \sim 4.5 \times 10^{14} M_\odot$ for SIM-SN. The density profiles of gas (red), dark matter (black) and stars (blue) are shown in the left panel. The gray dashed vertical line indicates r_{200} of the cluster.
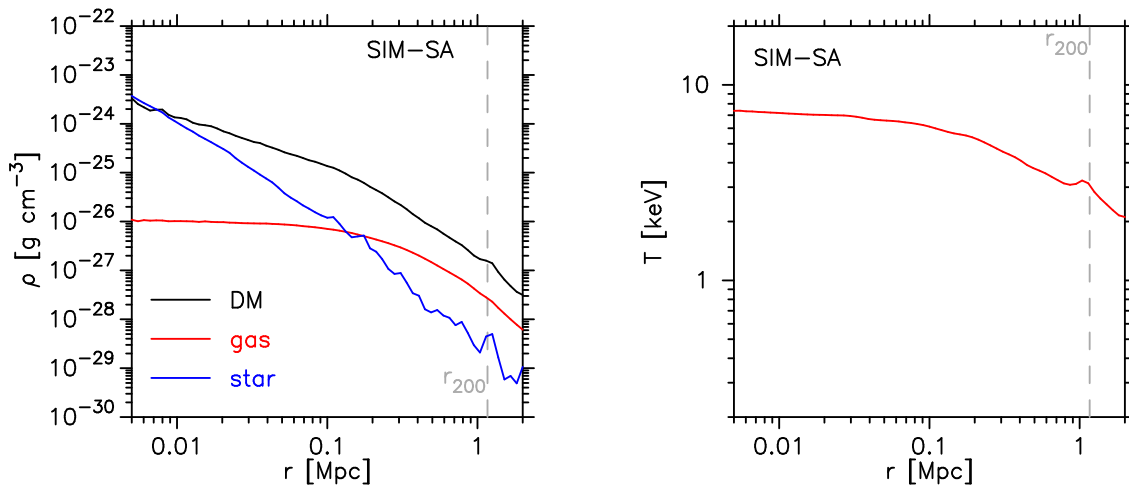

Figure 6.2: Same as Figure 6.1, but for the corresponding cluster in SIM-SA. Note that r_{200} is slightly different between SIM-SA and SIM-SN.

where $x_\alpha^{(i)}$ and $m^{(i)}$ is the position and mass of the i-th particle. The summation stops when the sum of $m^{(i)}$ reaches a given mass. We calculate the mass tensor iteratively in the same way as described in Section 5.2. For each of 40 simulated clusters, we calculate the projected dark matter density distribution along the x-, y- and z-axes. Then we identify the ellipses with the semi-major axis $a_2/r_{200} = 0.1, 0.2,..., 0.9, 1.0$. The same procedure is performed for the three simulations.

Figure 6.3 demonstrates the results for the same cluster in Figure 6.1. The resulting ellipses with the semi-major axis $a_2/r_{200} = 0.2, 0.4, 0.6, 0.8, 1.0$ are overplotted on the dark matter density distribution for each simulation; SIM-DM (upper-left), SIM-SN (upper-right) and SIM-SA (lower-left). The lower-right panel shows the dark matter density profiles in three simulations; SIM-DM (green), SIM-SN (magenta) and SIM-SA (black). Note that, since a part of the total mass of the universe is allocated to baryons in SIM-SN and SIM-SA, the dark matter mass in SIM-DM is larger than that in other simulations. Hence the density profile in SIM-DM is rescaled by $1 - \Omega_{b,0}/\Omega_{m,0} \approx 0.83$ in the figure.

The dark matter density distribution in SIM-SN is clearly rounder than the other two simulations for all the semi-major axes, while the ellipses in SIM-SA and SIM-DM look similar. Nevertheless, the spherically averaged density profiles are roughly the same outside $\sim 0.1r_{200}$; shapes of dark matter halos are different even though radial profiles are similar.

We note that, in general, dark matter density at the innermost region ($r < 0.1$ Mpc in this case) in both hydrodynamical simulations tends to be *larger* than that in SIM-DM, unlike Figure 6.3. This is because gas and stars fallen into in the central region pull dark matter towards the center. In fact, this tendency is noticeable in SIM-SN as in Figure 6.3. In SIM-SA, however, the individuality of clusters is more significant; whether the dark matter density in SIM-SA is larger or smaller than that in SIM-DM depends on individual halos.

In order to statistically see the difference of the resulting ellipses between the three simulations, we calculate PDFs of axis ratio $q = a_1/a_2$ for 40 clusters with three lines-of-sight. Figure 6.4 shows the results for the three simulations; SIM-DM (top), SIM-SN (middle) and SIM-SA (bottom). To compensate for the small number of clusters (120×3), we pile up the PDFs of $a_2 = 0.1$ - $0.4 \times r_{200}$ (left), 0.5 - $0.7 \times r_{200}$ (middle) and 0.8 - $1.0 \times r_{200}$ (right); the number of statistical samples is 480, 360 and 360, respectively. This procedure is justified by the weak radial dependence of q at least for SIM-DM (cf. Section 5.5).

At the scale of 0.1 - $0.4 \times r_{200}$, the PDF of SIM-DM (top) is basically consistent with the result for M_{2500} in Section 5.5 ($r_{2500} \approx 0.2r_{200}$), although the number of dark matter halos in this chapter is much smaller. The PDF of SIM-SN (middle) is shifted to the right, relative to that of SIM-DM; the dark matter density distribution is significantly rounder. In contrast, if the AGN feedback is included (bottom), the density distribution is only slightly rounder than that of SIM-DM.

One may expect that the rounder density distribution in SIM-SN may be related to the radial density profile concentrated in the central region. Then the difference in q should appear only in the inner region of cluster ($\lesssim 0.5r_{200}$) where the existence or absence of AGN significanly affects the density profile. However, the similar difference in PDFs between the three simulations still persists in outer regions, even up to the scale of r_{200},

as shown in the middle and right panels of Figure 6.4. This is surprising given that the
spherically-averaged density profile is roughly the same between the three simulations,
and that the dark matter occupies a much larger mass fraction (≈ 80 %) than gas and
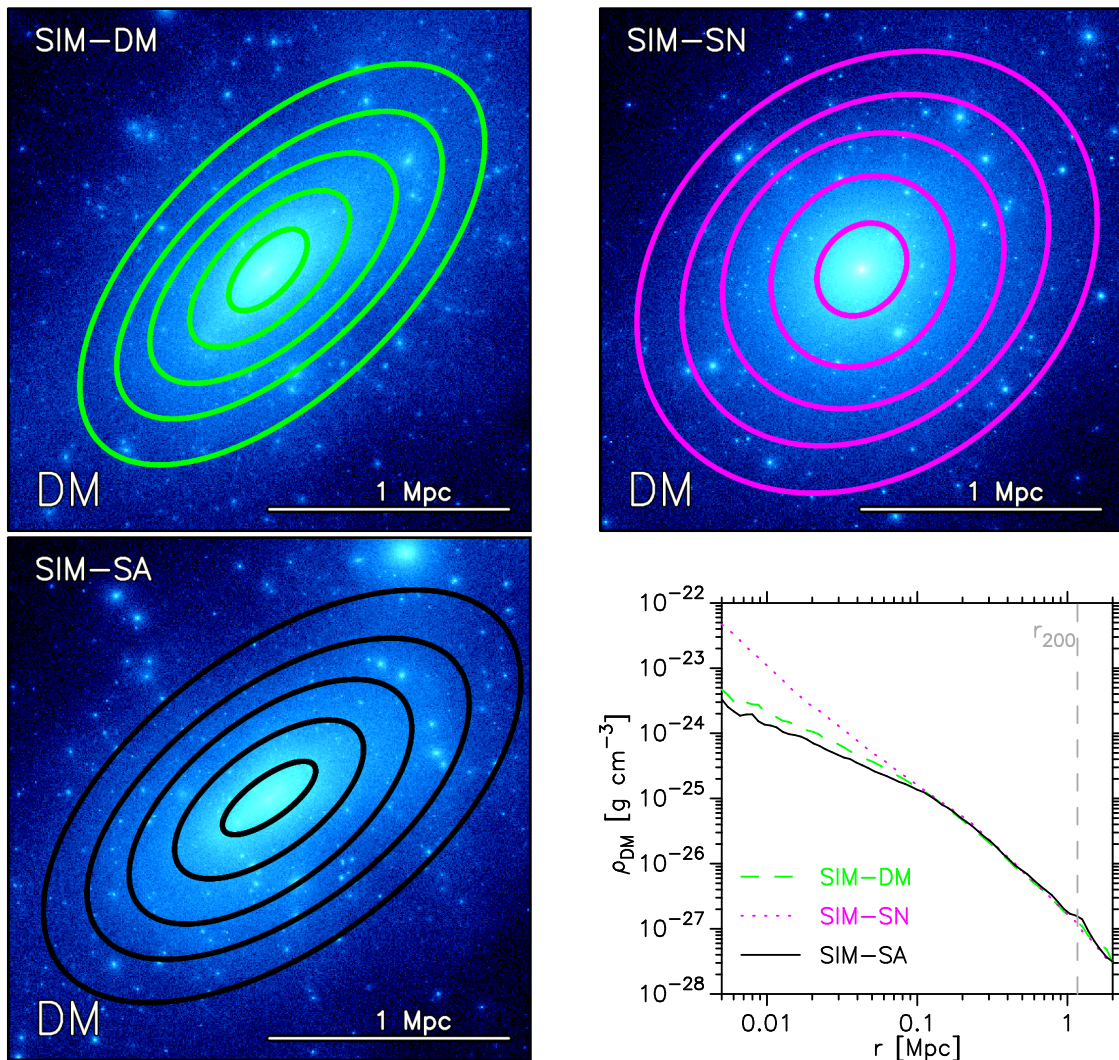stars.

Figure 6.3: Dark matter density distribution of the same cluster in Figure 6.1 projected
along the z-axis of the simulation for three simulations; SIM-DM (upper-left), SIM-
SN (upper-right) and SIM-SA (lower-left). The fitted ellipses with the semi-major axis
$a_2/r_{200} = 0.2, 0.4, 0.6, 0.8, 1.0$ are plotted in black curves. The corresponding dark matter
density profiles are shown in the lower-right panel; SIM-DM (green), SIM-SN (magenta)
and SIM-SA (black). The dashed vertical line indicates r_{200} in SIM-SA. For SIM-DM, the
density profile is multiplied by a factor of $1 - \Omega_{b,0}/\Omega_{m,0} \approx 0.83$.

Previously, Kazantzidis et al. (2004) showed that dark matter halos in a simulation
without radiative gas cooling is much less spherical than those in a simulation with cooling
(both simulations do not include AGN feedback) up to the virial radius ($\approx r_{200}$). This

result also indicates that the shape of dark matter halos strongly depends on the baryonic processes included in simulations. (Note that, since they adopted another definition of mass tensor, their results should not be quantitatively compared with ours.)

The above results indicate that the baryonic processes need to be carefully treated in cosmological simulations even when the non-sphericity of dark matter (not gas or stars) is studied. Simulation techniques for modelling baryonic processes are, however, still developing, and this problem becomes more difficult for higher resolution simulations. This remains a challenge for future.
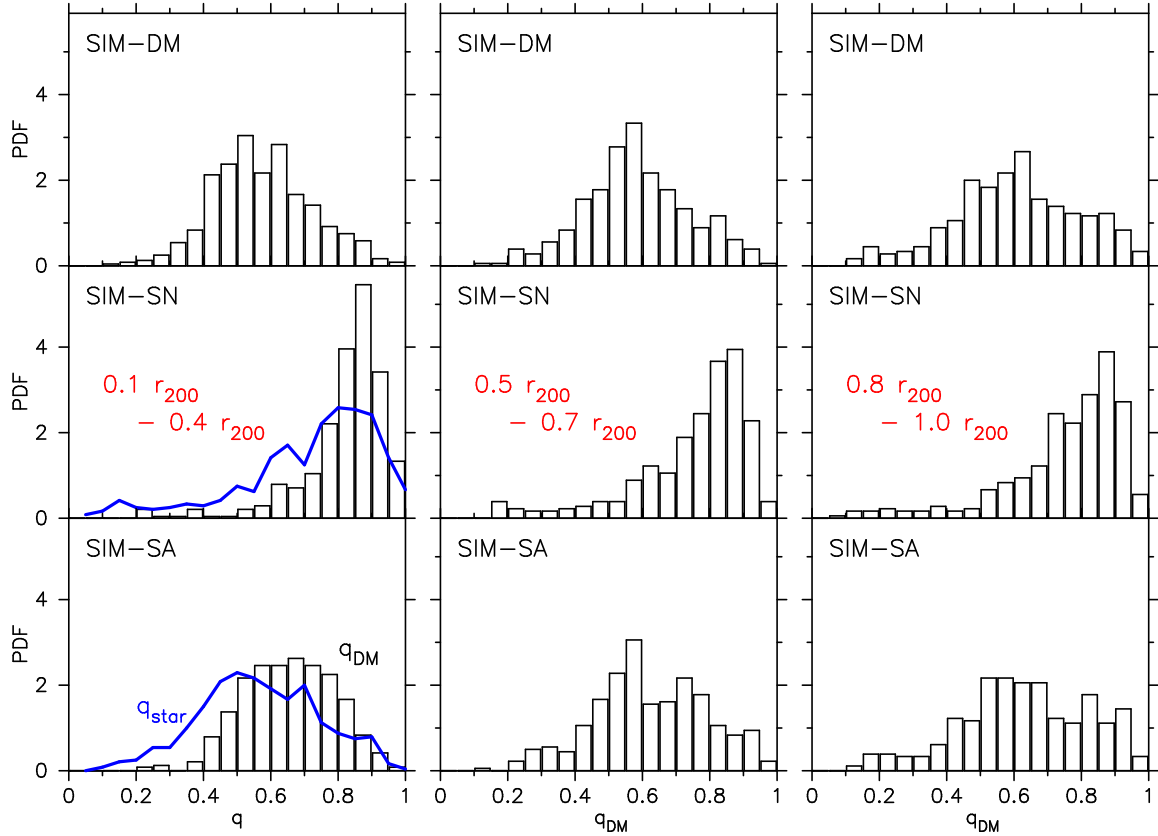
Figure 6.4: PDFs of projected axis ratio of dark matter density distribution for the 40 simulated cluster along three lines-of-sight (x-, y- and z-axes of the simulation). For each cluster, ellipses with the semi-major axis $a_2/r_{200} = 0.1, 0.2,..., 0.9, 1.0$ are obtained by the mass tensor $I = \sum xx$, and the PDF is calculated for the ellipses with 0.1 - 0.4 r_{200} (left), the ellipses with $a_2 = 0.1 - 0.4$ r_{200} (left), 0.5 - 0.7 r_{200} (middle) and 0.8 - 1.0 r_{200} (right). The same analysis is performed for the three kinds of simulations; SIM-DM (top), SIM-SA (middle) and SIM-SN (bottom). For SIM-SA and SIM-SN, the PDF of axis ratio of stellar density distribution for $a_2/r_{200} = 0.1, 0.2, 0.3, 0.4$ is shown in the blue curve.

The non-sphericity of stellar density distribution can be estimated also through the mass tensor similarly. The PDF of the axis ratio q of the ellipses with the semi-major axis $a_2/r_{200} = 0.1, 0.2, 0.3, 0.4$ for SIM-SN and SIM-SA (right) are illustrated in the middle-left and bottom-left panels of Figure 6.4, respectively. For both simulations, the

PDF of q for stars is slightly shifted to the left (less spherical) compared to that of dark matter in each simulation. This is partly because the mass tensor $I = \sum xx$ is sensitive to substructures, i.e., galaxies at large radii. The PDF in SIM-SN is shifted to the right, compared to that in SIM-SA, similarly to the case of dark matter.
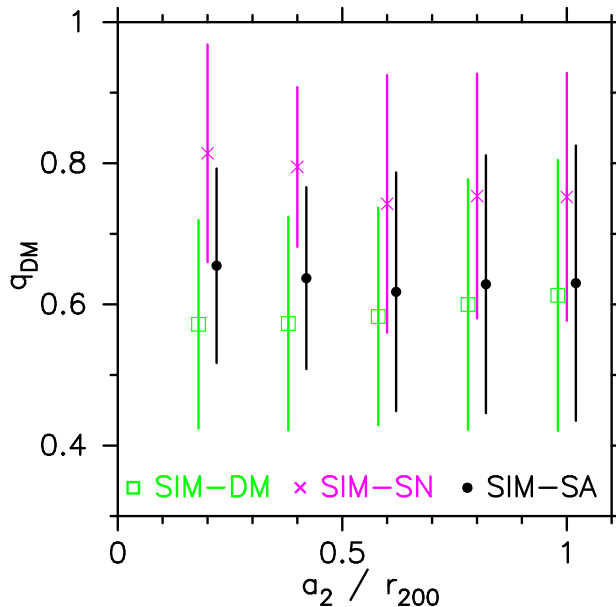

Figure 6.5: Radial dependence of axis ratio q of dark matter for the three simulations; SIM-DM (green squares), SIM-SN (magenta crosses), SIM-SA (black circles). The ellipses with $a_2/r_{200} = 0.1$, 0.2, 0.4, 0.6, 0.8, 1.0 are found for the projected density distribution of each dark matter halo by using the mass tensor. The lines indicate the standard deviations.

In addition, we demonstrate the radial dependence of q of dark matter for the three simulations in Figure 6.5. The figure shows q of the ellipses with $a_2/r_{200} = 0.1$, 0.2, 0.4, 0.6, 0.8, 1.0. In SIM-SN, halos have mean values $\langle q \rangle \sim 0.6$ with a weak radial dependence. This is consistent with the results in Section 5.5 based on another dark matter only simulation. As already seen in Figure 6.4, halos in SIM-SN are significantly rounder than those in the other simulations at all the scales up to the virial radius.

In contrast, $\langle q \rangle$ in SIM-SA is comparable to that in SIM-DM at least at around $a_2 = r_{200}$. Hence the results in Chapter 5 for the scales around the virial mass (comparison between the simulation results and the ellipsoidal collapse model, PDFs of axis ratio, etc.) will be little affected by baryons. At smaller mass scales ($\lesssim 0.5 M_{\rm vir}$), however, $\langle q \rangle$ in SIM-SA is larger than that in SIM-DM, i.e., the non-sphericity of halos will be significantly affected by baryons. This implies simulations with baryons are needed to precisely examine the non-sphericity of actual dark matter halos, while we clarified the intrinsic (under no baryon effects) evolution of the non-sphericity in Chapter 5.

6.5 Non-sphericity of X-ray Surface Brightness

6.5.1 Fitting Ellipses to X-ray Surface Brightness

We now measure the non-sphericity of the X-ray surface brightness S_X. For each cluster, we calculate S_X according to Equation (6.1) along the x-, y- and z axes. The range to be projected along the line-of-sight is chosen as $[-r_{200},\ r_{200}]$. We use the package SPEX to calculate the cooling function $\Lambda(\Lambda, Z)$. Then we directly fit ellipses to the X-ray surface brightness S_X. We adopt the fitting procedure of Jedrzejewski (1987), as done by Kawahara (2010). For each simulated cluster, we identify the ellipses with semi-major axis a_2 fixed to $a_2/r_{200} = 0.1$, 0.2, 0.3 and 0.4. Then the number of free parameters in the fitting procedure is four; the axis ratio a_1/a_2, direction of the major axis Θ and the central position $\boldsymbol{X}_c$.

The top-panels of Figure 6.6 shows the results of the fitting to S_X for the same cluster in Figure 6.1 for SIM-SN (left) and SIM-SA (right). The black curves illustrate the ellipses with the semi-major axis $a_2/r_{200} = 0.1$, 0.2, 0.3, 0.4. For comparison, the density distributions of dark matter and stars are shown in the middle and bottom panels.

The same color represents the same value of S_X both in the left and right panels. Hence the gas is more concentrated in SIM-SN. This is due to the high stellar density, as seen in the density profiles in Figure 6.1.

In SIM-SA, S_X is rounder than the dark matter density distribution, as expected from the HSE assumption. In addition, while the orientations of the ellipses for S_X are similar to those of dark matter, they are not concentric. In SIM-SN, on the other hand, S_X is as round as the dark matter density distribution. In the next subsection, we statistically examine the non-sphericity of S_X.

6.5.2 Mass- and Radial-Dependence of Axis Ratio

We examine the statistical dependence of axis ratio q of the X-ray surface brightness S_X on mass and radius, as done in Section 5.5 for q of dark matter density distribution. We have found that q of dark matter is very weakly dependent both on mass and radius. Hence it is expected that q of S_X also has weak dependence on mass and radius.

Figure 6.7 plots q of S_X at $a_2 = 0.4r_{200}$ for each simulated cluster along three lines-of-sight against its M_{200} for SIM-SA (left) and SIM-SN (right). The figure indicates the mass dependence of q is very weak both in SIM-SN and SIM-SA, while the scatter of q is large. For each cluster, the measured q along the x-, y-, and z-axis are plotted in the red squares, green triangles and blue squares, respectively. Even for the same cluster, q can be quite different depending on the lines-of-sight; for example, if a cluster is elongated along the z-axis, q along x- or y-axis is much smaller than that along the z-axis.

We divide the 40 clusters into four groups of 10 clusters in the decreasing order of mass. The mean value of q and the standard deviation are indicated by the black circle and line in Figure 6.7. The mean q in SIM-SN (~ 0.84) is slightly larger then that in SIM-SA ~ 0.78. This reflects the rounder shapes of the dark matter halos in SIM-SN, but the difference of q for S_X between the two simulations is smaller than that of dark matter.
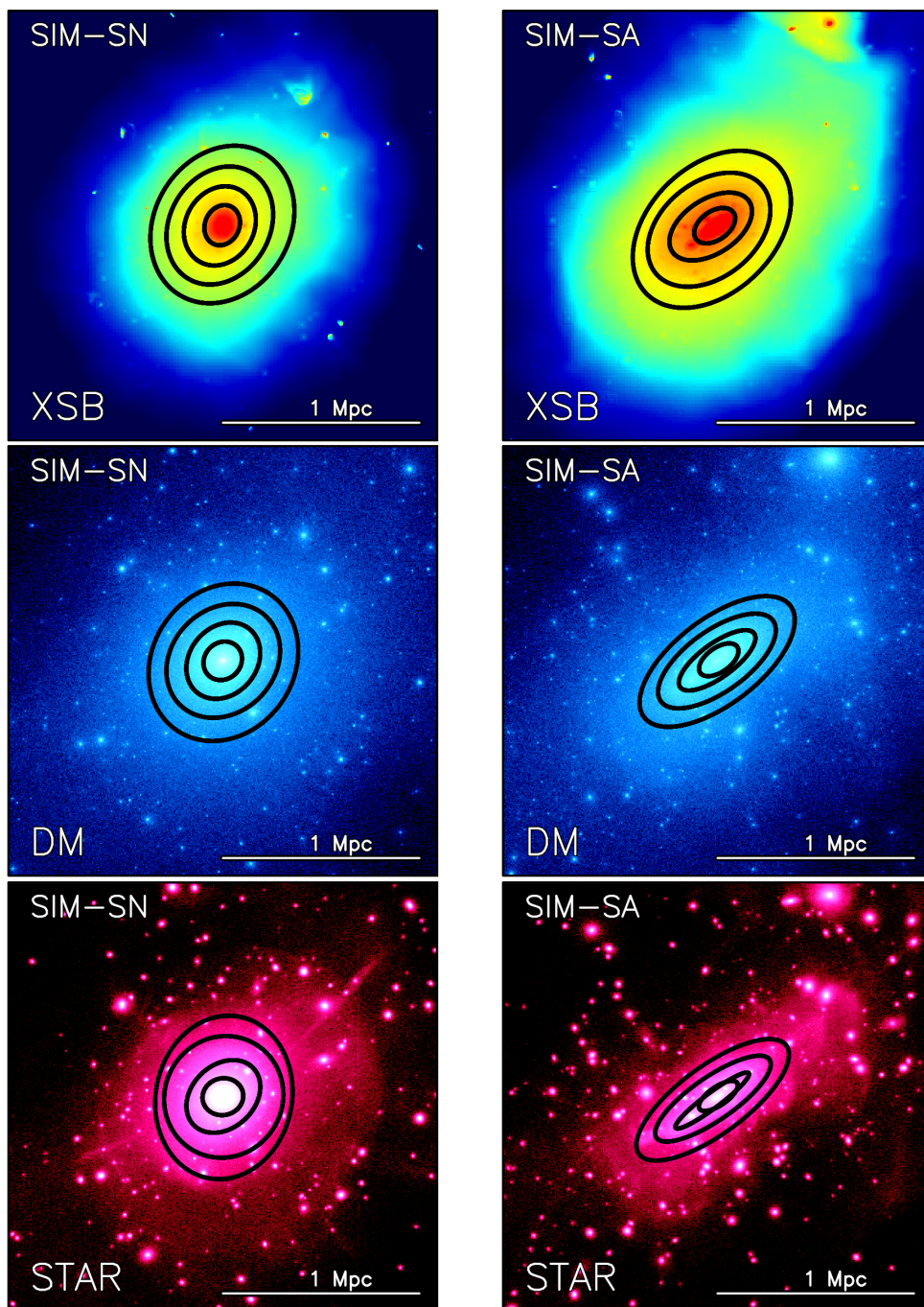
Figure 6.6: X-ray surface brightness S_X (top), dark matter density distribution (middle) and stellar density distribution (bottom) of the same cluster in Figure 6.1 along the z-axis, for SIM-SN (left) and SIM-SA (right). For each panel, the ellipses with the semi-major axis $a_2/r_{200} = 0.1, 0.2, 0.3, 0.4$ are plotted in black curves. The ellipses are obtained by direct fitting for S_x, and by mass tensor $I = \sum xx$ for dark matter and stars.

While Figure 6.7 shows the results for the semi-major axis $a_2 = 0.4 \times r_{200}$, basically the same results are reproduced even for $a_2 = 0.1, 0.2, 0.3 \times r_{200}$. In fact, the weak radial

dependence of q is demonstrated in Figure 6.8. The figure plots the q of S_X (red circles) averaged over all the simulated clusters with the standard deviation indicated by the red line, for SIM-SN (left) and SIM-SA (right). The mean q of S_X is roughly 0.8 at all the radii for both simulations. In SIM-SN, while the scatter is large, the mean value of q becomes slightly larger toward outer regions. This is partly because gas is more concentrated in SIM-SN (see Figure 6.6); contours of S_X with $a_2 \gtrsim 0.3r_{200}$ tend to be more spherical compared to those in SIM-SA.

The mean value of q for dark matter is plotted in the black squares. In SIM-SA, dark matter halos have a smaller mean value of q than S_X, while they are as round as S_X in SIM-SN. This has been already seen for the particular cluster in Figure 6.6.

The blue triangles in Figure 6.8 indicate that the density distribution of stars is less spherical than that of dark matter for both simulations. Also, the mean q of stars is higher in SIM-SN, as in the case of dark matter. The mean q of stars tends to be larger toward the center for both simulations. This is partly because there are more galaxies at outer regions that makes the ellipses determined by the mass tensor $I = \sum xx$ less spherical.

In the innermost region ($a_2 = 0.1r_{200}$) in SIM-SN, dark matter is more spherical than S_X, inconsistent with expectation from the HSE assumption. One might expect that, at this region, stars significantly contribute to the gravitational potential. We have confirmed, however, that q measured for the mixed density distribution of dark matter and stars is roughly the same as q for dark matter alone. Hence Figure 6.8 implies that, in SIM-SN, the gas is far from the hydrostatic equilibrium in the innermost region.

6.5.3 PDF of Axis Ratio

We finally calculate the PDF of axis ratio q of the X-ray surface brightness S_X and compare it with the data analyzed by Kawahara (2010). Since we have seen that q is almost independent of radius and mass in the previous subsection, we combine the results for all the four semi-major axis lengths $a_2 = 0.1, 0.2, 0.3, 0.4 \times r_{200}$ to calculate a single PDF. Hence the number of statistical sample is 480 (40 halos $\times$ 3 lines-of-sight $\times$ 4 semi-major axis lengths) for each simulation.

Figure 6.9 shows the results; the histogram is the PDF of q for the simulated clusters. The observation data analyzed by Kawahara (2010) are indicated by the cross symbols. For comparison, the PDF of q of dark matter is overplotted in green dashed line. The PDF for S_X is clearly different from that for dark matter at least in SIM-SA, as qualitatively expected from the HSE assumption.

We also plot in black solid curve the PDF of q for isopotential surfaces based on the PDF of JS02 for axis ratio of self-similar triaxial ellipsoids and the HSE assumption. Strictly speaking, this is the PDF expected for the *projected gas density distribution*, not for S_X, under the HSE assumption. As shown in the magenta dotted line in Figure 6.9, however, the PDF of q for the projected gas density directly calculated from the simulation is roughly the same as the PDF for S_X; while the projected gas density is proportional to n_{gas} and S_X is proportional to n_{gas}^2, their shapes are roughly the same. Therefore, the difference between the black solid curve and the red histogram is due to the projection effect (invalidity of the self-similar assumption in JS02) and the departure from the HSE
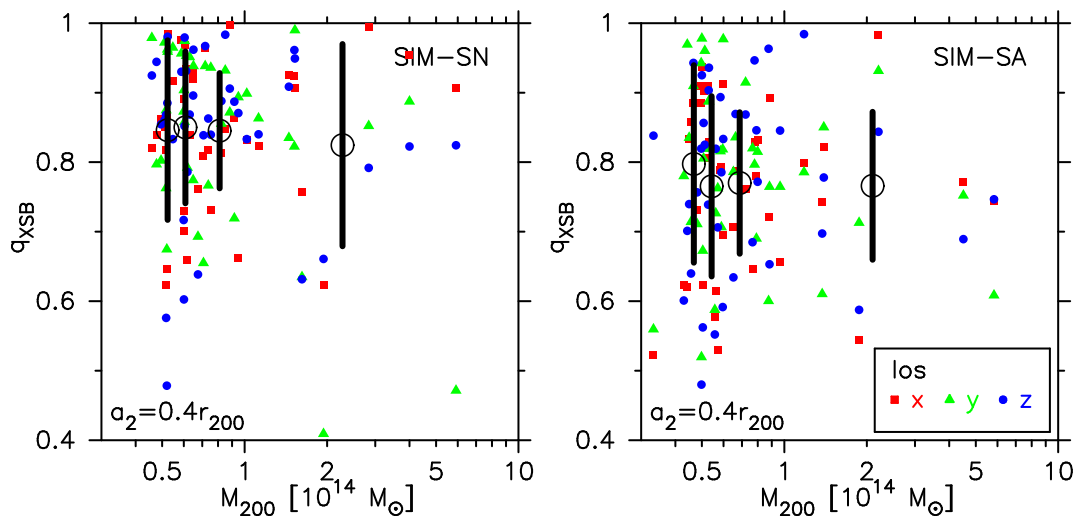
Figure 6.7: Projected axis ratio q of the X-ray surface brightness with $a_2 = 0.4r_{200}$, against M_{200} of each simulated cluster, for SIM-SN (left) and SIM-SA (right). Each symbol indicates the result for a simulated cluster. The axis ratio q of each cluster is measured along the three different lines-of-sight, and indicated in different symbols; x-axis (red square), y-axis (green triangle), z-axis (blue circle). The black circles show the averaged values of q over every 10 of 40 clusters, and the black lines indicate the corresponding standard deviation.
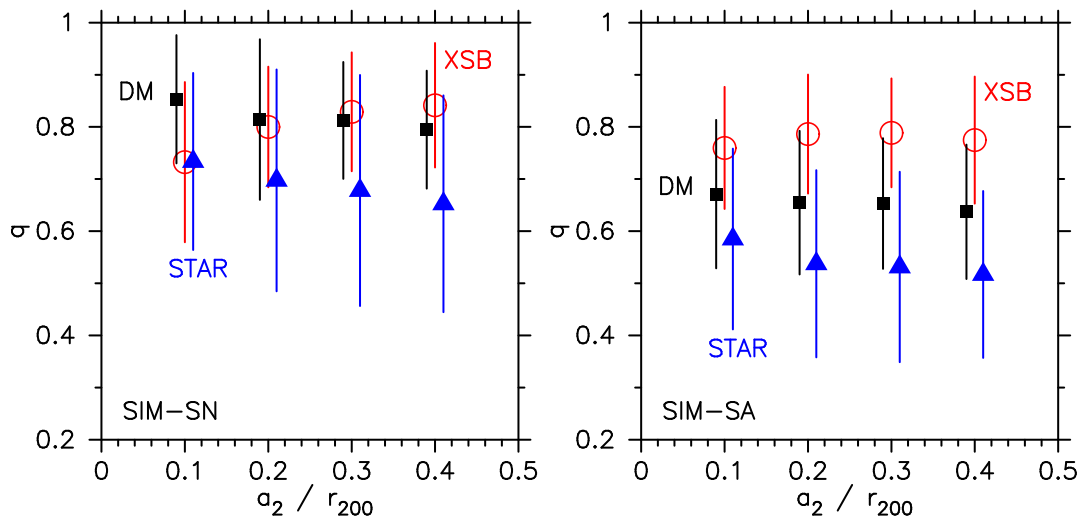

Figure 6.8: Projected axis ratio q of the X-ray surface brightness (red), dark matter (black) and stars (blue) for the semi-major axis $a_2/r_{200} = 0.1, 0.2, 0.3, 0.4$, averaged over the 40×3 clusters, for SIM-SN (left) and SIM-SA (right). The lines indicate the standard deviation. To facilitate visualization, the results for dark matter and stars are slightly shifted to the left and right, respectively.
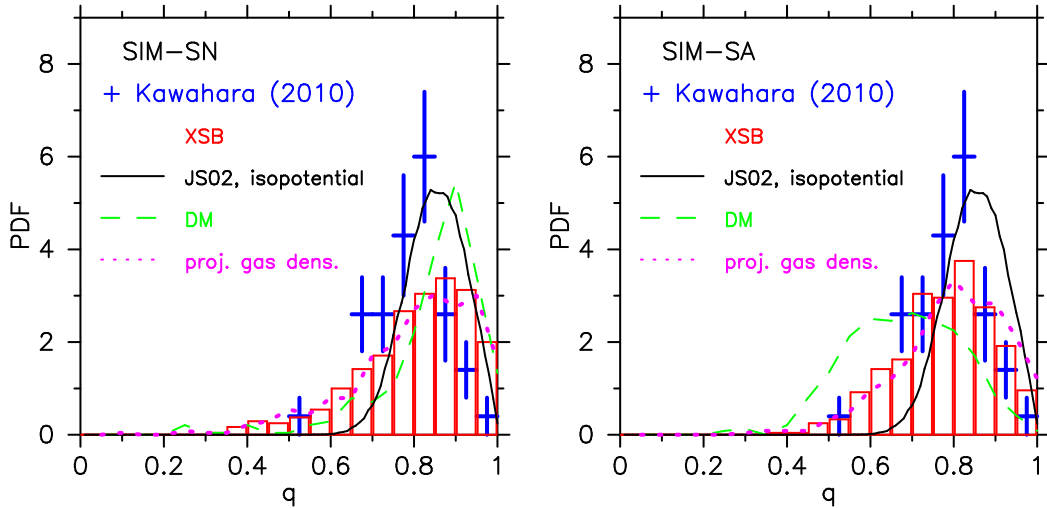
Figure 6.9: PDFs of projected axis ratio q of the X-ray surface brightness S_X (histogram), dark matter (green dashed line), the isopotential surfaces based on JS02 and the HSE assumption (black solid line), the projected gas density distribution (magenta dotted line) and the observational data analyzed by Kawahara (2010) (blue symbols), for SIM-SN (left) and SIM-SA (right).

assumption.

We emphasize that our simulation results (red histogram) and the PDF for the isopotential surfaces (black curve) are totally different. This indicates that the simple model prediction (black curve) based on the PDF of JS02 and HSE assumption is inappropriate for precise comparisons with observation data; it is necessary to calculate the observable quantities directly from simulation data.

Kawahara (2010) derived the PDF of q from the observation data, and compared it with the PDF for isopotential surfaces (black dashed curve) and concluded that they are barely consistent. Since we have obtained the more reliable prediction (red histogram) for the PDF of q, the consistency between the observation data and the simulation results can be more strictly tested. Here we apply the Kolmogorov-Smirnov (KS) test, which is free from the binning of data.

In general, for a PDF $F_n(x)$ with n samples for x and a null hypothesis that "$F_n(x)$ is generated from the smoothed distribution $F(x)$", the KS statistic D_n is defined by

$$D_n = \sup_x |F(x) - F_n(x)|. \tag{6.5}$$

Then the quantity $\sqrt{n}D_n$ has the following PDF independently of $F(x)$ and $F_n(x)$:

$$p(\sqrt{n}D_n \leq x) = 1 - 2\sum_{i=1}^{\infty}(-1)^{i-1}e^{-2i^2x^2}. \tag{6.6}$$

In addition, for a confidence level α, K_α is defined by $p(\sqrt{n}D_n \leq K_\alpha) = 1 - \alpha$. Then, if $\sqrt{n}D_n > K_\alpha$, the null hypothesis is rejected for the confidence level α.

We regard the observation data analyzed by Kawahara (2010) and the PDF of q for the isopotential surfaces as $F(x)$ and $F_n(x)$, respectively ($x = q$ and $n = 169$). Figure 6.10 shows the cumulative PDFs of the observation data (thin blue solid) and the PDF of q for the isopotential surfaces (black dashed). Note that the blue and black curves are the same for both panels. For these cumulative PDFs, we obtain $\sqrt{n}D_n = 3.89$, and the corresponding α is less than 10^{-7}. Hence the PDF of q for the isopotential surfaces is inconsistent with the observation data.

In Chapter 5, we convolved the PDF derived from the simulation with a Gaussian with $\sigma \sim 0.15$, corresponding to the typical uncertainty in estimates of axis ratio, as done by Oguri et al. (2010). Here we do not perform a similar procedure, since the typical uncertainty in determination of q of S_X in Kawahara (2010) is order of 0.01; PDFs little change after convolved with a Gaussian.

We next compare the observation data with our simulation results. The KS test can be modified for the two sets of discrete PDFs. For cumulative PDFs $F_n(x)$ and $G_m(x)$ with n and m samples, respectively, the KS statistic $\bar{D}_{n,m}$ is defined by

$$\bar{D}_{n,m} = \sup_x |F_n(x) - G_m(x)|. \tag{6.7}$$

Then the quantity $\sqrt{nm/(n+m)}\bar{D}_{n,m}$ follows the same PDF as Equation (6.6).
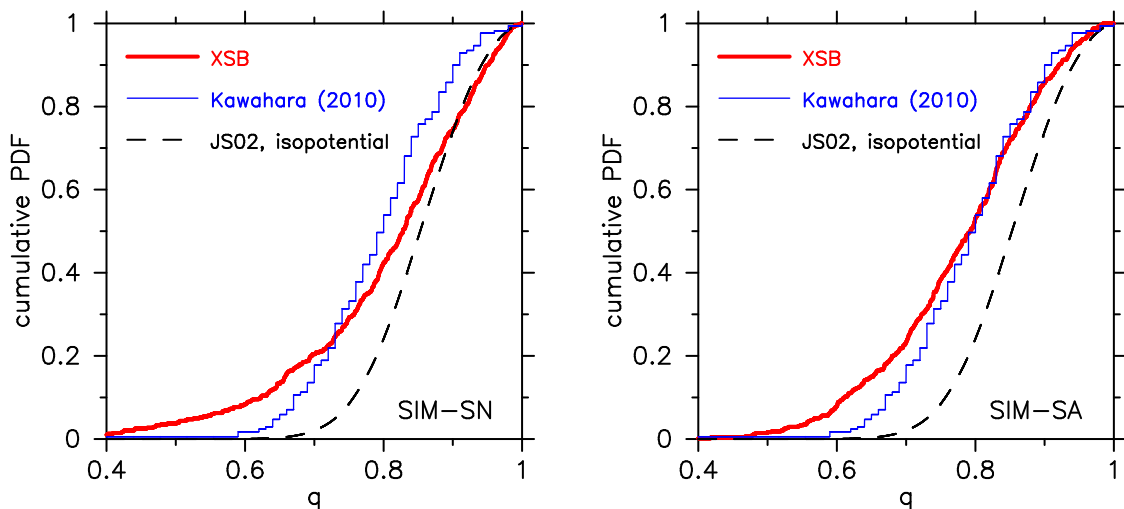

Figure 6.10: Cumulative PDFs of q of the X-ray surface brightness S_X (red thick), the isopotential surfaces based on JS02 and the HSE assumption (black dashed) and the observational data analyzed by Kawahara (2010) (blue thin) for SIM-SN (left) and SIM-SA (right).

We regard the histogram of q for S_X of our simulated clusters as $G_m(x)$ ($x = q$ and $m = 480$). The cumulative fraction for q of S_X is shown in thick red line in Figure 6.10 for SIM-SN (left) and SIM-SA. For SIM-SN, we obtain $\sqrt{nm/(n+m)}\bar{D}_{n,m} = 2.04$, and the correponding α is less than 10^{-3}. On the other hand, for SIM-SA, $\sqrt{nm/(n+m)}\bar{D}_{n,m} =$

1.24, and the corresponding α is 0.10. In other words, the probability that the observational data statistically agrees with our simulation results is 10 % for SIM-SA, and less than 0.1 % for SIM-SN.
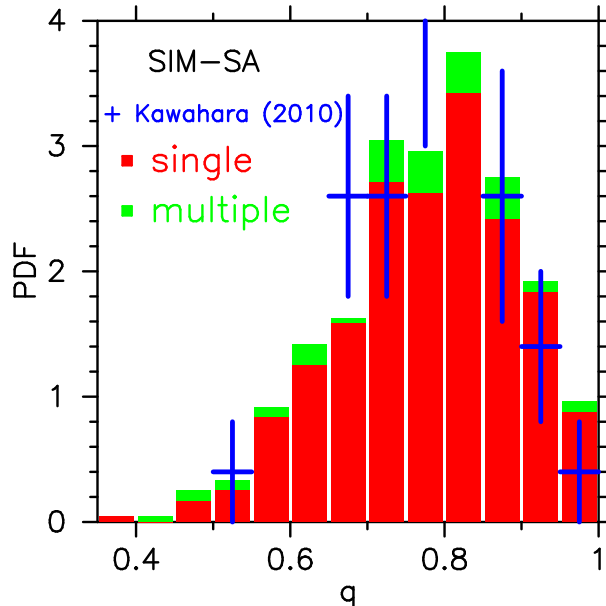

Figure 6.11: PDF of axis ratio q of the X-ray surface brightness S_X for SIM-SA, colored to indicate the contributions from single-halos (red) and multiple-halos (green). For comparison, the observation data analyzed by Kawahara (2010) are plotted in blue symbols.

As a result, our simulation results for SIM-SA (red curve in the right panel of 6.10) better agrees with the results of Kawahara (2010) (blue curve), compared to the prediction based on the PDF of JS02 (black curve). The resulting statistical agreement is, however, only 10 %, and so we discuss the origin of the disagreement between the simulation results and the observation data in what follows.

In SIM-SA, the main difference between PDFs for our simulation data and observation data analyzed by Kawahara (2010) comes from the much smaller number of observation data with $q < 0.65$ than the simulation results. One may suspect that multiple-halos (halos comprising two or more big structures; see Figure 5.1) occupy most parts of the PDF at $q < 0.65$ in our simulation. To check if this is true, we classify our clusters into single-halos and multiple-halos in the same way as Subsection 5.2.2; based on the mass of main dark matter halo M_1 and the mass of the most massive substructure M_2, a cluster is called a "single-halo" if $M_2/M_1 < 0.2$, and a "multiple-halo" otherwise. As a result, we find 4 multiple-halos among the 40 halos. Note that the fraction of the multiple-halos (10 %) is consistent with the halos analyzed in Chapter 5 (cf. Table 5.1).

In Figure 6.11, we color the PDF of q of S_X for SIM-SA in order to indicate the contributions from single-halos (red) and multiple-halos (green). The figure indicates that the results from multiple-halos have a broad distribution. This resembles the case of the projected dark matter density distribution (Section 5.5); q of multiple-halos distributes more broadly than three-dimensional space, and even more broadly at inner mass scales

(see Figure 5.10). Therefore the disagreement between the simulation results and the observation data is not mainly due to the multiple-halos.

One possibility for the origin of the disagreement between the simulation results and the observation data may be a selection effect in observations; for the same semi-major axis length, halos with smaller q are less massive, and therefore gas has lower temperature and density. Hence it is possible that smaller number of distorted clusters are observed than round clusters.

Also, the robustness of the analysis of the observation data should be tested. In this chapter, we fitted ellipses to *local* isocontours of S_X, just because Kawahara (2010) did so. Other method to determine q is possible; for example, one can use a kind of mass tensor with some weighting scheme. In this case, q is not locally determined, but the contribution from inner regions is taken into account. It is important to test the consistency between simulations and observations for more than one estimator.

In addition, how the baryonic processes included in simulations affect the non-sphericity of S_X should be more thoroughly tested. Especially, as seen in Section 6.4, the strength of AGN feedback influences shapes of dark matter halos, as well as S_X, even up to the virial radius.

All the above possibilities should be carefully examined by using much more simulation and observation data in the future, in order to test the validity of the CDM paradigm. In that sense, the comparison between the simulation results and the observation data in this chapter is still preliminary. We emphasize, however, that the above issues have become arguable because we have constructed the reliable PDF of q that is free from the assumptions of the self-similar density distribution and the hydrostatic equilibrium.

6.6 Short Summary

We have calculated the PDF of axis-ratio q of X-ray surface brightness S_X directly from the cosmological hydrodynamical simulations. We measure the axis ratio in the same way as Kawahara (2010), and compare our results with his result. The results in this chapter are summarized as follows:

1. The PDF of q of S_X calculated directly from the simulation data is totally different from the PDF for isopotential surfaces based on the self-similarity density distribution (Jing & Suto, 2002) and the hydrostatic equilibrium. The latter PDF, or such a simple model prediction should not be compared with observation data; the same estimator of axis ratio should be adopted both in simulations and observations.

2. We preliminarily compared our PDF of q of S_X with the X-ray observation data analyzed by Kawahara (2010). As a result, our PDF is much closer to the one derived from the observation data analyzed by Kawahara (2010), than the PDF for isopotential surfaces. However, since the statistical agreement is only 10 % according to the Kolmogorov-Smirnov test, and the disagreement may come from the selection effect in observations, robustness of the method to fit ellipses to S_X, etc.

3. The axis ratio of S_X depends little on radius and mass, consistent with that the

projected axis ratio of dark matter halos also depends little on radius and mass (Section 5.5).

The above results on S_X are mainly for the simulation with AGN feedback; the simulation reproduces typical density and temperature of observed clusters, much better than the simulation without AGN feedback. Another important result is obtained by comparing the different simulations:

4. The shapes of dark matter halos are significantly affected by the baryonic processes *up to the virial radius*, even though the spherically-averaged density profile is little affected outside a tenth of the virial radius. Specifically, if AGN feedback is absent, dark matter halos tend to be much rounder than those in the dark matter only simulation. If AGN feedback is adopted, halos are still slightly rounder than those in the dark matter only simulation.

At least at around the virial mass scale, the non-sphericity of dark matter halos in the simulation including AGN feedback is similar to that in the dark matter only simulation. Hence the results in Chapter 5 for the virial mass scale are little affected even if baryons are incorporated into simulations. In contrast, baryons have impact on the non-sphericity of halos at the inner mass scales (e.g. M_{2500} in Section 5.5). Therefore it is quite important to properly incorporate baryonic processes, especially AGN feedback, into simulations, to examine the non-sphericity of dark matter, not only gas.

Chapter 7

Summary and Conclusion

We have studied the non-sphericity of galaxy clusters by using the cosmological simulations. Especially, we paid a special attention to the simulation study of Jing & Suto (2002) (JS02). They approximated the isodensity surfaces of their simulated dark matter halos by triaxial ellipsoids, and found that their minor-to-major axis ratio follows a universal probability distribution function (PDF). The universality of the non-sphericity of halos suggests that comparisons of PDFs of axis ratio between simulations and observations can be tests for the cold dark matter (CDM) paradigm.

Observational estimates for PDFs of axis ratio has been performed, although the number of available data is small at this stage. In particular, Oguri et al. (2010) determined the axis ratio of weak lensing shear maps of clusters, and compared the resulting PDF of axis ratio with the PDF of projected axis ratio of dark matter halos, derived by Oguri et al. (2003) based on JS02. Also, Kawahara (2010) fitted ellipses to isocontours of X-ray surface brightness of 70 galaxy clusters. Then he compared the derived PDF of axis ratio of X-ray surface brightness with the PDF of axis ratio of isopotential surfaces predicted through the PDF of JS02 and the hydrostatic equilibrium assumption. Given the large observational uncertainty, both Oguri et al. (2010) and Kawahara (2010) concluded that the observation data and the predictions based on JS02 are barely consistent.

In this thesis, we showed that the predictions based on JS02 used in Oguri et al. (2010) and Kawahara (2010) are not adequate for more precise comparisons between simulations and observations. More reliable predictions on the non-sphericity of clusters are needed, since much more observation data will be available in the near future. Therefore, by using cosmological simulations, we presented predictions for the axis ratio of projected dark matter density distribution and the X-ray surface brightness, which will be useful in weak lensing analyses and X-ray observations, respectively. The specific results for the dark matter density distribution and the X-ray surface brightness are summarized in what follows.

In Chapter 5, we calculated PDFs of projected (two-dimensional) axis ratio of dark matter halos, directly from the projected density distribution in the simulation by using the mass tensor. We then showed that the resulting PDF is significantly different from the PDF of projected axis ratio, presented by Oguri et al. (2003) who projected the PDF of JS02. The difference between the two PDFs comes mainly from the assumption that the

three-dimensional density distribution is self-similar (described by concentric ellipsoids with common axis ratio), adopted in JS02. Since our calculation is free from the self-similarity assumption, our PDFs are more reliable when compared with weak lensing data.

We also found that our PDFs can be approximated by the beta distribution with two parameters that little depends on redshifts and radius (or mass scales from the center). The fitting formula will be useful for comparisons between simulations and observations.

As a preliminary approach, we compared the weak lensing data by Oguri et al. (2010) with the PDF of projected axis ratio directly calculated from the N-body simulation. Our PDF is broader than the PDF of Oguri et al. (2003), and seems to better agree with the observation data. However, after we convolve both PDFs with Gaussian with the dispersion corresponding to the typical uncertainty in the estimates of axis ratio, as done by Oguri et al. (2010), two PDFs cannot be discriminated due to the large observational error bars at this stage.

In order to make more precise comparisons, one should calculate the observable quantity, i.e., the lensed shear map, directly from simulations, and measure the axis ratio in the same way as the observation analysis. The analysis by Oguri et al. (2010) is, however, based on the assumption that halos have the self-similar density distribution in the three dimensional space. So the non-self-similarity of the projected density distribution cannot be examined in this method. Hence we did not reproduce the analysis by Oguri et al. (2010) in this thesis. With much more observation data in the near future, an analysis method that is free from the self-similarity assumption should be established.

In Chapter 6, we measured the axis ratio of X-ray surface brightness in the same way as Kawahara (2010). We then showed that the PDF of axis ratio of isopotential surfaces used in the analysis of Kawahara (2010) is inappropriate for comparisons with observation data; we calculate the PDF of axis ratio of X-ray surface brightness directly from the simulation data in the same way as Kawahara (2010), and showed that the resulting PDF is significantly different from the PDF of axis ratio of isopotential surfaces. The difference comes mainly from the assumption of the self-similar density distribution adopted by JS02, and from the hydrostatic equilibrium assumption.

Our PDF of axis ratio of X-ray surface brightness is free from the assumptions of self-similar density distribution and hydrostatic equilibrium, and therefore more reliable in comparisons with observation data.

We preliminarily compared our PDF of axis ratio of X-ray surface brightness with the X-ray data analyzed by Kawahara (2010). As a result, our PDF is much closer to the results of Kawahara (2010), than the PDF for isopotential surfaces based on JS02. The statistical agreement between our simulation results and the observation data is still 10 %. The origin of the disagreement may come from the selection effect in observations; for the same semi-major axis length, distorted clusters have smaller mass, and so the X-ray surface brightness is smaller. Also, the robustness of both the simulation results and the observation analysis should be more thoroughly examined in the future with much larger number of data, in order to test on the CDM paradigm.

In addition, we pointed out in Chapter 6 that shapes of dark matter halos are strongly

affected by the baryonic processes adopted in simulations even up to the virial radius, although the spherically averaged density profile is little affected. If AGN feedback is properly incorporated, the results in Chapter 5 at least at around the virial mass scale are little affected.

At the innermost mass scales (e.g., a fifth of the virial mass), halos become rounder due to baryonic processes. Therefore, even when the non-sphericity of dark matter density distribution alone is interested, hydrodynamical simulations are needed in order to precisely predict the PDF of axis ratio. These are challenging but important future tasks since a number of lensing data will be provided by the Subaru Hyper Suprime-Cam in the near future.

Generally, we emphasize that the same quantity should be adopted both in observations and simulations. This methodology is applicable to any other estimators of the non-sphericity of galaxy clusters. The main goal of this thesis was to establish this methodology, as well as to provide the more reliable PDFs of axis ratio than those based on the PDF of JS02.

Although the number of available observation data is limited for now, but our study in this thesis can be straightforwardly extended for much more observation data and higher resolution simulations in the future. Through more precise comparisons with simulations and observation data, the CDM paradigm will be severely tested, and cosmology beyond the standard model will develop further.

Acknowledgements

References

Adhikari, S., Dalal, N., & Chamberlain, R. T. 2014, JCAP, 11, 019, Splashback in accreting dark matter halos

Allen, S. W., Evrard, A. E., & Mantz, A. B. 2011, ARAA, 49, 409, Cosmological Parameters from Observations of Galaxy Clusters

Arnaud, M. & Evrard, A. E. 1999, MNRAS, 305, 631, The L_X-T relation and intracluster gas fractions of X-ray clusters

Bardeen, J. M., Bond, J. R., Kaiser, N., & Szalay, A. S. 1986, ApJ, 304, 15, The statistics of peaks of Gaussian random fields

Bertschinger, E. 1985, ApJS, 58, 39, Self-similar secondary infall and accretion in an Einstein-de Sitter universe

Binney, J. 1985, MNRAS, 212, 767, Testing for triaxiality with kinematic data

Bonamigo, M., Despali, G., Limousin, M., Angulo, R., Giocoli, C., & Soucail, G. 2015, MNRAS, 449, 3171, Universality of dark matter haloes shape over six decades in mass: insights from the Millennium XXL and SBARBINE simulations

Bond, J. R. & Myers, S. T. 1996, ApJS, 103, 1, The Peak-Patch Picture of Cosmic Catalogs. I. Algorithms

Colombi, S., Sousbie, T., Peirani, S., Plum, G., & Suto, Y. 2015, MNRAS, 450, 3724, Vlasov versus N-body: the Hénon sphere

Courtin, J., Rasera, Y., Alimi, J.-M., Corasaniti, P.-S., Boucher, V., & Füzfa, A. 2011, MNRAS, 410, 1911, Imprints of dark energy on cosmic structure formation - II. Non-universality of the halo mass function

Crocce, M., Pueblas, S., & Scoccimarro, R. 2006, MNRAS, 373, 369, Transients from initial conditions in cosmological simulations

Davis, M., Efstathiou, G., Frenk, C. S., & White, S. D. M. 1985, ApJ, 292, 371, The evolution of large-scale structure in a universe dominated by cold dark matter

Despali, G., Giocoli, C., & Tormen, G. 2014, MNRAS, 443, 3208, Some like it triaxial: the universality of dark matter halo shapes and their evolution along the cosmic time

REFERENCES

Diemer, B. & Kravtsov, A. V. 2014, ApJ, 789, 1, Dependence of the Outer Density Profiles of Halos on Their Mass Accretion Rate

Doroshkevich, A. G. 1970, Astrofizika, 6, 581, The space structure of perturbations and the origin of rotation of galaxies in the theory of fluctuation.

Dubois, Y., Devriendt, J., Slyz, A., & Teyssier, R. 2012, MNRAS, 420, 2662, Self-regulated growth of supermassive black holes by a dual jet-heating active galactic nucleus feedback mechanism: methods, tests and implications for cosmological simulations

Dubois, Y., Pichon, C., Welker, C., Le Borgne, D., Devriendt, J., Laigle, C., Codis, S., Pogosyan, D., Arnouts, S., Benabed, K., Bertin, E., Blaizot, J., Bouchet, F., Cardoso, J.-F., Colombi, S., de Lapparent, V., Desjacques, V., Gavazzi, R., Kassin, S., Kimm, T., McCracken, H., Milliard, B., Peirani, S., Prunet, S., Rouberol, S., Silk, J., Slyz, A., Sousbie, T., Teyssier, R., Tresse, L., Treyer, M., Vibert, D., & Volonteri, M. 2014, MNRAS, 444, 1453, Dancing in the dark: galactic properties trace spin swings along the cosmic web

Dubois, Y. & Teyssier, R. 2008, A&A, 477, 79, On the onset of galactic winds in quiescent star forming galaxies

Eke, V. R., Cole, S., & Frenk, C. S. 1996, MNRAS, 282, Cluster evolution as a diagnostic for Omega

Fang, T., Humphrey, P., & Buote, D. 2009, ApJ, 691, 1648, Rotation and Turbulence of the Hot Intracluster Medium in Galaxy Clusters

Fillmore, J. A. & Goldreich, P. 1984, ApJ, 281, 1, Self-similar gravitational collapse in an expanding universe

Greggio, L. & Renzini, A. 1983, A&A, 118, 217, The binary model for type I supernovae - Theoretical rates

Gunn, J. E. 1977, ApJ, 218, 592, Massive galactic halos. I - Formation and evolution

Gunn, J. E. & Gott, III, J. R. 1972, ApJ, 176, 1, On the Infall of Matter Into Clusters of Galaxies and Some Effects on Their Evolution

Haardt, F. & Madau, P. 1996, ApJ, 461, 20, Radiative Transfer in a Clumpy Universe. II. The Ultraviolet Extragalactic Background

Hahn, O. & Abel, T. 2011, MNRAS, 415, 2101, Multi-scale initial conditions for cosmological simulations

Hinshaw, G., Larson, D., Komatsu, E., Spergel, D. N., Bennett, C. L., Dunkley, J., Nolta, M. R., Halpern, M., Hill, R. S., Odegard, N., Page, L., Smith, K. M., Weiland, J. L., Gold, B., Jarosik, N., Kogut, A., Limon, M., Meyer, S. S., Tucker, G. S., Wollack, E., & Wright, E. L. 2013, ApJS, 208, 19, Nine-year Wilkinson Microwave Anisotropy Probe (WMAP) Observations: Cosmological Parameter Results

Jedrzejewski, R. I. 1987, MNRAS, 226, 747, CCD surface photometry of elliptical galaxies. I - Observations, reduction and results

Jing, Y. P. & Suto, Y. 2002, ApJ, 574, 538, Triaxial Modeling of Halo Density Profiles with High-Resolution N-Body Simulations

Kawahara, H. 2010, ApJ, 719, 1926, The Axis Ratio Distribution of X-ray Clusters Observed by XMM-Newton

Kazantzidis, S., Kravtsov, A. V., Zentner, A. R., Allgood, B., Nagai, D., & Moore, B. 2004, ApJL, 611, L73, The Effect of Gas Cooling on the Shapes of Dark Matter Halos

Komatsu, E., Smith, K. M., Dunkley, J., Bennett, C. L., Gold, B., Hinshaw, G., Jarosik, N., Larson, D., Nolta, M. R., Page, L., Spergel, D. N., Halpern, M., Hill, R. S., Kogut, A., Limon, M., Meyer, S. S., Odegard, N., Tucker, G. S., Weiland, J. L., Wollack, E., & Wright, E. L. 2011, ApJS, 192, 18, Seven-year Wilkinson Microwave Anisotropy Probe (WMAP) Observations: Cosmological Interpretation

Lacey, C. & Cole, S. 1993, MNRAS, 262, 627, Merger rates in hierarchical models of galaxy formation

Lau, E. T., Kravtsov, A. V., & Nagai, D. 2009, ApJ, 705, 1129, Residual Gas Motions in the Intracluster Medium and Bias in Hydrostatic Measurements of Mass Profiles of Clusters

Lau, E. T., Nagai, D., & Nelson, K. 2013, ApJ, 777, 151, Weighing Galaxy Clusters with Gas. I. On the Methods of Computing Hydrostatic Mass Bias

Lee, J. & Suto, Y. 2003, ApJ, 585, 151, Modeling Intracluster Gas in Triaxial Dark Halos: An Analytic Approach

Leitherer, C., Ortiz Otálvaro, P. A., Bresolin, F., Kudritzki, R.-P., Lo Faro, B., Pauldrach, A. W. A., Pettini, M., & Rix, S. A. 2010, ApJS, 189, 309, A Library of Theoretical Ultraviolet Spectra of Massive, Hot Stars for Evolutionary Synthesis

Leitherer, C., Schaerer, D., Goldader, J. D., Delgado, R. M. G., Robert, C., Kune, D. F., de Mello, D. F., Devost, D., & Heckman, T. M. 1999, ApJS, 123, 3, Starburst99: Synthesis Models for Galaxies with Active Star Formation

Lewis, A., Challinor, A., & Lasenby, A. 2000, ApJ, 538, 473, Efficient Computation of Cosmic Microwave Background Anisotropies in Closed Friedmann-Robertson-Walker Models

Łokas, E. L. & Mamon, G. A. 2001, MNRAS, 321, 155, Properties of spherical galaxies and clusters with an NFW density profile

Ludlow, A. D., Borzyszkowski, M., & Porciani, C. 2014, MNRAS, 445, 4110, The formation of CDM haloes - I. Collapse thresholds and the ellipsoidal collapse model

More, S., Diemer, B., & Kravtsov, A. V. 2015, ApJ, 810, 36, The Splashback Radius as a Physical Halo Boundary and the Growth of Halo Mass

More, S., Kravtsov, A. V., Dalal, N., & Gottlöber, S. 2011, ApJS, 195, 4, The Overdensity and Masses of the Friends-of-friends Halos and Universality of Halo Mass Function

Nakamura, T. T. & Suto, Y. 1997, Progress of Theoretical Physics, 97, Strong Gravitational Lensing and Velocity Function as Tools to Probe Cosmological Parameters — Current Constraints and Future Predictions —

Navarro, J. F., Frenk, C. S., & White, S. D. M. 1995, MNRAS, 275, 720, Simulations of X-ray clusters

—. 1996, ApJ, 462, 563, The Structure of Cold Dark Matter Halos

—. 1997, ApJ, 490, 493, A Universal Density Profile from Hierarchical Clustering

Nishimichi, T. & Oka, A. 2014, MNRAS, 444, 1400, Simulating the anisotropic clustering of luminous red galaxies with subhaloes: a direct confrontation with observation and cosmological implications

Nishimichi, T., Shirata, A., Taruya, A., Yahata, K., Saito, S., Suto, Y., Takahashi, R., Yoshida, N., Matsubara, T., Sugiyama, N., Kayo, I., Jing, Y., & Yoshikawa, K. 2009, PASJ, 61, 321, Modeling Nonlinear Evolution of Baryon Acoustic Oscillations: Convergence Regime of N-body Simulations and Analytic Models

Nowakowski, M., Sanabria, J.-C., & Garcia, A. 2002, Phys. Rev. Let., 66, 023003, Gravitational equilibrium in the presence of a positive cosmological constant

Oguri, M., Bayliss, M. B., Dahle, H., Sharon, K., Gladders, M. D., Natarajan, P., Hennawi, J. F., & Koester, B. P. 2012, MNRAS, 420, 3213, Combined strong and weak lensing analysis of 28 clusters from the Sloan Giant Arcs Survey

Oguri, M., Lee, J., & Suto, Y. 2003, ApJ, 599, 7, Arc Statistics in Triaxial Dark Matter Halos: Testing the Collisionless Cold Dark Matter Paradigm

Oguri, M., Takada, M., Okabe, N., & Smith, G. P. 2010, MNRAS, 405, 2215, Direct measurement of dark matter halo ellipticity from two-dimensional lensing shear maps of 25 massive clusters

Omma, H., Binney, J., Bryan, G., & Slyz, A. 2004, MNRAS, 348, 1105, Heating cooling flows with jets

Peebles, P. J. E. 1980, The large-scale structure of the universe

Press, W. H. & Schechter, P. 1974, ApJ, 187, 425, Formation of Galaxies and Clusters of Galaxies by Self-Similar Gravitational Condensation

Prunet, S., Pichon, C., Aubert, D., Pogosyan, D., Teyssier, R., & Gottloeber, S. 2008, ApJS, 178, 179, Initial Conditions For Large Cosmological Simulations

Rasera, Y. & Teyssier, R. 2006, A&A, 445, 1, The history of the baryon budget. Cosmic logistics in a hierarchical universe

Rines, K., Geller, M. J., Diaferio, A., & Kurtz, M. J. 2013, ApJ, 767, 15, Measuring the Ultimate Halo Mass of Galaxy Clusters: Redshifts and Mass Profiles from the Hectospec Cluster Survey (HeCS)

Rossi, G., Sheth, R. K., & Tormen, G. 2011, MNRAS, 416, 248, Modelling the shapes of the largest gravitationally bound objects

Scoccimarro, R. 1998, MNRAS, 299, 1097, Transients from initial conditions: a perturbative analysis

Snowden, S. L., Mushotzky, R. F., Kuntz, K. D., & Davis, D. S. 2008, A&A, 478, 615, A catalog of galaxy clusters observed by XMM-Newton

Sousbie, T. & Colombi, S. 2015, ArXiv e-prints, ColDICE: a parallel Vlasov-Poisson solver using moving adaptive simplicial tessellation

Springel, V. 2005, MNRAS, 364, 1105, The cosmological simulation code GADGET-2

Springel, V., White, S. D. M., Tormen, G., & Kauffmann, G. 2001, MNRAS, 328, 726, Populating a cluster of galaxies - I. Results at z=0

Sutherland, R. S. & Dopita, M. A. 1993, ApJS, 88, 253, Cooling functions for low-density astrophysical plasmas

Suto, D., Kawahara, H., Kitayama, T., Sasaki, S., Suto, Y., & Cen, R. 2013, ApJ, 767, 79, Validity of Hydrostatic Equilibrium in Galaxy Clusters from Cosmological Hydrodynamical Simulations

Suto, D., Kitayama, T., Osato, K., Sasaki, S., & Suto, Y. 2016, PASJ, 68, 14, Confrontation of top-hat spherical collapse against dark halos from cosmological N-body simulations

Teyssier, R. 2002, A&A, 385, 337, Cosmological hydrodynamics with adaptive mesh refinement. A new high resolution code called RAMSES

Valageas, P. & Nishimichi, T. 2011, A&A, 527, A87, Combining perturbation theories with halo models

Vega, J., Yepes, G., & Gottlöber, S. 2016, ArXiv e-prints, On the shape of dark matter halos from MultiDark Planck simulations

White, S. D. M. & Silk, J. 1979, ApJ, 231, 1, The growth of aspherical structure in the universe - Is the local supercluster an unusual system